

Modeling of pCO₂ Point-of-Care Devices

by Xu Liang Li

A thesis submitted to the Department of Chemical Engineering in
conformity with the requirements for the degree of Master's of Applied
Science

Queen's University
Kingston, Ontario, Canada

January, 2014

Copyright © Xu Liang Li, **2014**

Abstract

A dynamic model is developed and presented that predicts the voltage response for a Severinghaus electrode-based point-of-care pCO₂ sensor. Eight partial differential equations are derived to describe the diffusion and reaction phenomena in the sensor. The model is able to predict the potential response versus time behaviour from different CO₂ concentrations in the calibration fluid and control fluids.

The two most influential and uncertain parameters in the model are determined to be the forward rate constant for benzoquinone consumption at the gold surface ($k_{f_{Au}}$), and the partition coefficient for CO₂ between the membrane and the electrolyte ($\kappa_{CO_{2m}}$). These parameters were adjusted heuristically to obtain a good fit (within 2 mV) between the dynamic voltage response data and the model predictions during a critical 4 second period. The model predictions are sufficient for design sensitivity studies, however an improved fit might be possible using a formal least-squares parameter estimation approach, or if additional parameters were estimated.

Several design parameters are varied to study the influence of the electrolyte concentration and the sensor geometry on the voltage response. The most influential design parameter studied is the amount of water present in the electrolyte during sensor operation. This can be affected by the amount of water evaporated during manufacturing and storage, and by the amount of water present when the sensor “wets up” again during operation. The amount of water picked up by the sensor in turn is affected by design parameters such as component/membrane dimensions and thicknesses. The initial buffer

concentration in the electrolyte is the second most influential parameter. The resulting model can be used to perform “what if” analyses in order to understand the impact of design decisions on the sensor performance, and to potentially improve the sensor from performance and manufacturing cost perspectives.

Acknowledgement

First of all and foremost, I owe a big thank-you to my supervisors, Professor Kim McAuley and Professor Jim McLellan, for their guidance and delightful discussions during my Master's degree. Kim and Jim, your kindness, patience, and expertise will be missed by me deeply. I will miss our time spent together in Dupuis Hall, Gordon Hall, and via Skype. I learnt so much about modeling and writing a thesis for the past two years.

I would also like to thank my industrial supervisor, Dr. Craig Jeffrey, for his help with gathering all the data and discussions on how the sensor works. Thanks to Dr. Glenn Martin who was very patient to explain the electrochemistry at the electrodes. Special thanks to Stephen Snyder and Niko Lee-Yow for helping me with COMSOLTM implementation.

I am indebted to the thesis examine committee, Dr. Brian Amsden, Dr. Dominik Barz and Dr. Jon Pharoah. They took the time to go through my thesis and gave me many valuable suggestions.

Financial support from Queen's University, MITACS, Ontario Centre of Excellence and our industrial sponsor Abbott Point of Care made this project possible and there was no way to do this project without them.

My office mates, Jessica, Hui, Ryan, Abdullah, Hadis, Emily, Zahra and Yasmine made my time in Dupuis Hall G36 enjoyable and fun. Thanks for all the fun we had together especially with food and I will miss you all very much.

Finally, I would like to thank my parents for encouraging me throughout my Master's journey whenever I am excited or frustrated with my simulation results.

Table of Contents

Abstract.....	ii
Acknowledgement	iv
List of Tables	vi
List of Figures	vii
List of Abbreviations	x
List of Nomenclature	xi
Chapter 1 Introduction	1
Chapter 2 Model Development.....	15
2.1 Summary of Equation Development, Boundary Conditions, and Initial Model Parameters.....	19
2.2 Development of Material Balances and Boundary Conditions.....	27
2.3 Model Implementation in COMSOL™.....	43
2.4 Summary	58
Chapter 3 Simulation Results.....	58
3.1 Overview.....	58
3.2 Simulated Voltage Response Plots for Calibrant.....	63
3.3 Identifying the Two Most Influential Parameters.....	67
3.4 Sensitivity Analysis	73
3.5 Summary	86
Chapter 4 Conclusions and Recommendations.....	88
4.1 Conclusions.....	88
4.2 Contributions of this Thesis	90
4.3 Recommendations for Future Work.....	91
References:.....	92
Appendix:.....	96

List of Tables

Table 1: Model Assumptions	15
Table 2: Initial Parameters Used in Model Development.....	20
Table 3: Table of PDEs.....	22
Table 4: Boundary and Initial Conditions.....	23
Table 5: Heat of Reactions.....	31
Table 6: Values of α from 273.15 K to 348.15 K.	41
Table 7: Lumped Diffusion Coefficients Used in Model	43
Table 8: Parameter List in COMSOL TM	45
Table 9: Variable List	47
Table 10: pCO ₂ Values of Calibrant and Control Fluids.	60
Table 11: Scaled Sensitivity Matrix for Parameter Ranking	69

List of Figures

Figure 1: Traditional Severinghaus Carbon Dioxide Sensor. The electrolyte contains NaHCO_3 and water.	3
Figure 2: Potential change vs. time for a traditional Severinghaus sensor	4
Figure 3: Improved pCO_2 Sensor. The electrolyte contains NaHCO_3 , BQ, carbonic anhydrase, sucrose, KCl.....	7
Figure 4: Sensor operation timeline.....	9
Figure 5: Change in potential difference vs. time during sensor operation.	10
Figure 6: Concentration profile in Ross Equation.	12
Figure 7: Side View of Sensor with Flow Channel.	19
Figure 8: Electrodes with electrical connection strips.	19
Figure 9: Differential element of height Δz and thickness Δr	27
Figure 10: Schematic of pCO_2 Sensor	36
Figure 11: Small ring with thickness Δr	37
Figure 12: Curves of best fit for α and B.	42
Figure 13: Tree structure of the Transport of Diluted Species Modules	45
Figure 14: Voltage response at the Au electrode	47
Figure 15: Sub tabs in Transport of Diluted Species modules.....	50
Figure 16: Diffusion coefficients under “Diffusion GPM” and “Diffusion Electrolyte” .	51
Figure 17: Initial conditions in membrane and electrolyte	53
Figure 18: Reaction tab in electrolyte.....	54
Figure 19: Continuous flux at the interphase between gas-permeable membrane and electrolyte.....	55
Figure 20: BCs involving the Henry’s constant.....	56
Figure 21: BCs involving the partition coefficient between the membrane and the electrolyte.....	57

Figure 22: Reaction flux at the Au electrode.....	58
Figure 23: Voltage responses as a function of time for calibrant (from t_2 to t_3) and control fluids (from t_4 to t_5) for a) CV1, b) L2, c) GB, and d) CV5. Green error bars for measurements are show at two points to illustrate reproducibility.....	63
Figure 24: Voltage response for a simulation for calibrant in COMSOL TM with $k_{fAu} = 666.28 \text{ m7s} \cdot \text{mol2}$	64
Figure 25: Voltage response for a simulation with $k_{fAu} = 160 \text{ m7s} \cdot \text{mol2}$	65
Figure 26: Voltage response for a simulation with $k_{fAu} = 700 \text{ m7s} \cdot \text{mol2}$	66
Figure 27: Voltage response for all control fluids. The red marks are data points from experiments. The solid red marks are the initial predetermined number of seconds that are used to calculate the mean voltage response.....	66
Figure 28: Mean voltage response vs $p\text{CO}_2$ plots for the base and tuned cases	71
Figure 29: Voltage response for all control fluids for using initial parameter values in Table 8 are represented by dashed lines and voltage response using tuned parameter values are represented by solid lines.....	72
Figure 30: Concentration profiles for carbonic acid at the middle of the Au surface.	72
Figure 31: Voltage response for calibrant used for concentration profiles at centre of the Au electrode	73
Figure 32: Centre of Au electrode where carbonic acid concentration profiles are taken	73
Figure 33: Influence of water concentration in electrolyte voltage response for the calibrant.....	75
Figure 34: Influence of water concentration in electrolyte on voltage responses for control fluids.	76
Figure 35: Influence of the electrolyte height on voltage response for the calibrant.	77
Figure 36: Influence of water concentration in electrolyte on voltage responses for control fluids	77
Figure 37: Influence of water concentration in electrolyte and electrolyte thickness on voltage response for the calibrant.	78

Figure 38: Influence of water concentration in electrolyte on voltage responses for control fluids	79
Figure 39: Influence of initial carbonic acid concentration in electrolyte on voltage response for the calibrant.	80
Figure 40: Influence of initial carbonic acid concentration in electrolyte on voltage responses for control fluids.....	81
Figure 41: Influence of initial buffer concentration in electrolyte on voltage response for the calibrant.....	82
Figure 42: Influence of initial buffer concentration in electrolyte on voltage responses for control fluids	83
Figure 43: Influence of initial BQ concentration in electrolyte on voltage response for the calibrant.....	84
Figure 44: Influence of BQ concentration in electrolyte on voltage response for control fluids	84
Figure 45: Influence of Au electrode surface area voltage response for the calibrant	85
Figure 46: Influence of Au electrode surface on voltage responses for control fluids.....	85

List of Abbreviations

POC	Point-of-care
PDE	Partial differential equation
BC	Boundary conditions

List of Nomenclature

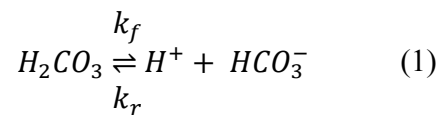
Symbol	Description
k_f	forward rate constant
k_r	reverse rate constant
E	electrode potential of gold
E_o	standard electrode potential of gold
R	ideal gas constant
T	absolute temperature
n	stoichiometric number of electrons transferred
F	Faraday constant
t	Time
L	thickness of electrolyte layer in Ross model
$C_e(0)$	the initial centration of H_2CO_3 in the electrolyte
$C_e(\infty)$	final concentration that would be reached when the concentration of H_2CO_3 in the electrolyte becomes equal to the concentration of H_2CO_3 in the blood sample
D	diffusion coefficient
ϵ	driving force in the Ross model
Z	vertical axis
R	radial direction
R_1	Width of electrolyte
R_2	Width of membrane
Z_1	Height of electrolyte
Z_2	Height of membrane
R_{AuI}	Inner radius of Au electrode
R_{AuO}	Outer radius of Au electrode
a	mean radius of Cl^-
D_{CO_2m}	Diffusion coefficient of CO_2 in membrane
$D_{H_2CO_3}$	Diffusion coefficient of H_2CO_3
$D_{HCO_3^-}$	Diffusion coefficient of HCO_3^-
D_{H^+}	Diffusion coefficient of H^+
D_{OH^-}	Diffusion coefficient of OH^-
$D_{CO_3^{2-}}$	Diffusion coefficient of CO_3^{2-}
D_{BQ}	Diffusion coefficient of BQ
D_{H_2Q}	Diffusion coefficient of H_2Q
$K_{HCO_3^-}$	Equilibrium constant of HCO_3^-
$K_{H_2CO_3}$	Equilibrium constant of H_2CO_3
K_{H_2O}	Equilibrium constant of H_2O
$K_{AuSurface}$	Equilibrium constant of the electrochemical reaction at Au electrode surface
$[H_2CO_3]_0$	Initial concentration of H_2CO_3
$[K^+]_0$	Initial concentration of K^+
$[Cl^-]_0$	Initial concentration of Cl^-

$[CO_3^{2-}]_0$	Initial concentration of CO_3^{2-}
$[Na^+]_0$	Initial concentration of Na^+
$[HCO_3^-]_0$	Initial concentration of HCO_3^-
$[H^+]_0$	Initial concentration of H^+
$[OH^-]_0$	Initial concentration of OH^-
$[H_2O]_0$	Initial concentration of H_2O
$[BQ]_0$	Initial concentration of BQ
$[H_2Q]_0$	Initial concentration of H_2Q
H	Henry's constant
κ_{CO_2m}	Partition coefficient
$k_{f_{Au}}$	Forward reaction rate constant at the Au electrode
$k_{f_{H_2CO_3}}$	Forward reaction rate constant for the dissociation of carbonic acid
$k_{f_{HCO_3^-}}$	Forward reaction rate constant for the dissociation of bi carbonate
$k_{f_{H_2O}}$	Forward reaction rate constant for the dissociation of water
$k_{r_{Au}}$	Reverse reaction rate constant at the Au electrode
$k_{r_{HCO_3^-}}$	Reverse reaction rate constant for the dissociation of bicarbonate
$k_{r_{H_2CO_3}}$	Reverse reaction rate constant for the dissociation of carbonic acid
$k_{r_{H_2O}}$	Reverse reaction rate constant for the dissociation of water

Chapter 1 Introduction

The global market for Blood Gas and Electrolyte Analyzers has been forecasted at 27,432 units and US\$477 million by the year 2017 (Global Industry Analysts, Inc., 2012). The reasons for this substantial demand are that the aging population will lead to more patients demanding critical care, and the growing popularity of point-of-care (POC) blood gas testing due to its simplicity, rapid read-out, and portability. One important test that is routinely performed using POC technology is pCO₂, which determines the partial pressure of dissolved carbon dioxide in the blood. pCO₂ is an indicator of the acid/base chemistry of the human body and is therefore one important blood test for assessing the condition of patients (Lane and Walker, 1987).

The Abbott Point of Care pCO₂ POC sensor is a potentiometric sensor based on a Severinghaus design (Severinghaus and Bradley, 1958; Lauks and Maczuszenko, 2006; Davis et al., 1996). In this sensor, CO₂ diffuses from the blood sample through a membrane and into the aqueous electrolyte. The sensor detects the resulting pH change associated with the dissolution of CO₂ and the formation of carbonic acid. Changes in pCO₂ result in changes in [H⁺] at the cathode surface. In traditional Severinghaus sensors there is a pH-sensitive glass electrode that detects the pH change in the electrolyte. The change in pH is governed by the chemical equilibrium (Severinghaus and Bradley, 1958):



The traditional Severinghaus sensor (generally not employed in POC applications) is composed of a pH electrode, a reference electrode (usually a Ag/AgCl electrode), and a NaHCO_3 electrolyte buffer solution, which is separated from the sample by a gas-permeable membrane. NaHCO_3 in the electrolyte is completely dissociated into Na^+ and HCO_3^- . These additional HCO_3^- ions affect the pH by shifting equilibrium reaction (1) to the left. High concentrations of bicarbonate (e.g., 2 mmol/L) influence the sensitivity of the sensor to CO_2 and lengthen the sensor's response time (Zosel et al., 2011) which is undesirable. Figure 1 shows a traditional Severinghaus carbon dioxide sensor (Ross et al., 1973).

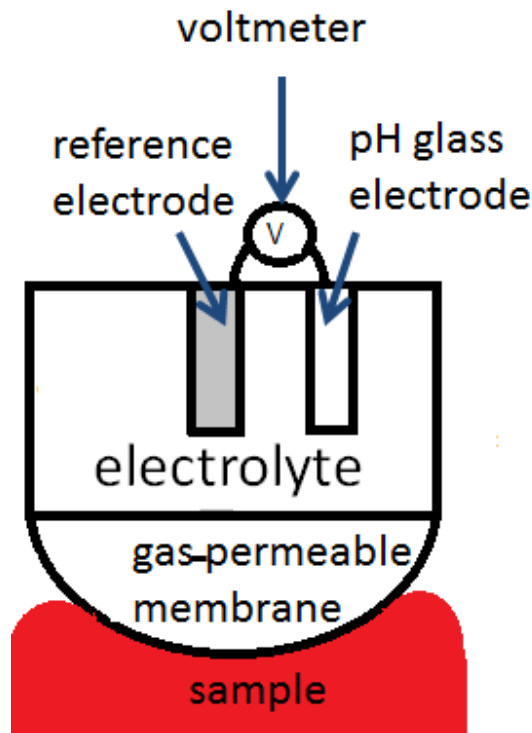


Figure 1: Traditional Severinghaus Carbon Dioxide Sensor (after Ross et al., 1973; Davis et al., 1996). The electrolyte contains NaHCO_3 and water.

The blood sample at the bottom is in contact with the gas-permeable membrane, which permits some of the CO_2 to diffuse into the electrolyte, until equilibrium is reached.

The potential of the pH glass electrode changes relative to the reference electrode as the acidity changes due to the dissolved CO_2 .

One shortcoming of the traditional Severinghaus sensor is that equilibrium needs to be established between the CO_2 level in the sample and the electrolyte so that accurate readings can be obtained. Many articles concerned with the design of Severinghaus electrodes focus on shortening the response time for this equilibrium to be established

(Zhao and Cai, 1997; Tongol et al., 2003; Meyerhoff et al., 1983; Lopez, 1984). Also, the traditional Severinghaus sensor has difficulties when measuring low CO_2 levels, due to poor sensitivity and to CO_2 depletion from the sample as CO_2 diffuses into the electrolyte. Therefore, achieving wide detection limits has been an important issue in Severinghaus sensor design (Cai and Reimers, 1993). Severinghaus sensors have been modified by many scientists to achieve improved response time and accuracy (Zhao and Cai, 1997; Tongol et al., 2003; Meyerhoff et al., 1983; Lopez, 1984).

Figure 2 shows the dynamic response of a traditional Severinghaus sensor when it is used for measuring CO_2 concentrations in ocean water (Cai and Reimers, 1993). Steady-state data obtained after 40 minutes would be used to calculate pCO_2 .

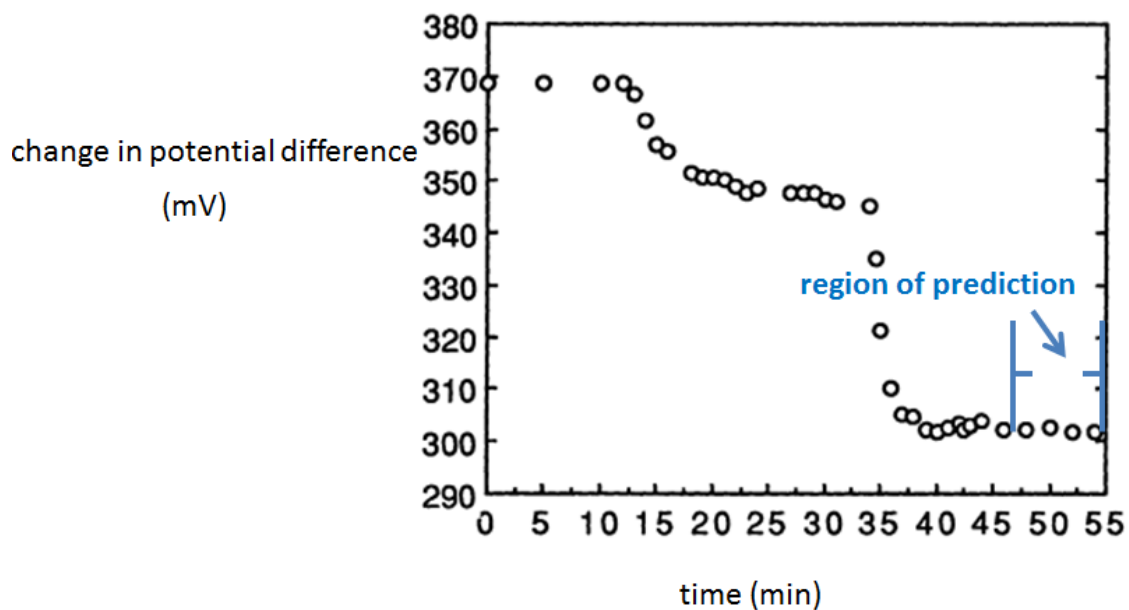
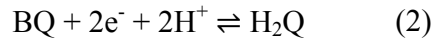
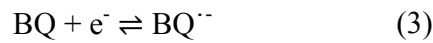


Figure 2: Potential change vs. time for a traditional Severinghaus sensor (from Cai and Reimers, 1993).

In the improved Severinghaus sensor for POC usage that is modeled in this study, the pH glass electrode is replaced by a gold electrode (Davis et al., 1996; Lauks and Maczuszenko, 2006). As in the traditional design, when the sample is in contact with the sensor, CO₂ diffuses through a gas-permeable membrane and into the electrolyte, which is in contact with a Ag/AgCl reference electrode and the gold electrode. The dissolved CO₂ reacts with water to form carbonic acid, which dissociates to form hydrogen ions as shown in reaction (1). The improved sensor contains sodium bicarbonate and carbonic anhydrase enzyme, which catalyzes the hydration of CO₂ to speed up the sensor response time and reduce sensor drift (Zhao and Cai, 1997; Zosel et al., 2011). The electrolyte also contains benzoquinone (BQ) (Lauks, 1998; Lauks and Maczuszenko, 2006; Davis et al., 1996). The potential of the Au electrode changes when BQ reacts with hydrogen ions and electrons at the Au electrode surface (Hui et al., 2009):



Changes in the potential difference over time are measured between the Au electrode and the reference Ag/AgCl electrode. Reaction (2) is actually a series of elementary reactions (Guin et al., 2011):



If reaction equilibrium is assumed to exist at the Au/electrolyte surface, the Nernst equation can be used to determine the change in potential based on concentrations of the reactants (Hui et al., 2009):

$$E_{BQ \text{ to } H_2Q} = E_{BQ \text{ to } H_2Q}^o - \frac{RT}{nF} \ln \left(\frac{[H_2Q]}{[BQ][H^+]^2} \right) \quad (7)$$

where:

$E_{BQ \text{ to } H_2Q}$: electrode potential of the quinone reaction (V)

$E_{BQ \text{ to } H_2Q}^o$: standard electrode potential of the quinone reaction which is 0.699 V (Dabos, 1975)

R : ideal gas constant ($8.314 \frac{J}{mol \cdot K}$)

T : absolute temperature (K)

n : stoichiometric number of electrons transferred, which is 2 in this case

F : Faraday constant ($96,485.3365 \frac{C}{mol}$)

If the Nernst equation is used (i.e., equilibrium is assumed for reaction (2)), then knowledge of the individual rates for reactions (3) to (6) is not required.

The improved sensor that is modeled in this study is a very small lab-on-a-chip device with the width of the Au electrode being approximately 10 microns (Davis et al., 1996).

Figure 3 is a schematic diagram of the POC pCO₂ sensor.

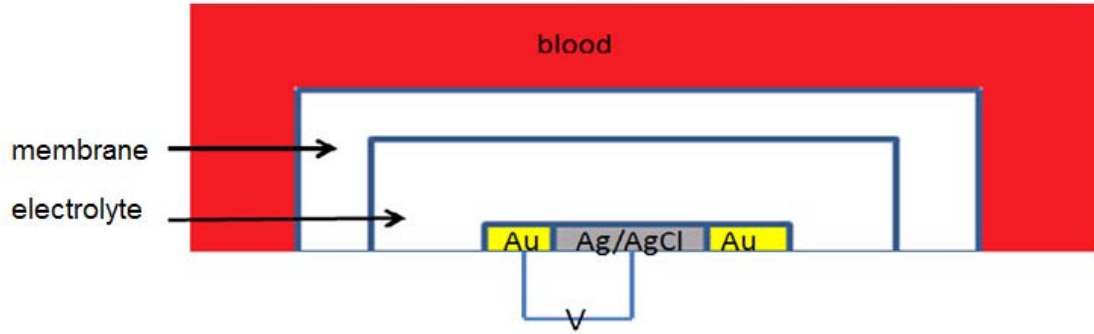


Figure 3: Improved pCO₂ Sensor. The electrolyte contains NaHCO₃, BQ, carbonic anhydrase, sucrose, KCl (after Davis et al., 1996; Lauks and Maczuszenko, 2006).

In addition to the sodium bicarbonate, BQ and carbonic anhydrase, the electrolyte also includes sucrose and KCl. The function of the sucrose is to keep the water within the electrolyte solution (i.e., via osmotic pressure), rather than having it diffuse out through the water- and CO₂- permeable membrane over time. The KCl affects the activity of the Cl⁻ in the electrolyte which in turn changes the potential of the reference Ag/AgCl electrode due to the ionic strength of the electrolyte. The activity of Cl⁻ is discussed in depth in Chapter Two.

The measured voltage from experimental data is governed by Equation (8):

$$E = E_{BQ \text{ to } H_2Q} - E_{ref} \quad (8)$$

where E is the measured voltage (V), $E_{BQ \text{ to } H_2Q}$ is the electrode potential of the quinone reaction (V) as shown in Equation (7), and E_{ref} is the voltage at the reference Ag/AgCl electrode (V).

The KCl in the electrolyte influences the potential of Ag/AgCl electrode. The reference Ag/AgCl electrode potential is calculated via Equation (9):

$$E_{ref} = E_{Ag/AgCl}^o - \frac{RT}{nF} \ln(a_{Cl^-}) \quad (9)$$

where $E_{Ag/AgCl}^o$ is the electrode potential of the reference Ag/AgCl electrode (V), which is 0.22233 V at 25 °C when compared against the standard hydrogen electrode (SHE) (Greeley and Smith et. al., 1960). a_{Cl^-} is the activity or effective concentration of chloride ion, Cl^- , in $\frac{mol}{L}$, which is discussed in Chapter Two.

Substituting Equations (7) and (9) into Equation (8) gives:

$$E = 0.699 - \frac{RT}{nF} \ln\left(\frac{[H_2Q]}{[BQ][H^+]^2}\right) - \left[0.22233 - \frac{RT}{nF} \ln(a_{Cl^-})\right] \quad (10)$$

This equation will be used in the model developed in this thesis to relate concentrations of H_2Q , BQ and H^+ to the measured voltage.

The i-STAT POC test system produced by Abbott Point of Care consists of a portable handheld analyzer that is capable of running various test cartridges for species of clinical interest such as creatinine, Na^+ , pCO_2 , and etc. Each cartridge containing the pCO_2 sensor is constructed with an onboard calibrant pack containing the calibration fluid. The operator fills the sample inlet well on each cartridge with a sample to be tested, seals the cartridge and inserts the cartridge into the handheld i-STAT analyzer to commence testing of the sample. When the cartridge is inserted into the analyzer, the calibrant and sample fluids are heated to 37 °C (human body temperature) during the course of the test. The sensor in Figure 3 is calibrated with each run (i-STAT cartridges are single-use

devices) so that reliable and accurate readings can be obtained. Note that the time scale has been normalized. A calibration fluid (aqueous solution with a known CO₂ concentration) is first delivered to the upper surface of membrane (before the blood sample is delivered). After a brief period of heating, the calibrant fluid comes in contact with the membrane so that CO₂ from the calibration fluid can begin diffusing into the electrolyte. This initial contact time is denoted as 0 seconds in Figure 4.

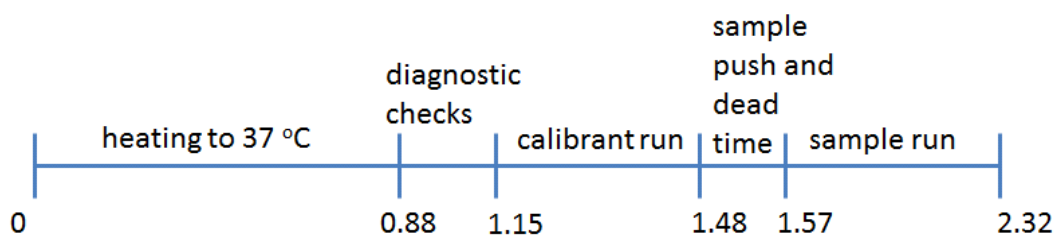


Figure 4: Sensor operation timeline (after Cozzette et al., 1992; Davis, 1998)

Heating to 37 °C is complete at 0.88, after which instrument and assay diagnostic checks are conducted for a brief period before data collection begins. At 1.15, readings of the potential difference between the Ag/AgCl electrode and the Au electrode are recorded until 1.48, when the calibration fluid is replaced by the blood sample, which induces a different dynamic response in the potential. Reliable readings of the potential are available at 1.57 from start of the “sample push”. The corresponding voltage response in Figure 5 and the known CO₂ concentration in the calibrant are then used to calculate the CO₂ partial pressure in the blood sample using an empirical model. Note that several values from the potential vs. time curves, rather than the final steady-state value (as used by the traditional Severinghaus sensor) are used to compute the CO₂ concentration in the blood sample.

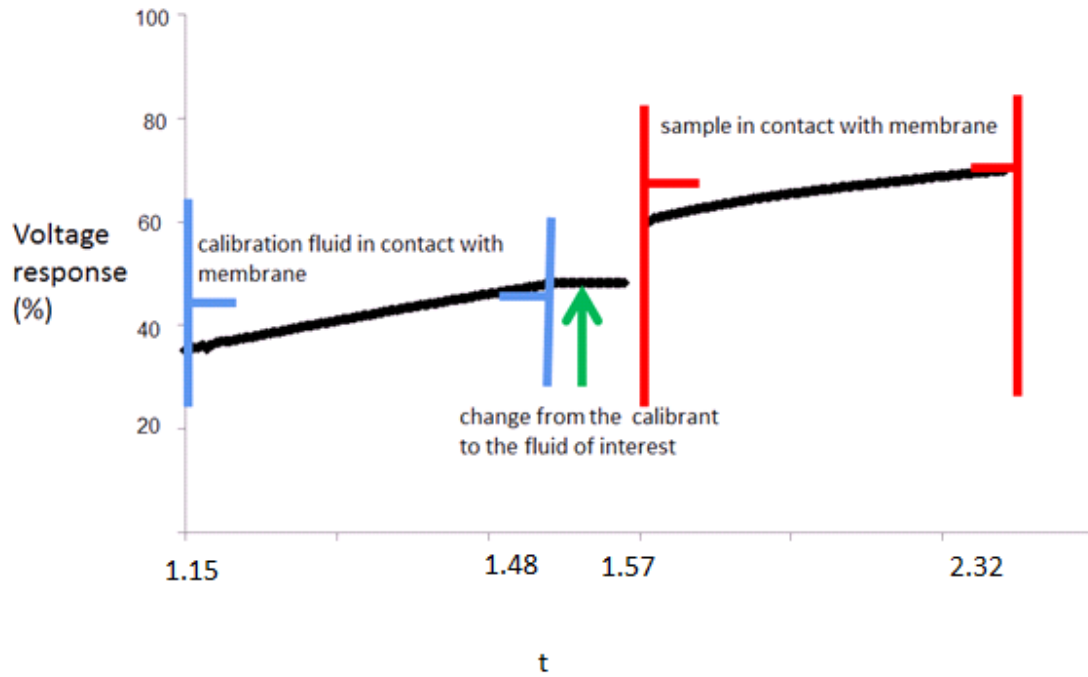


Figure 5: Change in potential difference vs. time during sensor operation (after Cozzette et al., 1992; Davis, 1998)

Until now, the only fundamental mathematical models that have been developed to describe potentiometric sensors for CO₂ are based on the work of Ross et al. (1973) who developed a simplified model to describe the operation of a traditional Severinghaus pCO₂ sensor (Jensen and Rechnitz, 1979; Cai and Reimers, 1993; Zosel et al., 2011). The Ross model was developed to determine the influence of various design parameters that affect the time t required to achieve a certain fractional approach to equilibrium for the aqueous CO₂ (i.e., the H₂CO₃) in the electrolyte. The Ross model:

$$t = \frac{Lm}{Dk} \frac{dC_I}{dC} \ln \left| \frac{C_e(\infty) - C_e(0)}{\epsilon C_e(\infty)} \right| \quad (11)$$

is useful for determining when the sensor response will be sufficiently close to steady state so that reliable measurements can be made using a traditional Severinghaus sensor (see Figure 2). The situation described by the Ross model is shown in Figure 6 where $C_e(0)$ is the initial concentration of H_2CO_3 in the electrolyte and $C_e(\infty)$ is the final concentration that would be reached when the concentration of H_2CO_3 in the electrolyte becomes equal to the concentration of H_2CO_3 in the blood sample. L is the thickness of the electrolyte layer, m is the thickness of the gas-permeable membrane, D is the diffusion coefficient of CO_2 in the gas-permeable membrane and k is a partition coefficient. The Ross model assumes that there is a linear concentration gradient across the gas-permeable membrane and Equation (12) is developed by assuming that the diffusion rate across the membrane is equal to the rate of accumulation of aqueous CO_2 (and related ionic species) within the electrolyte.

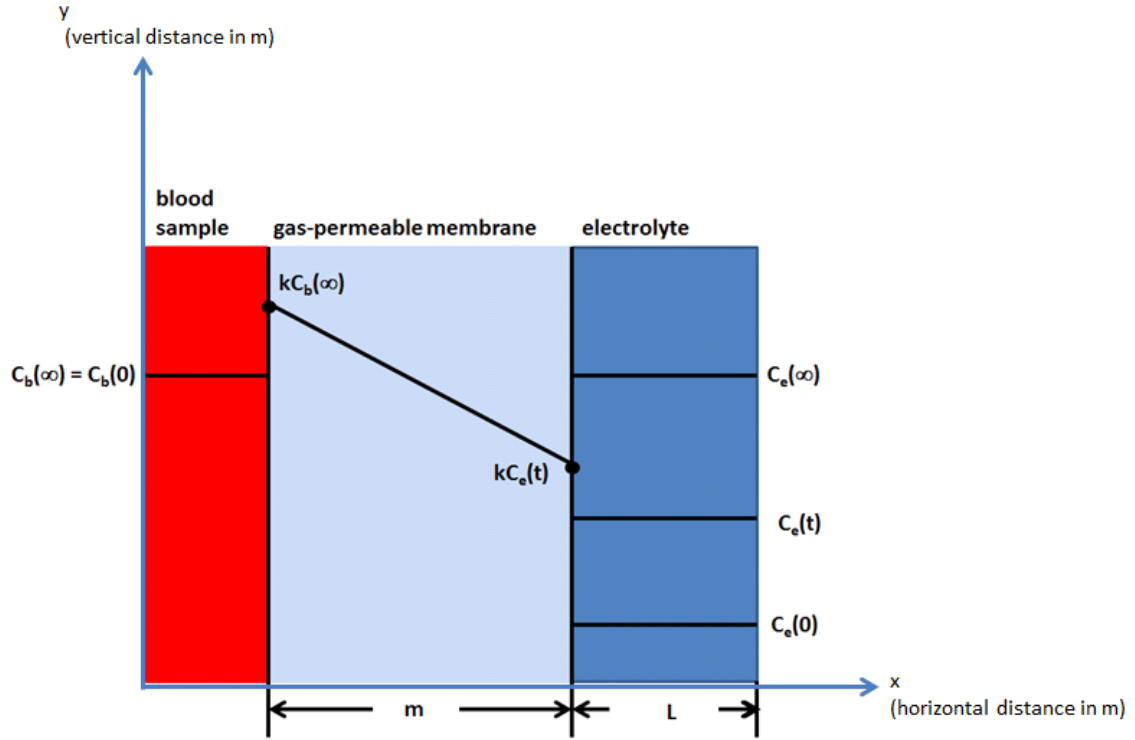


Figure 6: Concentration profile in Ross Equation (after Zoel et al., 2011).

In the Ross model ϵ is the dimensionless driving force:

$$\epsilon = \left| \frac{C_e(\infty) - C_e(t)}{C_e(\infty)} \right| \quad (12)$$

that approaches zero as H_2CO_3 accumulates in the electrolyte. $\frac{dC_I}{dC}$ (the change in the concentration of carbonic acid's associated ionic species over the change in the concentration of H_2CO_3) accounts for the accumulation of ionic species (HCO_3^- plus CO_3^{2-}) that are in equilibrium with H_2CO_3 . This ratio is required in the model because only a fraction of the CO_2 that diffuses through the membrane accumulates as H_2CO_3 . The value of $\frac{dC_I}{dC}$ can be assumed to be constant when the concentration of H_2CO_3 is high (i.e., higher than 2 mmol/L) (Zoel et al., 2011).

Assumptions in the Ross model include:

1. $C_b(\infty)=C_b(0)$ is constant because the blood volume is large compared to the electrolyte in Figure 6.
2. At the final steady state $C_b(\infty) = C_e(\infty)$ in Figure 6.
3. There is a linear CO_2 gradient within the gas-permeable membrane.
4. $C_e(t)$ is spatially uniform in the electrolyte because the only important resistance to mass transfer is in the gas-permeable membrane depicted in Figure 6.
5. All carbonate species in the electrolyte are in equilibrium.
6. The pH electrode responds instantaneously to pH changes in the electrolyte solution, which are caused by changes in $C_e(t)$ and the associated changes in the concentrations of ionic species.
7. The partition coefficient for CO_2 between the blood and the membrane is the same as the partition coefficient for CO_2 between the electrolyte and the membrane.

In the proposed model for the POC pCO_2 sensor, assumptions 1, 3 and 4 will be relaxed.

Assumption 6 does not apply because there is no pH electrode in the modified

Severinghaus system that will be modeled.

The Ross model only accounts for the diffusion of CO_2 through the gas-permeable membrane, neglecting concentration gradients of CO_2 and other species within the electrolyte. The model developed in this thesis will not only account for the CO_2 in the

gas-permeable membrane but will also account for the chemical reactions that occur in the electrolyte and at the electrode surface.

To my knowledge, the only model of a Severinghaus system that exhibits greater complexity than the Ross model is that developed by Samukawa et al. (1995). The system modeled consists of a pH electrode at the centre of a cylindrical container of electrolyte, which is surrounded by a cylindrical gas permeable membrane. Samukawa et al. used partial differential equations (PDEs) in cylindrical coordinates to account for changes in the partial pressure of dissolved CO_2 in time and two spatial dimensions. Zero-diffusion boundary conditions (BCs) were specified at the upper and lower surfaces of the electrolyte and at the surface between the electrolyte and the electrode. Presumably, the other BC in the radial direction is that the partial pressure of CO_2 at the outer edge of the membrane is equal to the partial pressure of CO_2 within the sample. Samukawa et al. used diffusion coefficients of $10^{-12} \text{ m}^2/\text{s}$ and $10^{-9} \text{ m}^2/\text{s}$, respectively, for CO_2 in the gas-permeable membrane and the electrolyte. The PDEs were discretized and solved using finite difference approximations and simulation results were shown for a variety of CO_2 pressures in the sample.

Like the model of Samukawa et al., the model proposed in this thesis will also use PDEs to model diffusion of CO_2 and H_2CO_3 in a Severinghaus sensor. The proposed model will be more detailed and will account for additional species (i.e., HCO_3^- , H^+ , OH^- , Na^+ , CO_3^{2-} , BQ and H_2Q) and for the different geometry used in the POC sensor.

The purpose of the current research project is to develop a mathematical model that will allow a POC pCO₂ sensor manufacturer to better estimate the effects of sensor design parameters on sensor performance. The proposed model will describe the potential versus time behaviour that results from the different CO₂ concentrations in the calibration fluid and standardized samples that are used for quality assurance. Many parameters in the model can be varied to influence the sensor performance including the dimensions of the membrane, electrolyte and electrodes and the concentrations of various species.

In this thesis, Chapter Two is concerned with model development and model implementation in COMSOLTM, including details such as setting up the BCs at the Au electrode surface. Chapter Three provides the simulation results and describes the methods used for parameter tuning. Conclusions and recommendations are provided in Chapter Four.

Chapter 2 Model Development

The mathematical model for the POC pCO₂ sensor consists of a set of material balances on the physical elements of the sensor. A simplified geometry is assumed for the membrane and electrode shown in Figures 7 and 8, so that the model equations can be written using cylindrical coordinates. Note that any effects of the electrode strips (see Figure 8 and Assumption 1.1 in Table 1) are ignored so that the behaviour of the sensor is uniform in the angular θ direction. The full set of assumptions used to develop the mathematical model is provided in Table 1.

Table 1: Model Assumptions

1.1	Concentrations of diffusing species in the membrane and electrolyte change in the vertical (z) direction and the radial (r) direction. There are no concentration gradients in the angular direction (θ), and the impact of gap in annular shape of the Au electrode and the electrode strips (see Figure 8) is negligible.
1.2	The CO ₂ partial pressure in the blood is uniform and at the bulk value. The concentration of CO ₂ within the blood remains constant over time because the amount of CO ₂ depletion is negligible.
1.3	The gas-permeable membrane is permeable to CO ₂ but not to other species in the blood or electrolyte. Any transfer of water through the membrane is neglected.
1.4	There is no bulk flow in this enclosed system.
1.5	The electrolyte has been heated to 37 °C at time zero so that changes in diffusivities and equilibrium constants over time due to temperature changes can neglected. Other factors that may influence diffusivities or equilibrium constants are also neglected, except for the influence of voltage on the equilibrium constant $K_{Au\ Surface}$ for the reaction at the surface of the Au electrode, which is included via Equation (31).
1.6	Concentrations within the electrolyte are spatially uniform at time zero. Any changes in water concentration within the electrolyte with time or position are negligible due to the high water concentration.
1.7	When the electrolyte solution is manufactured, it contains

	<p>significantly more water than the “dried down” electrolyte contained in the sensor. The amount of water that evaporates during sensor production and storage is not well known. In base case simulations, half of the water in the “as manufactured” electrolyte solution is assumed to be present in the electrolyte so that the concentrations of BQ and the NaHCO_3 buffer are twice of those in the “as manufactured” electrolyte. Other simulations are conducted using different amounts of water.</p>
1.8	<p>The initial H_2CO_3 concentration in the electrolyte during manufacturing is assumed to be $10^{-5} \text{ mol L}^{-1}$ in the base case simulations. This concentration would be in equilibrium with air at 25 °C containing a typical CO_2 concentration of 0.04 kPa (Manahan, 2005). The initial H_2CO_3 concentration is changed in other simulations.</p>
1.9	<p>Sucrose does not participate in any chemical reactions in the electrolyte. Its only influence is to help keep the water concentration within the electrolyte constant during sensor storage and use.</p>
1.10	<p>NaHCO_3 is assumed to dissociate completely. The Cl^- ions from the entirely dissociated KCl in the electrolyte influence the potential of the reference Ag/AgCl electrode, but the K^+ ions have no important influence on the operation of the sensor.</p>
1.11	<p>The potential of the Ag/AgCl electrode is constant during the sensor operation.</p>

1.12	The sensor is able to replace the calibration fluid with blood sample instantaneously at the membrane surface. There is no influence of the air bubble between the calibration fluid and the blood sample as it passes quickly over the membrane surface.
1.13	Diffusion occurs due to concentration gradients alone. Potential gradients within the electrolyte are small because they are not imposed, but arise from ion diffusion. As a result, migration of ions due to potential gradients is neglected. Cations and anions in the electrolyte diffuse in pairs or threesomes to maintain electroneutrality, which influences the values of the lumped diffusivity parameters chosen for use in the model (see Table 7).
1.14	The Ag/AgCl and Au electrodes protrude into the electrolyte by only a small distance (see Figure 7) so that the bottom boundary of the electrolyte can be treated as a flat surface in the model.
1.15	The degrees of polymerization of the benzoquinone and hydroquinone in the electrolyte have no influence on the operation of the sensor (Lindsey, 1974).
1.16	H^+ , BQ and H_2Q are the only species that influence the potential at the surface of the Au electrode.
1.17	There is a small surface current at the Au electrode, but there is negligible external current. The forward rate constant k_{fAu} is assumed to be constant and is not influenced by the small changes in voltage that are detected. However, the reverse rate constant k_{rAu} , which is

	calculated from Equations (29) does depend on the voltage because the equilibrium constant $K_{Au\ Surface}$ is voltage dependent.
--	--

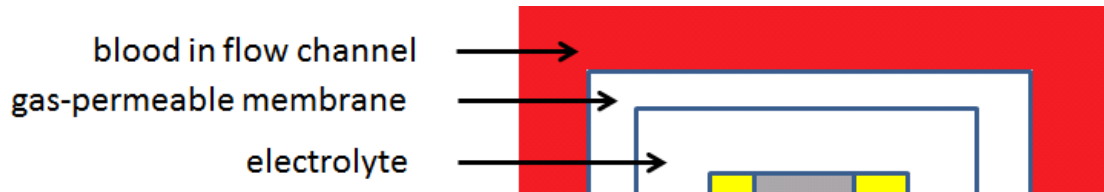


Figure 7: Side View of Sensor with Flow Channel (after Davis, 1998; Lauks, 1998).

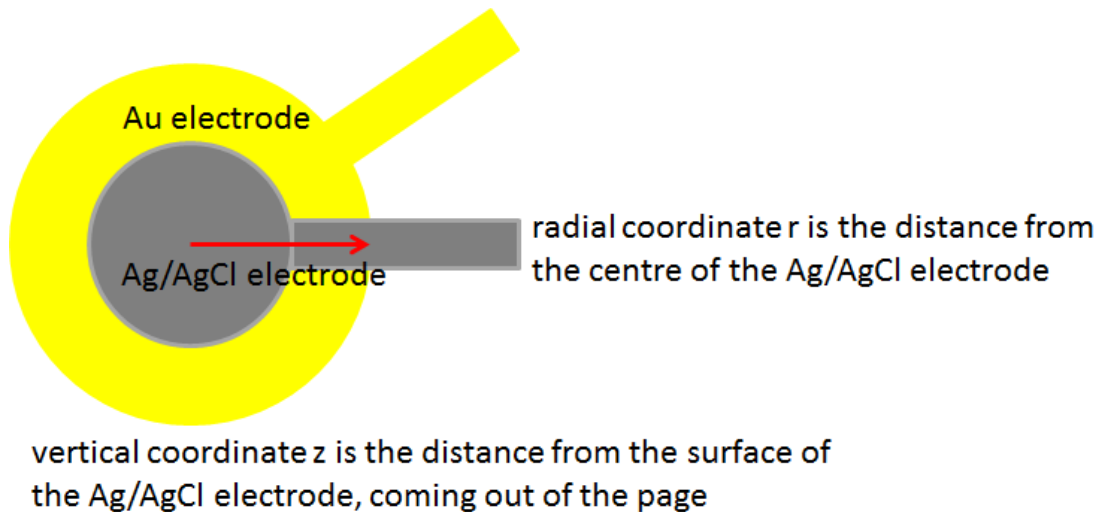


Figure 8: Electrodes with electrical connection strips (after Davis, 1998; Lauks, 1998).

2.1 Summary of Equation Development, Boundary Conditions, and Initial Model Parameters

Parameters used in the model, along with their initial literature values, are in shown in Table 2. Note that any parameter regarding the concentration of a particular species has a unit of mol/L due to the fact that Abbott Point of Care uses this unit for their stock solutions. However, this unit is converted to mol/m³ for the derivation of PDEs and

model implementation in COMSOLTM. Material balance partial differential equations (PDEs) developed for CO_2 in the membrane and H_2CO_3 , HCO_3^- , H^+ , OH^- , CO_3^{2-} , BQ, and H_2Q in the electrolyte are provided in Table 3. Initial and boundary conditions for the PDEs are provided in Table 4, where the conditions are grouped according to the corresponding PDEs (e.g., conditions (4.1.1) to (4.1.7) correspond to PDE (3.1)). Representative derivations for selected PDEs and BCs are provided in Section 2.2 along with a discussion of some of the parameter values. The derivations presented illustrate the approach taken (and the issues encountered) in developing the PDE model and BCs.

Table 2: Initial Parameters Used in Model Development.

Symbol	Description	Initial Value and Range if Applicable	Reference
R_1	Width of electrolyte	2.80×10^{-4} m	APOC Sensor
R_2	Width of membrane	2.816×10^{-4} m	APOC Sensor
Z_1	Height of electrolyte	2.05×10^{-5} m	APOC Sensor
Z_2	Height of membrane	3.65×10^{-5} m	APOC Sensor
R_{AuI}	Inner radius of Au electrode	10.2×10^{-5} m	APOC Sensor
R_{AuO}	Outer radius of Au electrode	1.55×10^{-4} m	APOC Sensor
a	Mean radius of Cl^-	0.78 nm	(Raghunathan and Aluru, 2006)
$D_{\text{CO}_2\text{m}}$	Diffusion coefficient of CO_2 in membrane at 37 °C	$2.20 \pm 0.2 \times 10^{-9}$ m ² /s	(Yang and Kao, 2010)
$D_{\text{H}_2\text{CO}_3}$	Diffusion coefficient of H_2CO_3 at 37 °C	$2.70 \pm 0.2 \times 10^{-9}$ m ² /s	(Zeebe, 2011)
$D_{\text{HCO}_3^-}$	Diffusion coefficient of HCO_3^- at 37 °C	$1.57 \pm 0.2 \times 10^{-9}$ m ² /s	(Newman and Thomas-Alyea, 2004)
D_{H^+}	Diffusion coefficient of H^+ at 37 °C	$1.25 \pm 0.2 \times 10^{-8}$ m ² /s	(Newman and Thomas-Alyea, 2004)
D_{OH^-}	Diffusion coefficient of OH^- at 37 °C	$7.04 \pm 0.2 \times 10^{-9}$ m ² /s	(Newman and Thomas-Alyea, 2004)
$D_{\text{CO}_3^{2-}}$	Diffusion coefficient of CO_3^{2-} at 37 °C	$1.08 \pm 0.2 \times 10^{-9}$ m ² /s	(Zeebe, 2011)

D_{BQ}	Diffusion coefficient of BQ at 37 °C	$1.18 \pm 0.2 \times 10^{-9}$ m^2/s	(Green and Perry, 2008)
D_{H_2Q}	Diffusion coefficient of H_2Q at 37 °C	$1.18 \pm 0.2 \times 10^{-9}$ m^2/s	Green and Perry, 2008)
$K_{HCO_3^-}$	Equilibrium constant of HCO_3^- at 37 °C	6.30 ± 0.5 $\times 10^{-11} \frac{mol}{L}$	(Snokeyink and Jenkins, 1980) (Haynes, 2012)
$K_{H_2CO_3}$	Equilibrium constant of H_2CO_3 at 37 °C	5.78 ± 0.5 $\times 10^{-7} \frac{mol}{L}$	(Snokeyink and Jenkins, 1980) (Haynes, 2012)
K_{H_2O}	Equilibrium constant of H_2O at 37 °C	2.39 ± 0.5 $\times 10^{-14} \frac{mol}{L}$	(Snokeyink and Jenkins, 1980) (Haynes, 2012)
$[H_2CO_3]_0$	Initial concentration of H_2CO_3	APOC Company Confidential	
$[K^+]_0$	Initial concentration of K^+	APOC Company Confidential	
$[Cl^-]_0$	Initial concentration of Cl^-	APOC Company Confidential	
$[CO_3^{2-}]_0$	Initial concentration of CO_3^{2-}	APOC Company Confidential	
$[Na^+]_0$	Initial concentration of Na^+	APOC Company Confidential	
$[HCO_3^-]_0$	Initial concentration of HCO_3^-	APOC Company Confidential	
$[H^+]_0$	Initial concentration of H^+	APOC Company Confidential	
$[OH^-]_0$	Initial concentration of OH^-	APOC Company Confidential	
$[H_2O]_0$	Initial concentration of H_2O	APOC Company Confidential	
$[BQ]_0$	Initial concentration of BQ	APOC Company Confidential	
$[H_2Q]_0$	Initial concentration of H_2Q	APOC Company Confidential	
H	Henry's constant at 37 °C	0.230 ± 0.002 $\frac{mmol}{L \cdot kPa}$	(Burtis et al., 2006)
κ_{CO_2m}	Partition coefficient at 37 °C	1 ± 0.5	(Burtis et al., 2006)
k_{fAu}	Forward reaction rate constant at the Au electrode at 37 °C	505 ± 495 $\frac{m^7}{s \cdot mol^2}$	Estimated

$k_{f_{H_2CO_3}}$	Forward reaction rate constant for the dissociation of carbonic acid at 37 °C	$1000 \frac{1}{s}$	Assumed to be large
$k_{f_{HCO_3^-}}$	Forward reaction rate constant for the dissociation of bi carbonate at 37 °C	$1000 \frac{1}{s}$	Assumed to be large
$k_{f_{H_2O}}$	Forward reaction rate constant for the dissociation of water at 37 °C	$1000 \frac{1}{s}$	Assumed to be large
$k_{r_{HCO_3^-}}$	Reverse reaction rate constant for the dissociation of bicarbonate at 37 °C	$\frac{k_{f_{HCO_3^-}}}{K_{HCO_3^-}}$	Due to equilibrium ratio
$k_{r_{H_2CO_3}}$	Reverse reaction rate constant for the dissociation of carbonic acid at 37 °C	$\frac{k_{f_{H_2CO_3}}}{K_{H_2CO_3}}$	Due to equilibrium ratio
$k_{r_{H_2O}}$	Reverse reaction rate constant for the dissociation of water at 37 °C	$\frac{k_{f_{H_2O}}}{K_{H_2O}}$	Due to equilibrium ratio
$[NaHCO_3]_0$	Concentration of bicarbonate before time 0	$0.050 \frac{\text{mol}}{\text{L}}$	(Abbott Point of Care-d, 2012)
$[BQ]_0$	Concentration of BQ before time 0		(Abbott Point of Care-d, 2012)
$[CO_2]_0$	Concentration of CO_2 before time 0	$1 \times 10^{-5} \frac{\text{mol}}{\text{L}}$	(Manahan, 2005)
$\rho_{\text{pure solvent}}$	Density of water at 37 °C	$0.993333 \frac{\text{kg}}{\text{L}}$	(Colt, 2012)

Table 3: Table of PDEs.

3.1	$\frac{\partial [CO_2]_m}{\partial t} = D_{CO_2m} \left[\frac{1}{r} \frac{\partial}{\partial r} \left(r \frac{\partial [CO_2]_m}{\partial r} \right) + \frac{\partial^2 ([CO_2]_m)}{\partial^2 z} \right]$
3.2	$\frac{\partial [H_2CO_3]}{\partial t} = D_{H_2CO_3} \left[\frac{1}{r} \frac{\partial}{\partial r} \left(r \frac{\partial [H_2CO_3]}{\partial r} \right) + \frac{\partial^2 [H_2CO_3]}{\partial^2 z} \right] + k_{r_{H_2CO_3}} [H^+][HCO_3^-] - k_{f_{H_2CO_3}} [H_2CO_3]$

3.3	$\frac{\partial[HCO_3^-]}{\partial t} = D_{HCO_3^-} \left[\frac{1}{r} \frac{\partial}{\partial r} \left(r \frac{\partial[HCO_3^-]}{\partial r} \right) + \frac{\partial^2[HCO_3^-]}{\partial^2 z} \right]$ $+ k_{f_{NaHCO_3}}[NaHCO_3] - k_{r_{NaHCO_3}}[Na^+][HCO_3^-]$ $+ k_{f_{H_2CO_3}}[H_2CO_3] - k_{r_{H_2CO_3}}[H^+][HCO_3^-] + k_{r_{HCO_3^-}}[H^+][CO_3^{2-}]$ $- k_{f_{HCO_3^-}}[HCO_3^-]$
3.4	$\frac{\partial[H^+]}{\partial t} = D_{H^+} \left[\frac{1}{r} \frac{\partial}{\partial r} \left(r \frac{\partial[H^+]}{\partial r} \right) + \frac{\partial^2[H^+]}{\partial^2 z} \right] + k_{f_{H_2CO_3}}[H_2CO_3] - k_{r_{H_2CO_3}}[H^+][HCO_3^-] +$ $k_{f_{HCO_3^-}}[HCO_3^-] - k_{r_{HCO_3^-}}[H^+][CO_3^{2-}] + k_{f_{H_2O}}[H_2O] - k_{r_{H_2O}}[H^+][OH^-]$
3.5	$\frac{\partial[OH^-]}{\partial t} = D_{OH^-} \left[\frac{1}{r} \frac{\partial}{\partial r} \left(r \frac{\partial[OH^-]}{\partial r} \right) + \frac{\partial^2[OH^-]}{\partial^2 z} \right] + k_{f_{H_2O}}[H_2O] - k_{r_{H_2O}}[H^+][OH^-]$
3.6	$\frac{\partial[CO_3^{2-}]}{\partial t} = D_{CO_3^{2-}} \left[\frac{1}{r} \frac{\partial}{\partial r} \left(r \frac{\partial[CO_3^{2-}]}{\partial r} \right) + \frac{\partial^2[CO_3^{2-}]}{\partial^2 z} \right]$ $+ k_{f_{HCO_3^-}}[HCO_3^-] - k_{r_{HCO_3^-}}[H^+][CO_3^{2-}]$
3.7	$\frac{\partial[BQ]}{\partial t} = D_{BQ} \left[\frac{1}{r} \frac{\partial}{\partial r} \left(r \frac{\partial[BQ]}{\partial r} \right) + \frac{\partial^2[BQ]}{\partial^2 z} \right]$
3.8	$\frac{\partial[H_2Q]}{\partial t} = D_{H_2Q} \left[\frac{1}{r} \frac{\partial}{\partial r} \left(r \frac{\partial[H_2Q]}{\partial r} \right) + \frac{\partial^2[H_2Q]}{\partial^2 z} \right]$

Table 4: Boundary and Initial Conditions

4.1	4.1.1	$HP_{CO_2B} = [CO_2]_m _{r,Z_2}$
	4.1.2	$\kappa_{CO_2m}[CO_2]_m _{r,Z_1} = [H_2CO_3] _{r,Z_1}$
	4.1.3	$\frac{\partial[CO_2]_m}{\partial z} _{R_1 \leq r \leq R_2, z=0} = 0$
	4.1.4	$HP_{CO_2B} = [CO_2]_m _{R_2,z}$ (note that H is the Henry's law constant)
	4.1.5	$\kappa_{CO_2m}[CO_2]_m _{R_1,z} = [H_2CO_3] _{R_1,z}$

	4.1.6	$\left. \frac{\partial [CO_2]_m}{\partial r} \right _{r=0, z} = 0$
	4.1.7	$[CO_2]_m(0, r, z) = \frac{[H_2CO_3]_0}{\kappa_{CO_2m}}$
4.2	4.2.1	$D_{CO_2m} \left. \frac{\partial [CO_2]_m}{\partial z} \right _{r, z_1} = D_{H_2CO_3} \left. \frac{\partial [H_2CO_3]}{\partial z} \right _{r, z_1}$
	4.2.2	$\left. \frac{\partial [H_2CO_3]}{\partial z} \right _{r, z=0} = 0$
	4.2.3	$D_{CO_2m} \left. \frac{\partial [CO_2]_m}{\partial r} \right _{R_1, z} = D_{H_2CO_3} \left. \frac{\partial [H_2CO_3]}{\partial z} \right _{R_1, z}$
	4.2.4	$\left. \frac{\partial [H_2CO_3]}{\partial r} \right _{r=0, z} = 0$
	4.2.5	$[H_2CO_3](0, r, z) = [H_2CO_3]_0$
4.3	4.3.1	$\left. \frac{\partial [HCO_3^-]}{\partial z} \right _{r, z=Z_1} = 0$
	4.3.2	$\left. \frac{\partial [HCO_3^-]}{\partial z} \right _{r, z=0} = 0$
	4.3.3	$\left. \frac{\partial [HCO_3^-]}{\partial r} \right _{r=R_1, z} = 0$
	4.3.4	$\left. \frac{\partial [HCO_3^-]}{\partial r} \right _{r=0, z} = 0$
	4.3.5	$[HCO_3^-](0, r, z) = [HCO_3^-]_0$
4.4	4.4.1	$\left. \frac{\partial [H^+]}{\partial z} \right _{r, z=Z_1} = 0$
	4.4.2	$\left. \frac{\partial [H^+]}{\partial z} \right _{r < R_{AuI}, z=0} = 0$
	4.4.3	$D_{H^+} \left. \frac{\partial [H^+]}{\partial z} \right _{R_{AuI} < r < R_{AuO}, z=0} = 2\{k_{fAu}[H^+]^2[BQ] - k_{rAu}[H_2Q]\}$
	4.4.4	$\left. \frac{\partial [H^+]}{\partial z} \right _{r > R_{AuO}, z=0} = 0$

	4.4.5	$\left. \frac{\partial[H^+]}{\partial r} \right _{r=R_1, z} = 0$
	4.4.6	$\left. \frac{\partial[H^+]}{\partial r} \right _{r=0, z} = 0$
	4.4.7	$[H^+](\mathbf{0}, r, z) = [H^+]_0$
4.5	4.5.1	$\left. \frac{\partial[OH^-]}{\partial z} \right _{r, z=Z_1} = 0$
	4.5.2	$\left. \frac{\partial[OH^-]}{\partial z} \right _{r, z=0} = 0$
	4.5.3	$\left. \frac{\partial[OH^-]}{\partial r} \right _{r=R_1, z} = 0$
	4.5.4	$\left. \frac{\partial[OH^-]}{\partial r} \right _{r=0, z} = 0$
	4.5.5	$[OH^-](\mathbf{0}, r, z) = [OH^-]_0$
4.6	4.6.1	$\left. \frac{\partial[CO_3^{2-}]}{\partial z} \right _{r, z=Z_1} = 0$
	4.6.2	$\left. \frac{\partial[CO_3^{2-}]}{\partial z} \right _{r, z=0} = 0$
	4.6.3	$\left. \frac{\partial[CO_3^{2-}]}{\partial r} \right _{r=R_1, z} = 0$
	4.6.4	$\left. \frac{\partial[CO_3^{2-}]}{\partial r} \right _{r=0, z} = 0$
	4.6.5	$[CO_3^{2-}](\mathbf{0}, r, z) = [CO_3^{2-}]_0$
4.7	4.7.1	$\left. \frac{\partial[BQ]}{\partial z} \right _{r, z=Z_1} = 0$
	4.7.2	$\left. \frac{\partial[BQ]}{\partial z} \right _{r < R_{AuI}, z=0} = 0$
	4.7.3	$D_{BQ} \left. \frac{\partial[BQ]}{\partial z} \right _{R_{AuI} < r < R_{AuO}, z=0} = \{k_{f_{Au}}[H^+]^2[BQ] - k_{r_{Au}}[H_2Q]\}$
	4.7.4	$\left. \frac{\partial[BQ]}{\partial z} \right _{r > R_{AuO}, z=0} = 0$

	4.7.5	$\left. \frac{\partial[BQ]}{\partial r} \right _{r=R_1, z} = 0$
	4.7.6	$\left. \frac{\partial[BQ]}{\partial r} \right _{r=0, z} = 0$
	4.7.7	$[BQ](0, r, z) = [BQ]_0$
4.8	4.8.1	$\left. \frac{\partial[H_2Q]}{\partial z} \right _{r, z=Z_1} = 0$
	4.8.2	$\left. \frac{\partial[H_2Q]}{\partial z} \right _{r < R_{AuI}, z=0} = 0$
	4.8.3	$D_{H_2Q} \left. \frac{\partial[H_2Q]}{\partial z} \right _{R_{AuI} < r < R_{AuO}, z=0} = -\{k_{fAu}[H^+]^2[BQ] - k_{rAu}[H_2Q]\}$
	4.8.4	$\left. \frac{\partial[H_2Q]}{\partial z} \right _{r > R_{AuO}, z=0} = 0$
	4.8.5	$\left. \frac{\partial[H_2Q]}{\partial r} \right _{r=R_1, z} = 0$
	4.8.6	$\left. \frac{\partial[H_2Q]}{\partial r} \right _{r=0, z} = 0$
	4.8.7	$[H_2Q](0, r, z) = [H_2Q]_0$

2.2 Development of Material Balances and Boundary Conditions

The material balance equations – whether for species in the membrane, or the electrolyte, can be derived by considering an annular element of height Δz and thickness Δr as shown in Figure 9. The following material balance (in moles) can be written for any species of interest in this control volume (either within the membrane or within the electrolyte):

$$\begin{aligned} \text{Accumulation} = & \text{in} - \text{out} + \text{generated} - \text{consumed} \quad (13) \\ & + \text{migration due to potential} \end{aligned}$$



Figure 9: Differential element of height Δz and thickness Δr .

Due to Assumption 1.13, the term migration due to potential is neglected. The only species whose concentration needs to be modeled within the gas-permeable membrane is the dissolved CO_2 . Even though water can also permeate the membrane, it is assumed that there is no appreciable transport of water across the membrane and that the water concentration in the electrolyte is constant (i.e., see Assumptions 1.6 and 1.7 in Table 1).

In the membrane, CO_2 diffuses in at the outer surface of the annulus (i.e., at $r+\Delta r$) and out at the inner surface (i.e., at r). CO_2 also diffuses in at the upper surface (i.e., at $z+\Delta z$) and out at the lower surface (i.e., at z). No reactions occur within the small element, so there is neither generation nor consumption of CO_2 . Let $[\text{CO}_2]_m$ be the concentration of

dissolved CO₂ in mol/m³ in the membrane and D_{CO_2m} be the corresponding diffusivity in m²/s. The number of moles of CO₂ that diffuse into the control volume at $r+\Delta r$ during a short period of time Δt is:

$$D_{CO_2m} 2\pi(r + \Delta r)\Delta z \left. \frac{\partial [CO_2]_m}{\partial r} \right|_{r+\Delta r} \Delta t$$

The number of moles of CO₂ that diffuse out at r is:

$$D_{CO_2m} 2\pi r \Delta z \left. \frac{\partial [CO_2]_m}{\partial r} \right|_r \Delta t$$

The number of moles diffusing in at $z+\Delta z$ is:

$$D_{CO_2m} 2\pi r \Delta r \left. \frac{\partial [CO_2]_m}{\partial z} \right|_{z+\Delta z} \Delta t$$

The number of moles diffusing out at z is:

$$D_{CO_2m} 2\pi r \Delta r \left. \frac{\partial [CO_2]_m}{\partial z} \right|_z \Delta t$$

The number of moles of CO₂ that accumulate within the control volume within the period Δt is:

$$2\pi r \Delta r \Delta z ([CO_2]_m|_{t+\Delta t} - [CO_2]_m|_t)$$

As a result, Equation (13) becomes:

$$2\pi r \Delta r \Delta z ([CO_2]_m|_{t+\Delta t} - [CO_2]_m|_t) = \quad (14)$$

$$D_{CO_2m} 2\pi(r + \Delta r)\Delta z \left. \frac{\partial[CO_2]_m}{\partial r} \right|_{r+\Delta r} \Delta t - D_{CO_2m} 2\pi r \Delta z \left. \frac{\partial[CO_2]_m}{\partial r} \right|_r \Delta t +$$

$$D_{CO_2m} 2\pi r \Delta r \left. \frac{\partial[CO_2]_m}{\partial z} \right|_{z+\Delta z} \Delta t - D_{CO_2m} 2\pi r \Delta r \left. \frac{\partial[CO_2]_m}{\partial z} \right|_z \Delta t$$

Dividing both sides by $2\pi\Delta r\Delta z\Delta t$ gives:

$$r \frac{\Delta[CO_2]_m}{\Delta t} = D_{CO_2m} \frac{(r + \Delta r) \left. \frac{\partial[CO_2]_m}{\partial r} \right|_{r+\Delta r} - r \left. \frac{\partial[CO_2]_m}{\partial r} \right|_r}{\Delta r} \quad (15)$$

$$+ D_{CO_2m} r \frac{\left(\left. \frac{\partial[CO_2]_m}{\partial z} \right|_{z+\Delta z} - \left. \frac{\partial[CO_2]_m}{\partial z} \right|_z \right)}{\Delta z}$$

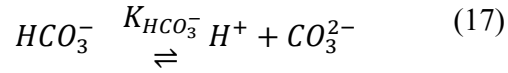
Taking the limit as $\Delta t, \Delta r, \Delta z$ approach 0 gives:

$$r \frac{\partial[CO_2]_m}{\partial t} = D_{CO_2m} \frac{\partial \left(r \frac{\partial[CO_2]_m}{\partial r} \right)}{\partial r} + D_{CO_2m} r \frac{\partial \left(\frac{\partial[CO_2]_m}{\partial z} \right)}{\partial z} \quad (16)$$

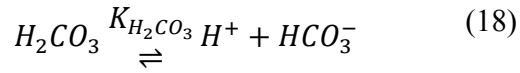
which can be manipulated to give PDE (3.1) in Table 3.

The concentrations of all chemical species (H_2CO_3 , HCO_3^- , H^+ , OH^- , CO_3^{2-} , BQ, and H_2Q) in the electrolyte are also tracked using PDEs and algebraic equations to model the transport of these species. Diffusion is assumed to be only due to concentration gradients, and not due to potential gradients (i.e., see Assumption 1.13 of Table 1). These material balance PDEs differ from the membrane balance by the presence of reactions taking place in the electrolyte.

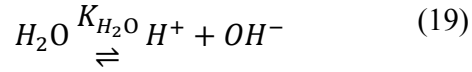
The reactions in the electrolyte are governed by the following chemical equilibria and their equilibrium constants at standard conditions are well known (Maas et.al., 1971; Snokeyink and Jenkins, 1980; Wimberley et.al., 1985):



$$K_{HCO_3^-} = \frac{[H^+][CO_3^{2-}]}{[HCO_3^-]}$$



$$K_{H_2CO_3} = \frac{[H^+][HCO_3^-]}{[H_2CO_3]}$$



$$K_{H_2O} = \frac{[H^+][OH^-]}{[H_2O]}$$

Equilibrium constants at 37 °C can be determined from the integrated form of the van't Hoff equation using the values at the standard conditions:

$$\ln\left(\frac{K}{K_{ref}}\right) = \frac{-\Delta H^o}{R} \left[\frac{1}{T_{ref}} - \frac{1}{T} \right] \quad (20)$$

where R is the universal gas constant $8.314 \frac{J}{K \cdot mol}$, T_{ref} is at 298.15 K, and T is 310.15

K . ΔH^o is the standard heat of reaction in kJ/mol at 25 °C and 1 atm and the values of ΔH^o s for equilibrium reactions (17) to (19) are listed in Table 5(Haynes, 2012). The reactions are endothermic.

Table 5: Heat of Reactions

Equilibrium Reactions	ΔH^o (kJ/mol)
$HCO_3^- \xrightleftharpoons{K_{HCO_3^-}} H^+ + CO_3^{2-}$ (17)	14.7
$H_2CO_3 \xrightleftharpoons{K_{H_2CO_3}} H^+ + HCO_3^-$ (18)	9.15
$H_2O \xrightleftharpoons{K_{H_2O}} H^+ + OH^-$ (19)	55.8

The resulting values at 37 °C are provided in Table 2 (Standard, 2012; Manahan, 2005).

The equilibrium constants in Equations (17) to (19) are ratios of the forward and reverse rate constants for these dissociation reactions:

$$K_{HCO_3^-} = \frac{k_{f_{HCO_3^-}}}{k_{r_{HCO_3^-}}} \quad (21)$$

$$K_{H_2CO_3} = \frac{k_{f_{H_2CO_3}}}{k_{r_{H_2CO_3}}} \quad (22)$$

$$K_{H_2O} = \frac{k_{f_{H_2O}}}{k_{r_{H_2O}}} \quad (23)$$

In the electrolyte, H_2CO_3 (which is CO_2 dissolved in the aqueous phase) enters the outer surface of an annulus at $r+\Delta r$ and leaves the inner surface at r . H_2CO_3 also diffuses in at

the upper surface (i.e., at $z+\Delta z$) and out at the lower surface (i.e., at z). H_2CO_3 is also consumed and generated via equilibrium reaction (1). Let $[H_2CO_3]$ be the concentration of dissolved CO_2 in mol/m^3 in the electrolyte and $D_{H_2CO_3}$ be the corresponding diffusivity in m^2/s . The number of moles of H_2CO_3 that diffuse into the control volume at $r+\Delta r$ during a short period of time Δt is:

$$D_{H_2CO_3} 2\pi(r + \Delta r)\Delta z \left. \frac{\partial [H_2CO_3]}{\partial r} \right|_{r+\Delta r} \Delta t$$

The number of moles of H_2CO_3 that diffuse out at r is:

$$D_{H_2CO_3} 2\pi r \Delta z \left. \frac{\partial [H_2CO_3]}{\partial r} \right|_r \Delta t$$

The number of moles diffusing in at $z+\Delta z$ is:

$$D_{H_2CO_3} 2\pi r \Delta r \left. \frac{\partial [H_2CO_3]}{\partial z} \right|_{z+\Delta z} \Delta t$$

The number of moles diffusing out at z is:

$$D_{H_2CO_3} 2\pi r \Delta r \left. \frac{\partial [H_2CO_3]}{\partial z} \right|_z \Delta t$$

The number of moles of H_2CO_3 consumed is:

$$k_{f_{H_2CO_3}} 2\pi r \Delta r \Delta z [H_2CO_3] \Delta t$$

The number of moles of H_2CO_3 generated is:

$$k_{r_{H_2CO_3}} 2\pi\Delta r\Delta z [H^+][HCO_3^-]\Delta t$$

The number of moles of H_2CO_3 that accumulate within the control volume during the period Δt is:

$$2\pi\Delta r\Delta z ([H_2CO_3]|_{t+\Delta t} - [H_2CO_3]|_t)$$

As a result, the material balance Equation (13) for H_2CO_3 in the electrolyte becomes:

$$\begin{aligned} & 2\pi\Delta r\Delta z ([H_2CO_3]|_{t+\Delta t} - [H_2CO_3]|_t) \tag{24} \\ &= D_{H_2CO_3} 2\pi(r + \Delta r)\Delta z \left. \frac{\partial [H_2CO_3]}{\partial r} \right|_{r+\Delta r} \Delta t \\ &\quad - D_{H_2CO_3} 2\pi r\Delta z \left. \frac{\partial [H_2CO_3]}{\partial r} \right|_r \Delta t \\ &\quad + D_{H_2CO_3} 2\pi r\Delta r \left. \frac{\partial [H_2CO_3]}{\partial z} \right|_{z+\Delta z} \Delta t \\ &\quad - D_{H_2CO_3} 2\pi r\Delta r \left. \frac{\partial [H_2CO_3]}{\partial z} \right|_z \Delta t \\ &\quad + k_{r_{H_2CO_3}} 2\pi\Delta r\Delta z [H^+][HCO_3^-]\Delta t \\ &\quad - k_{f_{H_2CO_3}} 2\pi\Delta r\Delta z [H_2CO_3]\Delta t \end{aligned}$$

Dividing both sides by $2\pi\Delta r\Delta z\Delta t$ gives:

The number of moles of H_2CO_3 that accumulate within the control volume during the period Δt is:

$$2\pi\Delta r\Delta z ([H_2CO_3]|_{t+\Delta t} - [H_2CO_3]|_t)$$

As a result, the material balance Equation (13) for H_2CO_3 in the electrolyte becomes:

$$\begin{aligned}
& 2\pi r \Delta r \Delta z ([H_2CO_3]|_{t+\Delta t} - [H_2CO_3]|_t) \\
&= D_{H_2CO_3} 2\pi(r + \Delta r) \Delta z \left. \frac{\partial [H_2CO_3]}{\partial r} \right|_{r+\Delta r} \Delta t \\
&\quad - D_{H_2CO_3} 2\pi r \Delta z \left. \frac{\partial [H_2CO_3]}{\partial r} \right|_r \Delta t \\
&\quad + D_{H_2CO_3} 2\pi r \Delta r \left. \frac{\partial [H_2CO_3]}{\partial z} \right|_{z+\Delta z} \Delta t \\
&\quad - D_{H_2CO_3} 2\pi r \Delta r \left. \frac{\partial [H_2CO_3]}{\partial z} \right|_z \Delta t \\
&\quad + k_{r_{H_2CO_3}} 2\pi r \Delta r \Delta z [H^+][HCO_3^-] \Delta t \\
&\quad - k_{f_{H_2CO_3}} 2\pi r \Delta r \Delta z [H_2CO_3] \Delta t
\end{aligned} \tag{25}$$

Dividing both sides by $2\pi r \Delta r \Delta z \Delta t$ gives:

$$\begin{aligned}
& \frac{r(\partial [H_2CO_3]|_{t+\Delta t} - \partial [H_2CO_3]|_t)h}{\Delta t} \\
&= D_{H_2CO_3} \frac{(r + \Delta r) \left. \frac{\partial [H_2CO_3]}{\partial r} \right|_{r+\Delta r} - r \left. \frac{\partial [H_2CO_3]}{\partial r} \right|_r}{\Delta r} \\
&\quad + D_{H_2CO_3} r \frac{\left(\left. \frac{\partial [H_2CO_3]}{\partial z} \right|_{z+\Delta z} - \left. \frac{\partial [H_2CO_3]}{\partial z} \right|_z \right)}{\Delta z} \\
&\quad + k_{r_{H_2CO_3}} r [H^+][HCO_3^-] - k_{f_{H_2CO_3}} r [H_2CO_3]
\end{aligned} \tag{26}$$

Taking the limit as Δt , Δr , Δz approach 0:

$$r \frac{\partial [H_2CO_3]}{\partial t} = D_{H_2CO_3} \frac{\partial \left(r \frac{\partial [H_2CO_3]}{\partial r} \right)}{\partial r} + D_{H_2CO_3} r \frac{\partial \left(\frac{\partial [H_2CO_3]}{\partial z} \right)}{\partial z} \quad (27)$$

$$+ k_{r_{H_2CO_3}} r [H^+] [HCO_3^-] - k_{f_{H_2CO_3}} r [H_2CO_3]$$

which is being manipulated to Equation (3.2) in Table 3.

The material balance PDEs for the remaining six species in the electrolyte were derived in an analogous fashion and are listed as Equations (3.3) to (3.8) in Table 3. Note that since there are no reactions of BQ and H₂Q in the bulk of the electrolyte, their PDEs resemble the PDE for CO₂ in the membrane. The electrochemical reaction at the Au electrode appears in BCs (4.4.3), (4.7.3) and (4.8.3) in Table 4.

Figure 10 is a schematic of the sensor that is helpful when deriving the BCs. R_{AuI} is the radial distance to the inner edge of the gold electrode (in m) and R_{AuO} is the radial distance to the outer edge. R_I is the radial distance to the inner edge of the membrane and R_2 is radial distance to the outer edge of the membrane. Similarly, Z_I is the vertical distance to the bottom of the membrane and Z_2 is the vertical distance to the top surface of the membrane. Some of the BCs are also indicated by numbers and arrows in Table 3 on the figure.

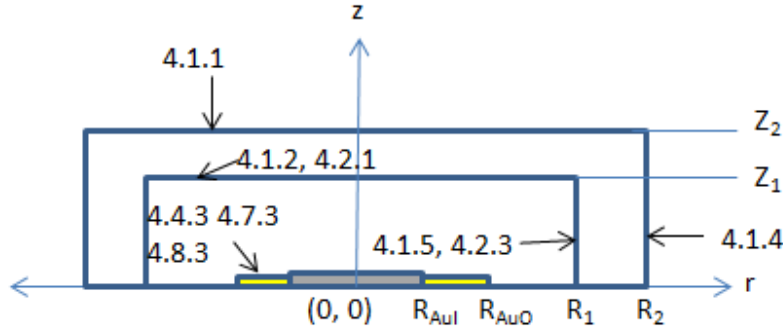


Figure 10: Schematic of pCO₂ Sensor

The upper (outer) surface of the gas-permeable membrane is in contact with the blood or the calibrant fluid. At this outer edge of the membrane, the CO₂ partial pressure in the blood is assumed to be the same as the bulk CO₂ partial pressure in the blood sample (see Assumption 1.2 in Table 1). Concentration gradients within the blood sample are neglected as is the depletion of CO₂ in the blood over time due to the small volumes of the membrane and electrolyte compared to the volume of the blood. At the outer membrane surface in contact with blood, the partial pressure of CO₂ is assumed to be in equilibrium with the CO₂ concentration just inside the membrane (at (t, r, Z_2) and (t, R_2, z) which gives rise to BCs (4.1.1) and (4.1.4) in Table 4 where H is Henry's constant in mmol/ kPa⁻¹ m⁻³.

The CO₂ concentration in the membrane at its inner surface is assumed to be in equilibrium with the H₂CO₃ in the neighboring electrolyte, which gives rise to BCs 4.1.2 and 4.1.5, for CO₂ where κ_{CO_2m} is a partition coefficient. Initial condition (4.1.7) indicates that the initial [CO₂] in the membrane is in equilibrium with the initial concentration of H₂CO₃ in the electrolyte [H₂CO₃]₀.

BC 4.2.1 for H_2CO_3 at the upper surface of the electrolyte can be derived by considering a ring with thickness Δr on the flat upper surface of the electrolyte, as shown in Figure 11. The number of moles of CO_2 that diffuse into the membrane surface during a short period of time Δt is equal to the number of moles of H_2CO_3 that diffuse from the surface and into the electrolyte:

$$D_{CO_2m} 2\pi r \Delta r \left. \frac{\partial [CO_2]_m}{\partial z} \right|_{r,z_1} \Delta t = D_{H_2CO_3} 2\pi r \Delta r \left. \frac{\partial [H_2CO_3]}{\partial z} \right|_{r,z_1} \Delta t \quad (28)$$

Dividing by $2\pi r \Delta r \Delta t$ gives BC 4.2.1 in Table 4. A similar argument is used to obtain BC 4.2.3.



Figure 11: Small ring with thickness Δr

BCs for other species at the interface between the electrolyte and the gas-permeable membrane are zero-flux conditions because none of the other species can diffuse into or out of the membrane. BC (4.2.4) arises from the radial symmetry of the electrolyte, which results in a minimum in $[H_2CO_3]$ at $r=0$.

The bottom surface of the electrolyte consists of two different regions: the inert surface and the Au electrode surface. For the purposes of this model, the Ag/AgCl electrode is treated as an inert surface (see Assumptions 1.10 and 1.12 in Table 1).

For the inert portions of the bottom surface of the electrolyte, there is no diffusion of any species in the z direction, resulting in BCs (4.3.2), (4.4.2), (4.5.2), (4.6.2), and (4.7.2) in Table 4.

At the Au electrode surface, H^+ and BQ diffuse from the electrolyte onto the Au surface to react with electrons supplied by the Au to produce H_2Q according to chemical equilibrium reaction (2), resulting in BCs (4.4.3) and (4.7.3). The H_2Q that is produced diffuses away from the Au electrode into the bulk electrolyte solution, resulting in BC (4.8.3).

The potential of the Au electrode changes when BQ reacts with H^+ and electrons as described by Equation (7), resulting in a change in k_{rAu} with time, due to a change in the equilibrium constant $K_{Au\ Surface}$. Assuming that k_{fAu} remains constant (See Assumption 1.17 in Table 1):

$$k_{rAu} = \frac{k_{fAu}}{K_{Au\ Surface}} \quad (29)$$

Since the forward and reverse reaction rates are very fast and the concentrations are in equilibrium defined by $K_{Au\ Surface}$ which is changing in time and leading to changes in the concentration ratio, we can assume that:

$$K_{Au\ Surface} = \frac{[H_2Q]_{Au}}{[BQ]_{Au}[H^+]_{Au}^2} \quad (30)$$

where the subscript Au indicates an average concentration over the surface of the Au electrode, which is computed using the “Boundary Probe” function in COMSOLTM that is used to compute the average voltage response for the forward and reverse $BQ \rightleftharpoons H_2Q$ reaction. Additional details on the implementation in COMSOLTM are in the next

section, 2.3. The updated potential, E , between the Au and Ag/AgCl electrode can then be calculated from:

$$K_{Au\ Surface} = e^{\frac{-E + 0.699 - \left[0.22233 - \frac{RT}{nF} \ln(a_{Cl^-})\right]}{\frac{RT}{nF}}} \quad (31)$$

which is obtained by rearranging Equation (10).

Initial concentrations for species in the electrolyte are determined from the known initial concentration of $NaHCO_3$ in the electrolyte recipe (see Table 2) and the known carbon dioxide dissolved (H_2CO_3) in water at 25 °C which is 10^{-5} mol/L. Since half the water in the electrolyte is assumed to evaporate and the concentration of H_2CO_3 during manufacturing is constant, the known concentration of the buffer is doubled. The initial concentrations of all species in the electrolyte (except for BQ and H_2Q) can be determined from:

$$[H_2CO_3]_0 + [CO_3^{2-}]_0 + [HCO_3^-]_0 = [NaHCO_3]_{0-} + [H_2CO_3]_{0-} \quad (32)$$

$$[H_2CO_3]_0 + 2[HCO_3^-]_0 + [H^+]_0 - [OH^-]_0 = [NaHCO_3]_{0-} + 2[H_2CO_3]_{0-} \quad (33)$$

Calculation of the initial conditions for BQ and H_2Q requires Equation (34) and the following mass balance:

$$[BQ]_{0-} = [BQ]_0 + [H_2Q]_0 \quad (34)$$

and the initial value of E is known in mV (APOC Company Confidential) given:

$$E_{known} = 0.699 - \frac{RT}{nF} \ln \left(\frac{[H_2Q]_0}{[BQ]_0[H^+]_0} \right) - \left[0.22233 - \frac{RT}{nF} \ln(a_{Cl^-}) \right] \quad (35)$$

a_{Cl^-} is the activity or effective concentration of chloride ion, which can be calculated using (Newman and Thomas-Alyea, 2004):

$$a_{Cl^-} = \gamma_{Cl^-} [Cl^-] \quad (36)$$

where γ_{Cl^-} is the activity coefficient of chloride ion (Newman and Thomas-Alyea, 2004):

$$\gamma_{Cl^-} = e^{\left(\frac{-z_i^2 \alpha \sqrt{I}}{1 + Ba\sqrt{I}} \right)} \quad (37)$$

$z_i = -1$ is the charge number for Cl^- , α is one of the Debye-Hückel parameters for aqueous

solutions in $\sqrt{\frac{kg}{mol}}$, B is the other Debye-Hückel parameter for aqueous solutions in $\frac{\sqrt{\frac{kg}{mol}}}{nm}$,

and a is the mean diameter of the hydrated chloride ion in nm.

I is the molal ionic strength of the solution in $\frac{mol}{kg}$ calculated from:

$$I = \frac{I'}{\rho_{pure\ solvent}} \quad (38)$$

where I' is the molar ionic strength of the solutions in $\frac{mol}{L}$ and $\rho_{pure\ solvent}$ is the density

of the pure solvent in $\frac{kg}{L}$. The molar ionic strength is calculated from :

$$I' = \frac{1}{2} \sum_i z_i^2 c_i \quad (39)$$

where z_i is the charge number of species i and c_i is the concentration of species i in $\frac{mol}{L}$.

Two Debye-Hückel parameters, α and B at 37 °C, are required to calculate I'. These values were obtained by fitting a quadratic using values of the two Debye-Hückel parameters at the temperatures listed below in Table 6 (Newman and Thomas-Alyea, 2004):

Table 6: Values of α from 273.15 K to 348.15 K.

T (K)	$\frac{1}{T} \left(\frac{1}{K}\right)$	$\alpha \left(\sqrt{\frac{kg}{mol}}\right)$	B $\left(\frac{\sqrt{kg}}{mol \cdot nm}\right)$
273.15	0.003661	1.1324	3.248
298.15	0.003354	1.1762	3.287
323.15	0.003095	1.2300	3.326
348.15	0.002872	1.2949	3.368

Curves of best fit were estimated using linear least squares regression:

$$\hat{\alpha} = 139117 \left(\frac{1}{T}\right)^2 - 1113.9 \frac{1}{T} + 3.3461$$

$$\hat{B} = 56951 \left(\frac{1}{T}\right)^2 - 523.56 \frac{1}{T} + 4.4017$$

as shown in Figure 12:

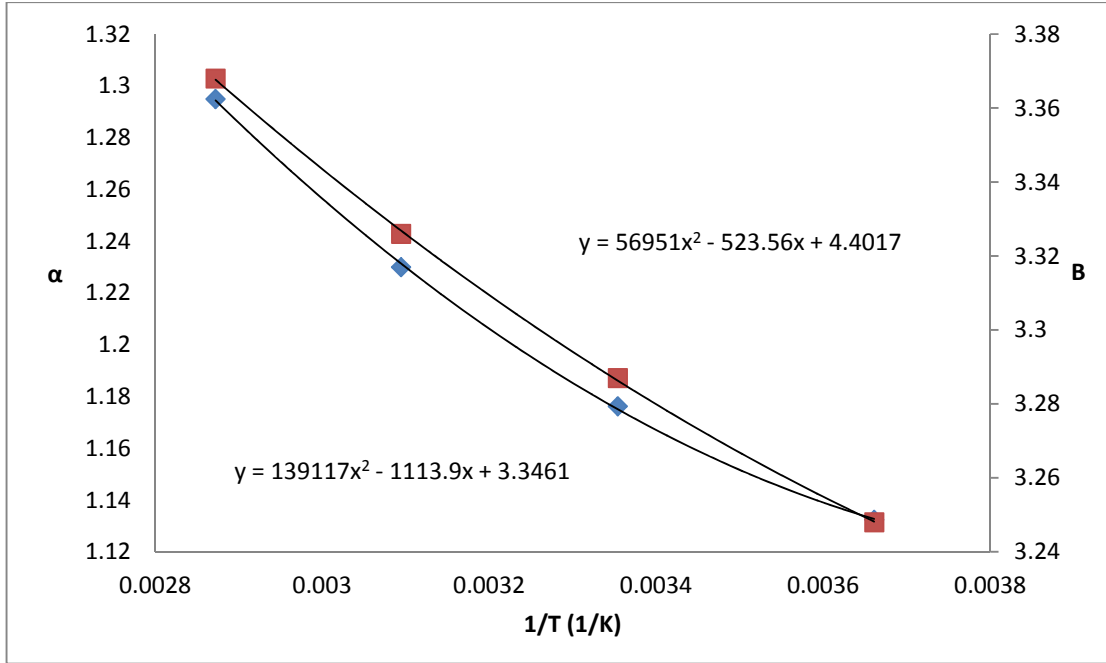


Figure 12: Curves of best fit for α and B.

giving $\alpha = 1.2008 \sqrt{\frac{kg}{mol}}$ and $B = 3.3057 \sqrt{\frac{kg}{nm}}$ at 37 °C.

The value $I' = 0.98$ shown in Table 2 was obtained from:

$$I' = \frac{1}{2} \{ (1)^2 [K^+]_0 + (-1)^2 [Cl^-]_0 + (1)^2 [Na^+]_0 + (-1)^2 [HCO_3^-]_0 + (-2)^2 [CO_3^{2-}]_0 + (1)^2 [H^+]_0 + (-1)^2 [OH^-]_0 \} \quad (40)$$

The only remaining unknowns in Equation (33) are $[H_2Q]_0$ and $[BQ]_0$. As a result Equation (33) can be combined with Equation (32) to obtain the initial conditions for the quinones.

The ionic diffusivities listed above are for ions in pure water. The true diffusivities in the electrolyte may be lower due to the fact that 10% of the electrolyte by weight is sucrose, which increases the viscosity of electrolyte solution. In order to maintain electroneutrality

in the electrolyte, ions tend to diffuse in pairs. In conclusion, the diffusion of a cation and its counter anion can be lumped together to obtain a reasonable diffusion coefficient for the corresponding ion pair. For example, the most probable anion that H^+ will diffuse with is HCO_3^- because it is the most abundant anion in the electrolyte. There is about a million time more HCO_3^- ions than H^+ ions. Therefore, the ion pair diffusion coefficient for H^+ and HCO_3^- should be approximately the lower value of their two diffusivities, which is $1.48 \times 10^{-9} \text{ m}^2/\text{s}$. Similarly, OH^- should have approximately the same diffusivity as Na^+ in the solution because Na^+ is the most abundant cation. Table 7 lists the corresponding diffusivity parameters used in the simulations.

Table 7: Lumped Diffusion Coefficients Used in Model

Diffusivity	Value
D_{CO_2m}	$2.20 \times 10^{-9} \text{ m}^2/\text{s}$
$D_{H_2CO_3}$	$2.70 \times 10^{-9} \text{ m}^2/\text{s}$
$D_{H^+} = D_{HCO_3^-}$	$1.48 \times 10^{-9} \text{ m}^2/\text{s}$
$D_{OH^-} = D_{H^+}$	$1.79 \times 10^{-9} \text{ m}^2/\text{s}$
$D_{CO_3^{2-}} = D_{HCO_3^-}$	$1.48 \times 10^{-9} \text{ m}^2/\text{s}$
$D_{BQ} = D_{H_2Q}$	$1.18 \times 10^{-9} \text{ m}^2/\text{s}$

2.3 Model Implementation in COMSOL™:

COMSOL™ is a finite element method (FEM) tool for numerically solving PDEs. A solution is computed by discretizing the domain into elements so that the PDEs can be converted to algebraic equations. The density of the elements in the domain can have an effect on both the accuracy of the solution and the computation time of the model. The

“user controlled mesh” was used in COMSOLTM and a maximum element size of 0.8 μm and a relative tolerance of 1×10^{-7} s for the time were used for the simulations (See Appendix). The solver used in this thesis was the MUMPS (MULTifrontal Massively Parallel sparse direct Solver). This uses a multifrontal method, which is a version of Gaussian elimination for a large system of equations which arises from the finite element method.

Since numerical solutions are approximate, a certain amount of error is associated with the calculations. It is important to analyze the solution to determine the reliability of the results. At the same time, it is important to consider the typical magnitudes of measurement errors that would be encountered for the dependent variables, such as the species concentrations and potential. In the discussion that follows, an overview is presented of how the model was implemented in COMSOLTM to assist future users of the model, and those wishing to reproduce the results. COMSOLTM version 4.3.0 was used for the simulations in this thesis.

The COMSOLTM tree structure for the model implementation is shown in Figure 13. Under the “Global Definitions” tab, there is a list of parameters (see Table 8) and a list of variables (see Table 9) that appear in the model. Parameters such as the partition coefficient κ_{CO_2m} , the equilibrium constant $K_{H_2CO_3}$ and the diffusion coefficient D_{H^+} are defined in the parameter list. Calculated variables such as K_{Au} (K_{Au} in COMSOLTM instead of $K_{Au_{surface}}$ for simplicity) and $k_{r_{Au}}$ are defined in the variable list. At time zero, when the calibrant fluid first contacts the membrane, K_{Au} is computed from Equation (33)

as a function of the known initial voltage response. Thereafter, K_{Au} is computed from Equation (30).

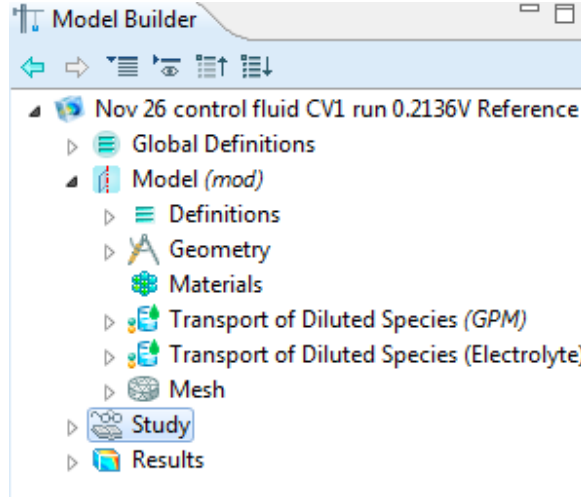


Figure 13: Tree structure of the Transport of Diluted Species Modules

Table 8: Parameter List in COMSOL™.

Symbol	Description	Value	Reference
D_{CO_2m}	Diffusion coefficient of CO_2 in membrane at 37 °C	$2.20 \times 10^{-9} \text{ m}^2/\text{s}$	(Yang and Kao, 2010)
$D_{H_2CO_3}$	Diffusion coefficient of H_2CO_3 at 37 °C	$2.70 \times 10^{-9} \text{ m}^2/\text{s}$	(Zeebe, 2011)
D_{H^+}	Diffusion coefficient of H^+ at 37 °C	$1.48 \times 10^{-9} \text{ m}^2/\text{s}$	(Newman and Thomas-Alyea, 2004)
D_{Na^+}	Diffusion coefficient of Na^+ at 37 °C	$1.79 \times 10^{-9} \text{ m}^2/\text{s}$	(Newman and Thomas-Alyea, 2004)
D_{BQ}	Diffusion coefficient of BQ at 37 °C	$1.18 \times 10^{-9} \text{ m}^2/\text{s}$	(Green and Perry, 2008)
$K_{HCO_3^-}$	Equilibrium constant of HCO_3^- at 37 °C	$6.30 \times 10^{-11} \frac{\text{mol}}{\text{L}}$	(Snokeyink and Jenkins, 1980) (Haynes, 2012)
$K_{H_2CO_3}$	Equilibrium constant of H_2CO_3 at 37 °C	$5.78 \times 10^{-7} \frac{\text{mol}}{\text{L}}$	(Snokeyink and Jenkins, 1980) (Haynes, 2012)
K_{H_2O}	Equilibrium constant of H_2O at 37 °C	$2.39 \times 10^{-14} \frac{\text{mol}}{\text{L}}$	(Snokeyink and Jenkins, 1980) (Haynes, 2012)
$[H_2CO_3]_0$	Initial concentration of H_2CO_3	APOC Company Confidential	

$[K^+]_0$	Initial concentration of K^+	APOC Company Confidential	
$[Cl^-]_0$	Initial concentration of Cl^-	APOC Company Confidential	
$[CO_3^{2-}]_0$	Initial concentration of CO_3^{2-}	APOC Company Confidential	
$[Na^+]_0$	Initial concentration of Na^+	APOC Company Confidential	
$[HCO_3^-]_0$	Initial concentration of HCO_3^-	APOC Company Confidential	
$[H^+]_0$	Initial concentration of H^+	APOC Company Confidential	
$[OH^-]_0$	Initial concentration of OH^-	APOC Company Confidential	
$[H_2O]_0$	Initial concentration of H_2O	APOC Company Confidential	
$[BQ]_0$	Initial concentration of BQ	APOC Company Confidential	
$[H_2Q]_0$	Initial concentration of H_2Q	APOC Company Confidential	
H	Henry's constant at 37 °C	$0.230 \frac{mmol}{L \cdot kPa}$	(Burtis et al., 2006)
κ_{CO_2m}	Partition coefficient at 37 °C	1	(Burtis et al., 2006)
$k_{f_{Au}}$	Forward reaction rate constant at the Au electrode at 37 °C	$600 \frac{m^7}{s \cdot mol^2}$	Estimated
$k_{f_{H_2CO_3}}$	Forward reaction rate constant for the dissociation of carbonic acid at 37 °C	$1000 \frac{1}{s}$	Assumed to be large
$k_{f_{HCO_3^-}}$	Forward reaction rate constant for the dissociation of bicarbonate at 37 °C	$1000 \frac{1}{s}$	Assumed to be large
$k_{f_{H_2O}}$	Forward reaction rate constant for the dissociation of water at 37 °C	$1000 \frac{1}{s}$	Assumed to be large
$k_{r_{HCO_3^-}}$	Reverse reaction rate constant for the dissociation of bicarbonate at 37 °C	$\frac{k_{f_{HCO_3^-}}}{K_{HCO_3^-}}$	Due to equilibrium ratio
$k_{r_{H_2CO_3}}$	Reverse reaction rate constant for the dissociation of carbonic acid at 37 °C	$\frac{k_{f_{H_2CO_3}}}{K_{H_2CO_3}}$	Due to equilibrium ratio

$k_{r_{H_2O}}$	Reverse reaction rate constant for the dissociation of water at 37 °C	$\frac{k_{f_{H_2O}}}{K_{H_2O}}$	Due to equilibrium ratio
----------------	---	---------------------------------	--------------------------

Table 9: Variable List

Variables	
Name	Expression
K_Au	$\exp((0.699[V]-E-E_{reference})/(R*T/(2*F)))[m^6/mol^2]$
kr_Au	k_{f_Au}/K_Au
E	$(0.699[V]-R*T/2/F*\log((mod1.C_{H2Q}/1000)/((mod1.C_{B...}$

As noted earlier, an average voltage response over the Au electrode surface is required for reaction (7) and Equation (10) and this is accomplished using a COMSOL™ Boundary Probe function that is specified in the “Definitions” tab under the “Model” tab, as shown in Figure 14.

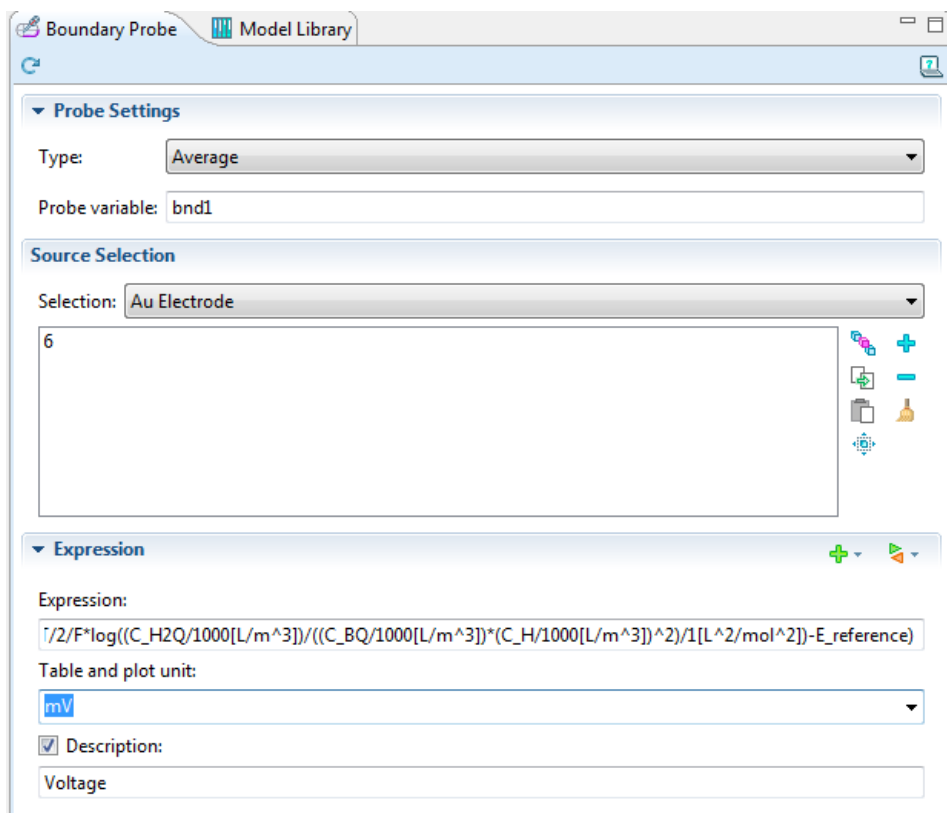


Figure 14: Voltage response at the Au electrode

Under the “Geometry” tab the layout of the domain in Figure 15 is specified using 2-D axisymmetric settings. Note that the corresponding dimensions are specified as parameters in Table 9. Nothing was defined under the “Material” tab because all parameters relating to material characteristics, such as the partition coefficient and diffusion coefficients, are defined in the parameter list.

PDEs as well as boundary and initial conditions were entered in COMSOLTM using the Diffusion of Diluted Species Module in the library module. Two modules were created: one for the gas-permeable membrane, and another for the electrolyte (see Figure 13). In the Transport of Diluted Species (GPM) module that was defined (GPM stands for gas permeable membrane) only one dependent variable was specified because only one species diffuses within the membrane (i.e., CO_{2m}). In the Transport of Diluted Species (Electrolyte) module that was defined, seven dependent variables were specified because there are seven PDE material balances for this part of the domain (i.e., balances on H₂CO₃, HCO₃⁻, H⁺, OH⁻, CO₃²⁻, BQ, and H₂Q shown in Table 3). The Transport of Diluted Species Module library automatically builds terms in the PDEs associated with diffusion of each species, according to the specifications for each of the modules of this type that are defined (e.g., GPM or Electrolyte). These are stored as Transport of Dilute Species modules.

Under the Transport of Diluted Species modules there are sub-tabs as shown in Figure 15. Under the “Diffusion GPM” tab, the label for the diffusion coefficient, $D_{CO_{2m}}$, was entered. Similarly, diffusion coefficients for species in “Transport of Diluted Species (Electrolyte)” were defined under the “Diffusion Electrolyte” tab.

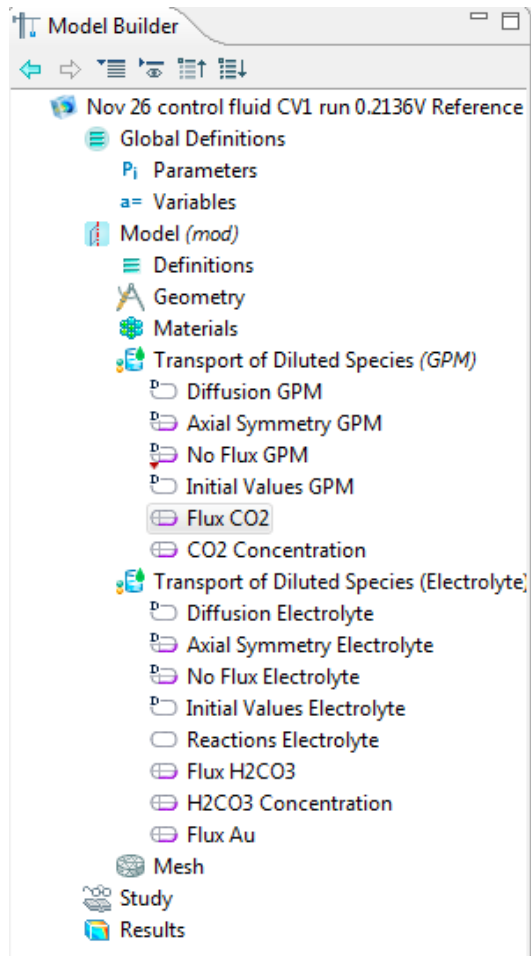


Figure 15: Sub tabs in Transport of Diluted Species modules

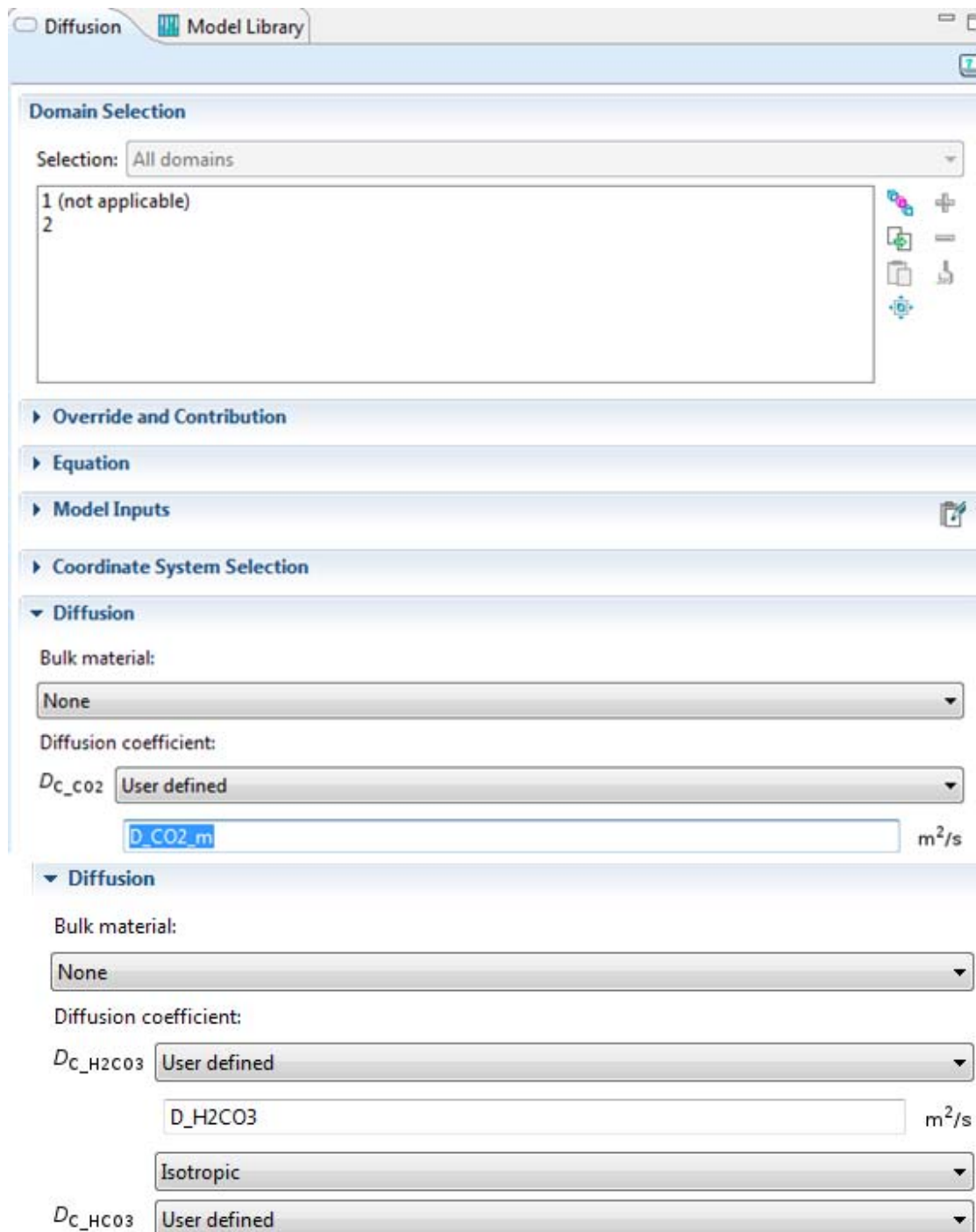


Figure 16: Diffusion coefficients under “Diffusion GPM” and “Diffusion Electrolyte”

In Figure 15, “Axial Symmetry GPM” and “No Flux GPM” are default BCs where the flux is 0 in the middle due to: radial symmetry (i.e., at $r=0$), at the walls (i.e., at $z=0$), and on the sides of the domain ($r=R_2$). Similarly, “Axial Symmetry Electrolyte” and “No Flux Electrolyte” BCs are specified where appropriate according to the BCs shown in Table 4. Initial conditions are included for each species by entering the corresponding initial concentrations under the “Initial Values GPM” tab and “Initial Values Electrolyte” tab in Figure 17.

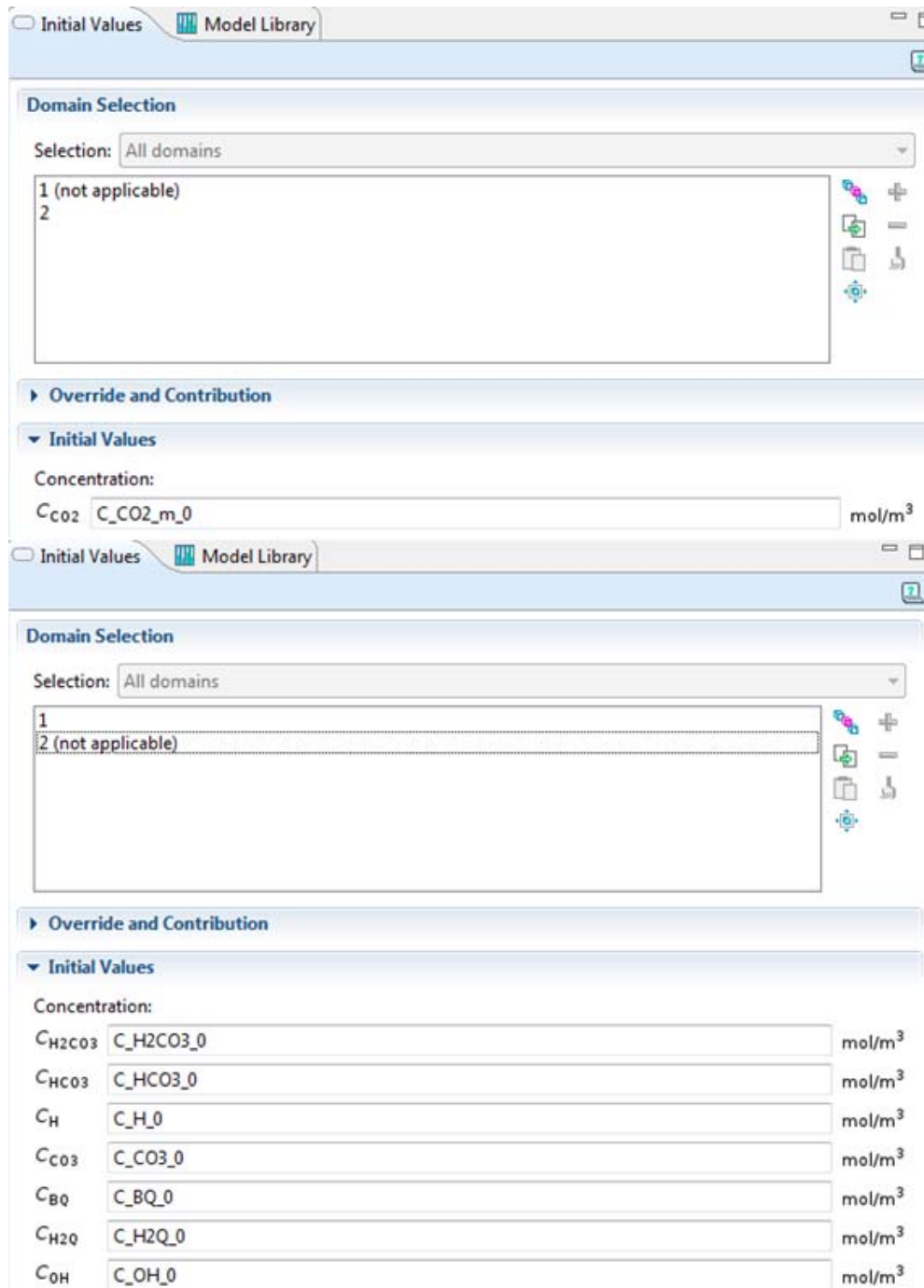


Figure 17: Initial conditions in membrane and electrolyte

Reactions in the electrolyte were specified using the “Reactions Electrolyte” tab shown in Figure 18

Domain Selection

Selection: Electrolyte

1

► Override and Contribution

► Equation

▼ Reactions

R_{C_H2CO3}	<input type="text" value="kr_H2CO3*C_H*C_HCO3-kf_H2CO3*C_H2CO3"/>	mol/(m ³ ·s)
R_{C_HCO3}	<input type="text" value="kf_H2CO3*C_H2CO3-kr_H2CO3*C_H*C_HCO3+kr_HCO3*C_I"/>	mol/(m ³ ·s)
R_{C_H}	<input type="text" value="kf_HCO3*C_HCO3-kr_HCO3*C_H*C_CO3+kf_H2CO3*C_H2C"/>	mol/(m ³ ·s)
R_{C_CO3}	<input type="text" value="kf_HCO3*C_HCO3-kr_HCO3*C_H*C_CO3"/>	mol/(m ³ ·s)
R_{C_BQ}	<input type="text" value="0"/>	mol/(m ³ ·s)
R_{C_H2O}	<input type="text" value="0"/>	mol/(m ³ ·s)
R_{C_OH}	<input type="text" value="kf_H2O*C_H2O_0-kr_H2O*C_H*C_OH"/>	mol/(m ³ ·s)

Figure 18: Reaction tab in electrolyte

Under the “Flux CO₂” and “Flux H₂CO₃” tabs shown in Figure 19, special BCs such as BC (4.2.1) in Table 4 were specified using the *Flux* function where the syntax “ndflux_xx” was used to specify the rate of diffusion of the species. The symbol “+” indicates that H₂CO₃ is entering the electrolyte. The value of GPM.ndflux_C_CO₂ is computed by COMSOLTM using the PDEs.

Boundary Selection

Selection: Interphase between GPM and Electrolyte

4

8

► **Override and Contribution**

► **Equation**

▼ **Inward Flux**

Flux type:

General inward flux

☒ Species C_H2CO3

Inward flux:

$N_{0,C_{H_2CO_3}}$ +GPM.ndflux_C_CO2 mol/(m²·s)

Figure 19: Continuous flux at the interphase between gas-permeable membrane and electrolyte

Under the “CO₂ Concentration” and “H₂CO₃ Concentration” tabs in Figure 20, BCs involving the known concentration at a boundary (such as BCs (4.1.1) and (4.1.4)) were implemented using the “Concentration” function.

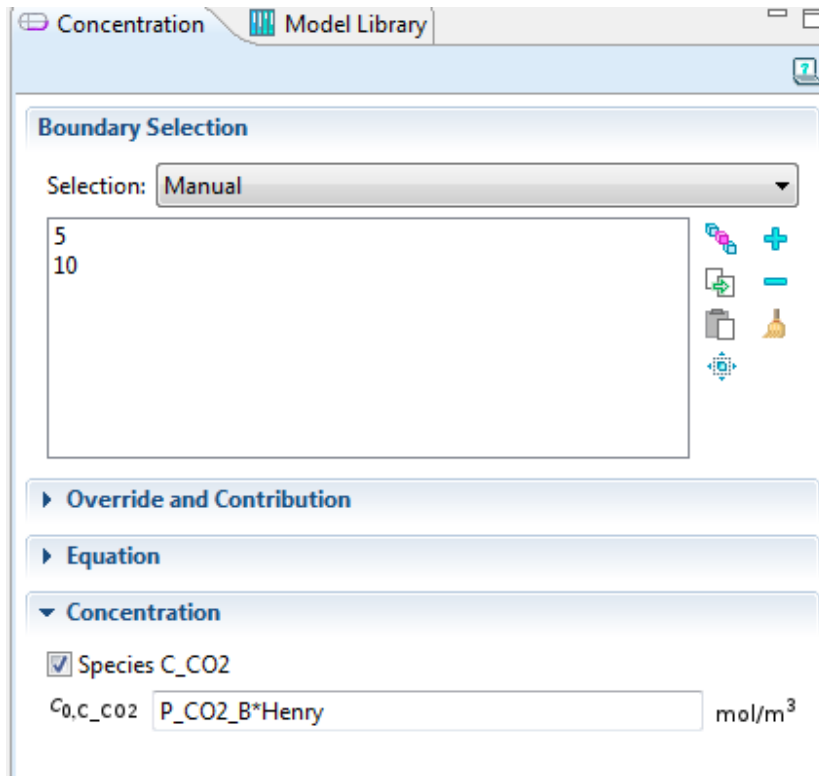


Figure 20: BCs involving the Henry's constant.

BCs involving the partition coefficient between the membrane and the electrolyte (i.e., BCs (4.1.2) and (4.1.5) in Table 4) were implemented as shown in Figure 21. Note that the Concentration tab in Figure 20 was opened from the Transport of Diluted Species (GPM) tab in Figure 15 and that the Concentration tab in Figure 21 was opened from the Transport of Diluted Species (Electrolyte) tab in Figure 15.

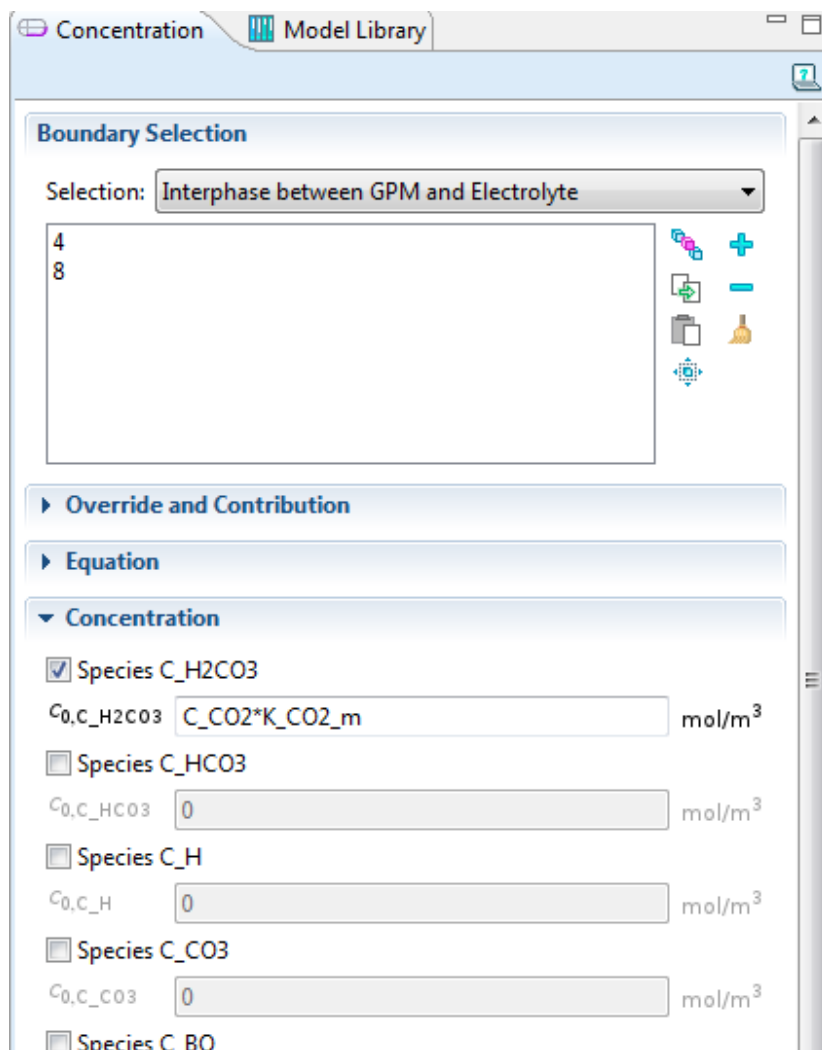


Figure 21: BCs involving the partition coefficient between the membrane and the electrolyte

Equilibrium reaction (7) occurs at the Au electrode. As such, BCs (4.4.3), (4.7.3), and (4.8.3) involving rate constants k_{fAu} and k_{rAu} were implemented using the “Flux Au” tab shown in Figure 22. The corresponding species influenced by these rate constants were specified by checking the corresponding boxes in Figure 22 so that the rate expressions could be entered.

▼ Inward Flux

Flux type:
General inward flux

☐ Species C_H2CO3

☐ Species C_HC03

☒ Species C_H

Inward flux:
 N_{0,C_H} mol/(m²·s)

☐ Species C_CO3

☐ Species C_NaHCO3

☐ Species C_Na

☐ Species C_OH

☒ Species C_BQ

Inward flux:
 N_{0,C_BQ} mol/(m²·s)

☒ Species C_H2Q

Inward flux:
 N_{0,C_H2Q} mol/(m²·s)

Figure 22: Reaction flux at the Au electrode.

Chapter 3 Simulation Results

2.4 Summary

The mathematical model for the POC pCO₂ sensor has been presented in this Chapter.

The fully implemented model consists of the material balance PDEs, algebraic equations

from constitutive relationships such as the Nernst equation, initial and BCs, and the implementation in COMSOLTM, using library modules such as the Transport of Dilute Species, and probes and flux calculations.

The model is fitted in the following chapter, and laboratory test data are used to adjust several key parameters in order to obtain predictions that match observed behavior. The fitted model is then used to conduct a series of sensitivity investigations, in which the impact of key design parameters on predicted sensor response is determined.

3.1 Overview

The mathematical model for the pCO₂ sensor was solved using COMSOLTM, and fitted with a number of datasets obtained from an Abbott Point of Care product testing database. Four sets of data were obtained for POC pCO₂ sensors using the calibrant fluid, and for four different control fluids with observed pCO₂ values, as shown in Table 10 (Abbott Point of Care-d, 2012). The unit mmHg was used due to the fact the data was collected under this unit. It was converted to kPa in COMSOLTM.

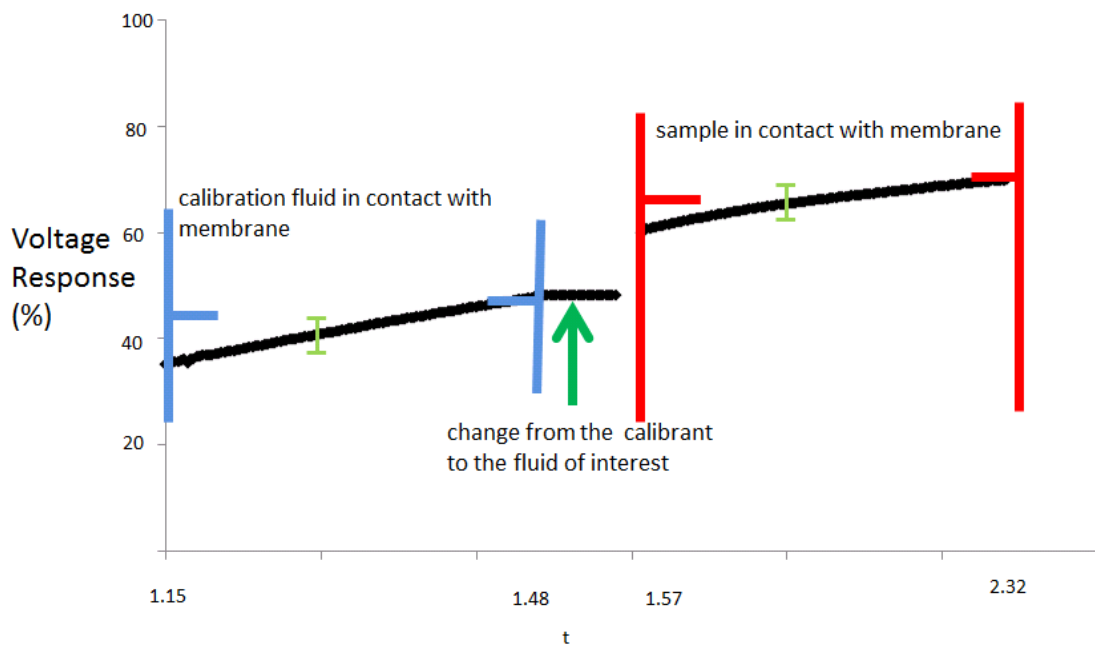
Table 10: pCO₂ Values of Calibrant and Control Fluids.

Calibrant and Control Fluids	Observed pCO ₂ Values (mmHg)
Calibrant fluid	APOC Company Confidential
CV1	89.4
L2	29.3
GB	22.2
CV5	17.8

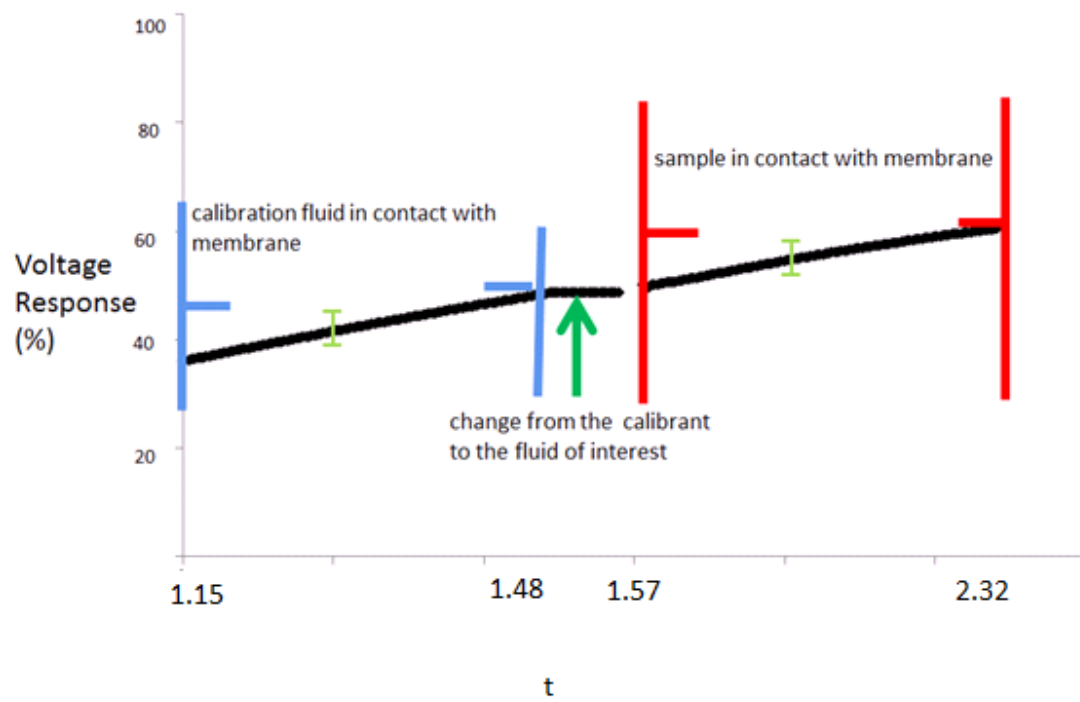
Each run consists of a calibrant/control fluid pair in which the first portion of the run was with a standard calibrant (contained within the test cartridge), followed by a control fluid (entered into the cartridge by an operator). Note that CV1, L2 and CV5 are control fluids (aqueous solutions) and GB (glucose blood) is blood collected from donors infused with a known level of CO₂. This blood is collected by the phlebotomist at Abbott Point of Care and its pCO₂ value is determined offline right before usage. Voltage versus time data was collected for each fluid for four replicate experiments. Representative plots of voltage versus (vs) time for each fluid are plotted in Figure 23 (the time has been normalized for the time axis). Note that the green error bars (corresponding to one

standard deviation of measurement noise) are shown on the (overlapping) symbols to illustrate the reproducibility of the calibrant and control-fluid data (which were all collected in October, 2012). These plots have an approximately linear slope during the time periods when the calibration fluid or a control fluid is in contact with the membrane (Cai and Reimers, 1993).

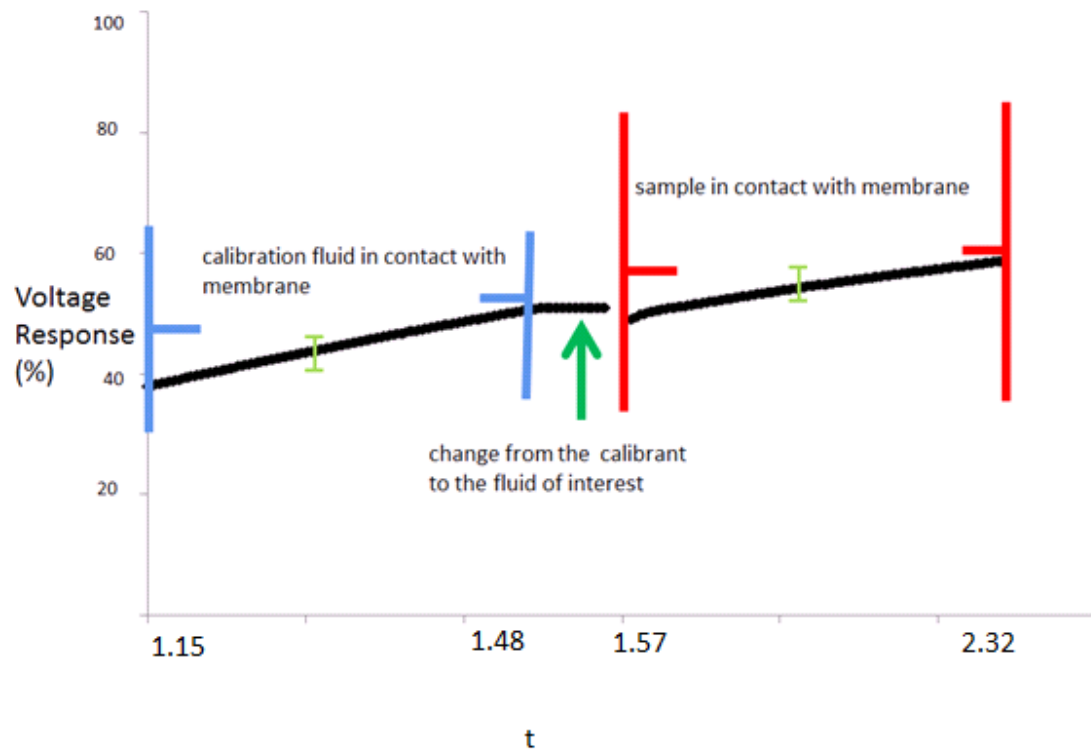
a)



b)



c)



d)

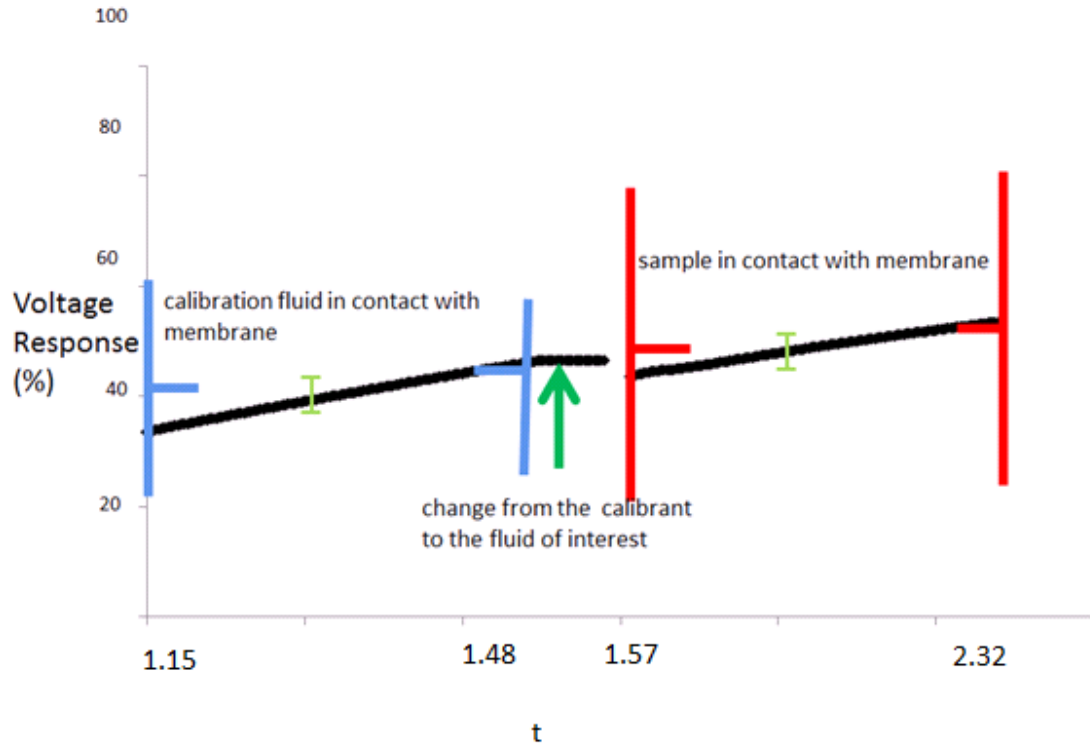


Figure 23: Voltage responses as a function of time for calibrant (from 1.15 to 1.48) and control fluids (from 1.57 to 2.32) for a) CV1, b) L2, c) GB, and d) CV5. Green error bars for measurements are shown at two time points to illustrate reproducibility.

3.2 Simulated Voltage Response Plots for Calibrant

A voltage versus time plot was generated in COMSOLTM using an input $p\text{CO}_2$ value of the calibrant, as specified in Table 2. The results are shown in Figure 24. Note that these simulation results were obtained using the initial conditions and the parameter values in Table 8. Parameter k_{fAu} was adjusted to obtain a good match between the simulation results (in black) and the data values in red. No data were available before $t = t_2$ (see Figure 4 and associated discussion). Note that the manually adjusted value $k_{fAu} = 666.28$

$\frac{m^7}{s \cdot mol^2}$ is the initial parameter value reported in Table 10 because no literature values for

this parameter were available and it was determined using these preliminary simulation results. Simulations with alternative values of k_{fAu} are shown in Figures 25 and 26.

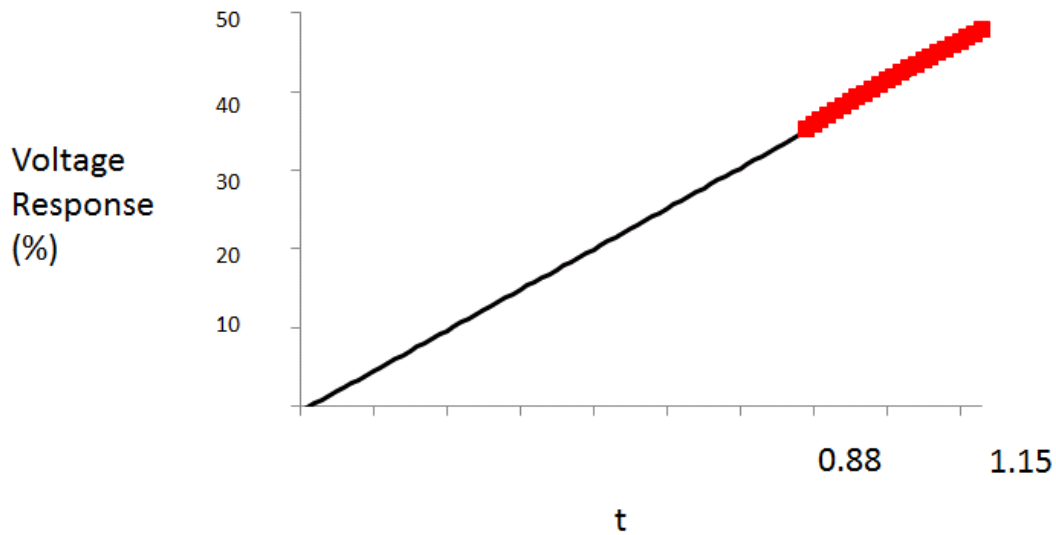


Figure 24: Voltage response for a simulation for calibrant in COMSOL™ with $k_{fAu} = 666.28 \frac{m^7}{s \cdot mol^2}$

Figure 25 is a simulation for a k_{fAu} value of $160 \frac{m^7}{s \cdot mol^2}$ and Figure 26 is a simulation for a k_{fAu} value of $700 \frac{m^7}{s \cdot mol^2}$. k_{fAu} changes the slope of the voltage versus time plot, with higher k_{fAu} values yielding steeper slopes. Note that when k_{fAu} is adjusted, the reverse rate constant k_{rAu} is automatically recalculated via the equilibrium constant, so that Equation (28) is satisfied. Figures 25 and 26 confirm that the value of $k_{fAu} = 666.28 \frac{m^7}{s \cdot mol^2}$ provides the best fit.

Figure 27 shows the initial voltage response of all control fluids, revealing a mismatch between the simulated results and the data, indicating that one or more parameters need to be adjusted to obtain a good fit to the data. Unfortunately, the version of COMSOL™

that was used did not have any parameter estimation capabilities or a Matlab Livelink so that Matlab could be used to estimate the parameters. Rather than conducting a formal nonlinear least-squares parameter estimation, a few key parameters were identified and adjusted manually to improve the fit to the data. Abbott Point of Care uses a mean-based algorithm that calculates the average voltage response between a predetermined number of seconds (APOC Company Confidential) for the control fluid run. This average voltage response value corresponds to the pCO₂ in each of the control fluids. This value can be compared to the known pCO₂ value (calibrant) in order to generate a quantitative result.

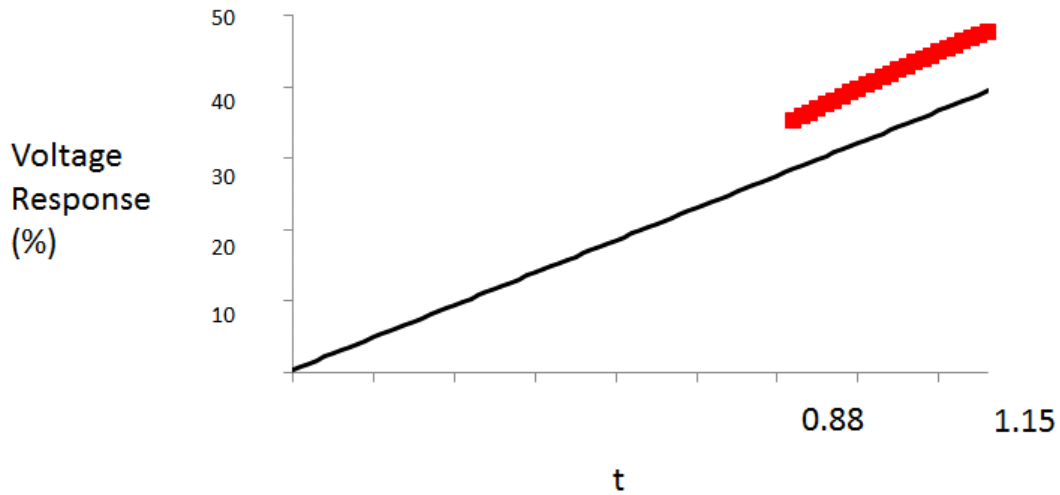


Figure 25: Voltage response for a simulation with $k_{fAu} = 160 \frac{m^7}{s \cdot mol^2}$

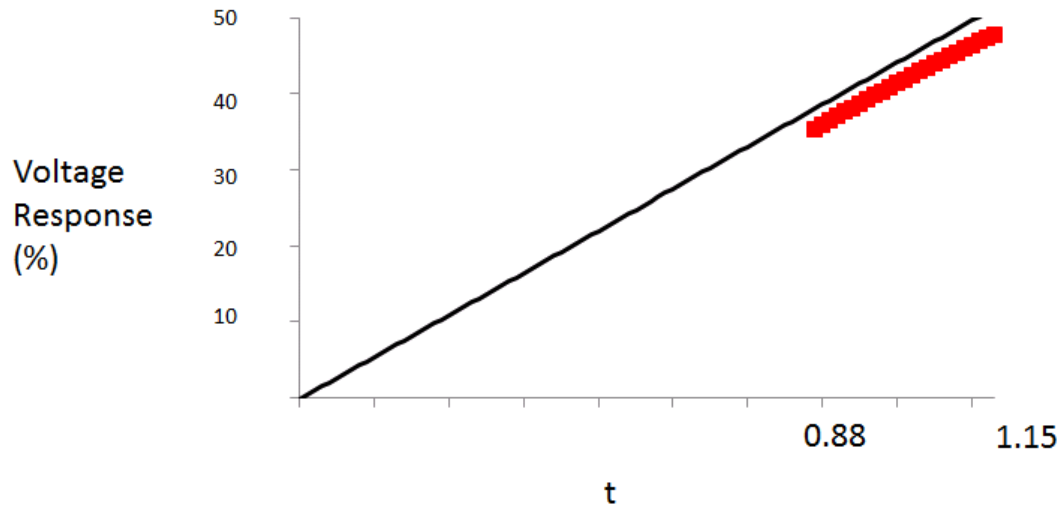


Figure 26: Voltage response for a simulation with $k_{fAu} = 700 \frac{m^7}{s \cdot mol^2}$

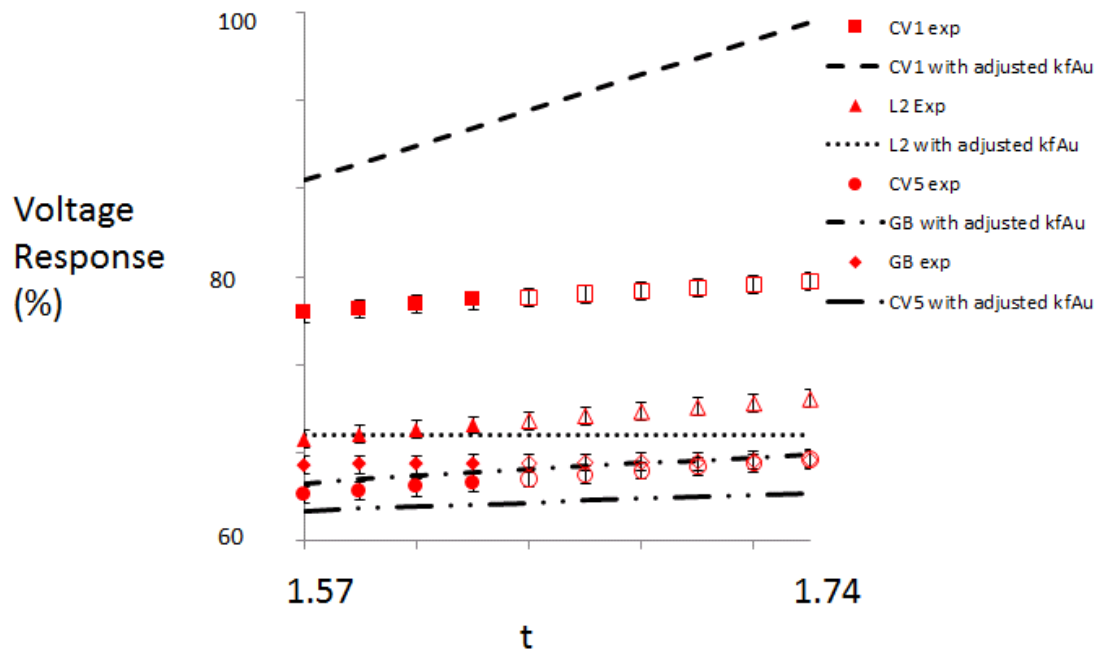


Figure 27: Voltage response for all control fluids. The red marks are data points from experiments. The solid red marks are the initial predetermined number of seconds that are used to calculate the mean voltage response.

3.3 Identifying the Two Most Influential Parameters

The 11 parameters that could be considered for estimation are: $k_{f_{Au}}$, $K_{H_2CO_3}$, K_{HCO_3} , K_{H_2O} , κ_{CO_2m} , H , D_{CO_2m} , $D_{H_2CO_3}$, D_{H^+} , D_{Na^+} , and D_{BQ} . An estimability ranking procedure was used to determine that parameters $k_{f_{Au}}$ and K_{CO_2m} are the most influential (relative to their uncertainties) (Thompson et al., 2009; McLean and McAuley, 2012). The estimability analysis is conducted using first-order sensitivity information (first derivative information) that describes the impact of perturbations of parameters on the predicted responses, with all other parameters held constant at nominal values. This sensitivity information can be generated analytically if algebraic models are available. In this instance, because the model consisted of PDE and algebraic equations requiring numerical solution using COMSOLTM, a finite-difference perturbation approach was used to determine the first-order sensitivity information. Each of the 11 parameters was perturbed one at a time (by 10% of their nominal values), and the solution trajectories were computed using COMSOLTM. The response being considered was the average voltage at the surface of the Au electrode for a predetermined number of seconds (APOC Company Confidential). This response was considered because of the algorithm used in Abbott Point of Care. A mean-based algorithm is employed in the pCO₂ sensor design. In order to apply the estimability algorithm of McAuley and co-workers, the scaled sensitivity matrix corresponding to the runs being considered has to be formed. In this instance, the sensitivities were considered over the four control fluid runs identified earlier (CV1, L2, GB and CV5), which makes 4 rows in the scaled sensitivity matrix. Since there are 11 parameters, the sensitivity matrix is a 4 X 11 matrix whose elements are:

$$\frac{\Delta \bar{V}_j}{\Delta \theta_i} \frac{s_{\theta_i}}{s_{y_j}}$$

where $\Delta \bar{V}_j$ is the resulting change in predicted average voltage (for fluid j) when parameter θ_i is adjusted by $\Delta \theta_i$. s_{θ_i} is the uncertainty in the initial value of the i^{th} parameter, which is calculated as half the distance between the lower and upper bound for the parameter (see Table 2). s_{y_j} is the uncertainty in the measured average voltage, which was assumed to be the same for all four fluids. This value $s_{y_j} = 2.48$ mV was determined using the pooled standard deviation of the average voltage responses from five sets of dynamic experiments for each control fluid. The elements of the resulting scaled sensitivity matrix (to two decimal places of accuracy) are shown in Table 11. These elements are dimensionless due to the scaling that was used.

The estimability algorithm of McAuley and co-workers determines the most influential parameters, after taking into account the co-dependencies in the impact of parameters on the predicted response. This is accomplished using an orthogonalization algorithm (Thompson et al., 2009; McLean and McAuley, 2012). The algorithm determined that parameters k_{fAu} and κ_{CO2m} are the most influential parameters. This result is not surprising because of the relatively large magnitudes of the scaled sensitivity entries in columns 1 and 5 in Table 11 compared to the entries in columns corresponding to the other parameters.

Table 11: Scaled Sensitivity Matrix for Parameter Ranking

Fluids	k_{fAu}	$K_{H_2CO_3}$	K_{HCO_3}	K_{H_2O}	κ_{CO_2m}	H	D_{CO_2m}	$D_{H_2CO_3}$	D_{H^+}	D_{Na^+}	D_{BQ}
CV1	70.86	0.01	0.00	0.00	20.69	0.00	-0.02	-0.03	0.00	0.00	-1.53
L2	9.70	0.01	0.00	0.00	2.82	0.09	0.00	0.00	0.00	0.00	-0.11
GB	10.05	0.01	0.00	0.00	3.44	0.11	0.00	0.00	0.00	0.00	-0.08
CV5	5.45	0.01	0.00	0.00	1.59	0.05	0.00	0.00	0.00	0.00	-0.03

The two most estimable parameters were hand tuned in order to improve the predictions of the average voltage response. Adjustments were introduced, and COMSOLTM was used to generate new trajectories from which average voltage response values were determined. The resulting “best” values of the two most influential parameters were $k_{f_{Au}} = 66.6 \frac{m^7}{s \cdot mol^2}$ and $\kappa_{CO_{2m}} = 1.2$. Predictions using the tuned parameter values are shown in Figures 28 and 29. A good match with the data was obtained over the predetermined number of seconds (solid symbols). However, the simulated data did not fit the data as well after the predetermined number of seconds (open symbols) for the L2 and CV5 runs. The experimental data for L2 has a steeper slope compared to the rest of the control fluids. Note that a better fit to the data might be obtained using least-squares parameter estimation instead of empirical hand-tuning.

In order to have a better understanding of the underlying phenomena in the sensor, a number of “sectioning” plots were generated to study concentration profiles along the vertical and radial axes. The resulting plots are summarized for a number of key species.

Concentration profiles for carbonic acid within the calibration fluid were simulated at several different times in Figure 30 using the tuned parameter values and conditions that correspond to the run shown in Figure 31. These vertical profiles were determined at the midpoint of the Au electrode annulus ($r = 1.265 \times 10^{-4} \text{ m}$), as shown in Figure 32. Note that because there is no angular variation, this profile would be the same anywhere along the midpoint radius on the Au electrode annulus. At time zero, the concentration profile is flat and corresponds to the initial concentration indicated in Assumption 1.2 in Table 1. When the calibration fluid comes in contact with the membrane, CO₂ begins to diffuse

through the membrane and to dissolve as H_2CO_3 . After 0.1 ms, the additional H_2CO_3 has penetrated about 1.4 μm into the electrolyte and by 100 ms, the vertical concentration profile is uniform. These simulation results suggest that the dynamics of the diffusion within these small POC sensors are very fast compared to the dynamics in larger Severinghaus sensors described in the introduction. Furthermore, these results suggest that stable voltage readings could be obtained in an even shorter period of time than is used in the current sensor. The main impediment to achieving a fast response may be heating of the sensor (i.e., the sensor can be heated faster to 37 °C so the voltage response reading can be generated sooner) rather than diffusion of CO_2 .

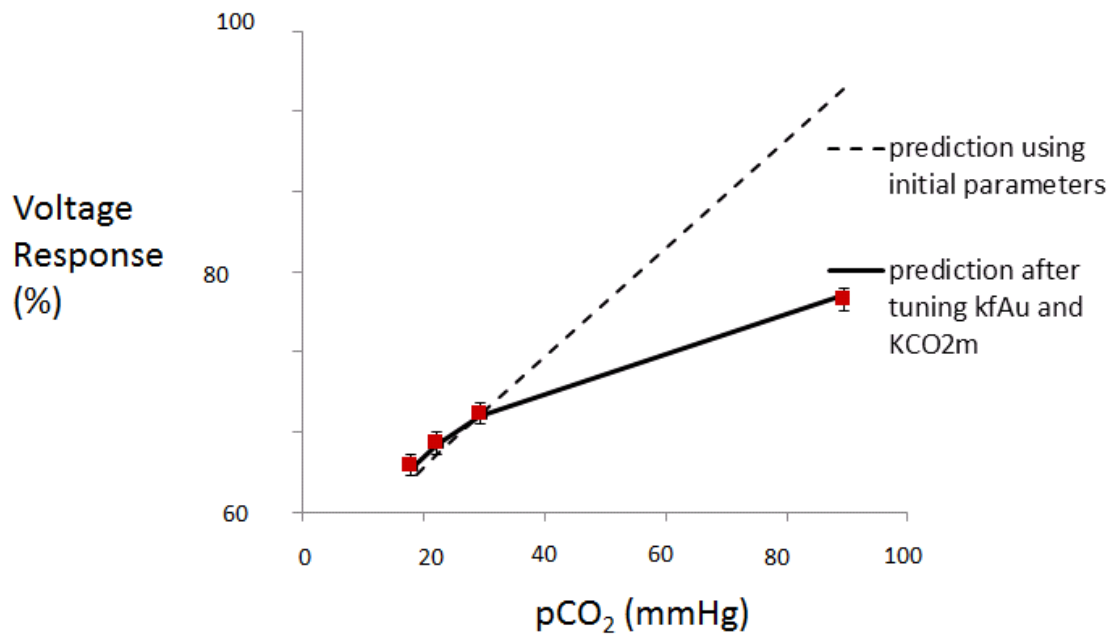


Figure 28: Mean voltage response vs pCO₂ plots for the base and tuned cases

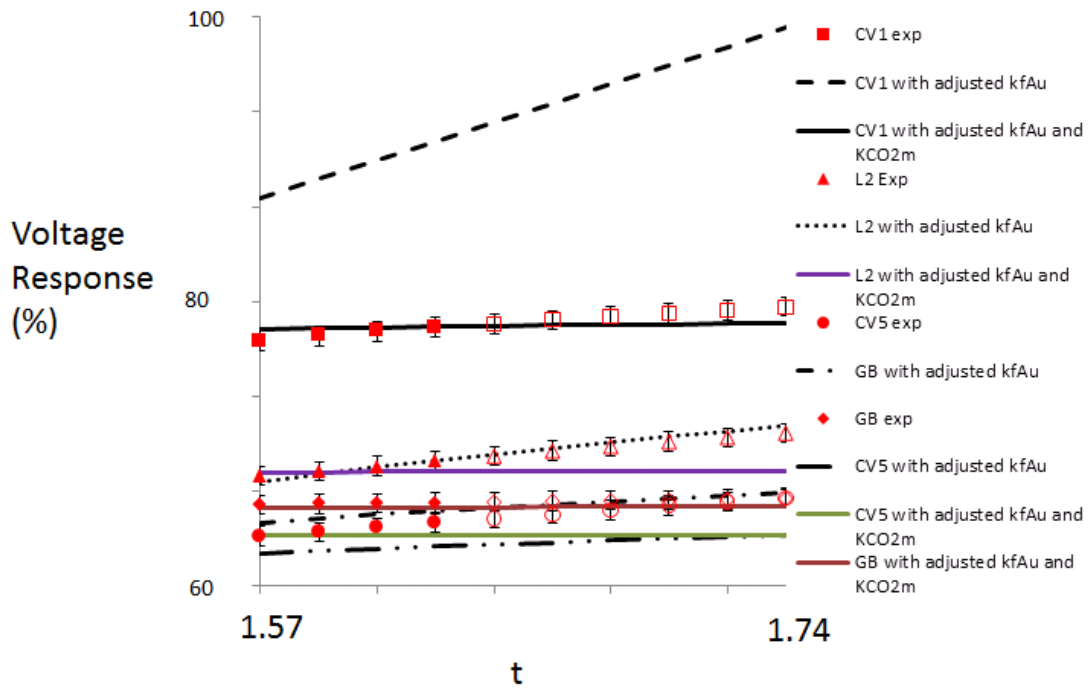


Figure 29: Voltage response for all control fluids for using initial parameter values in Table 8 are represented by dashed lines and voltage response using tuned parameter values are represented by solid lines.

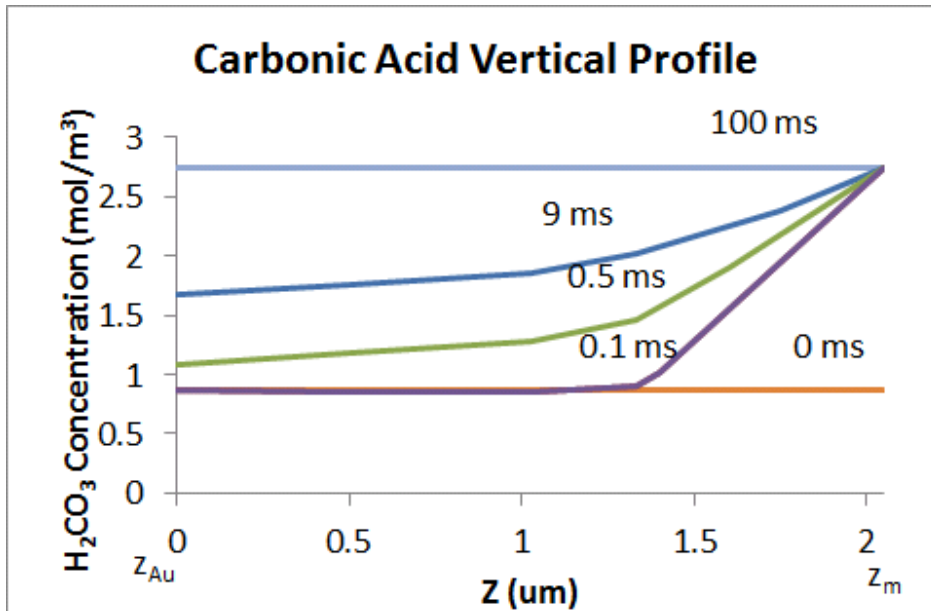


Figure 30: Concentration profiles for carbonic acid at the middle of the Au surface.

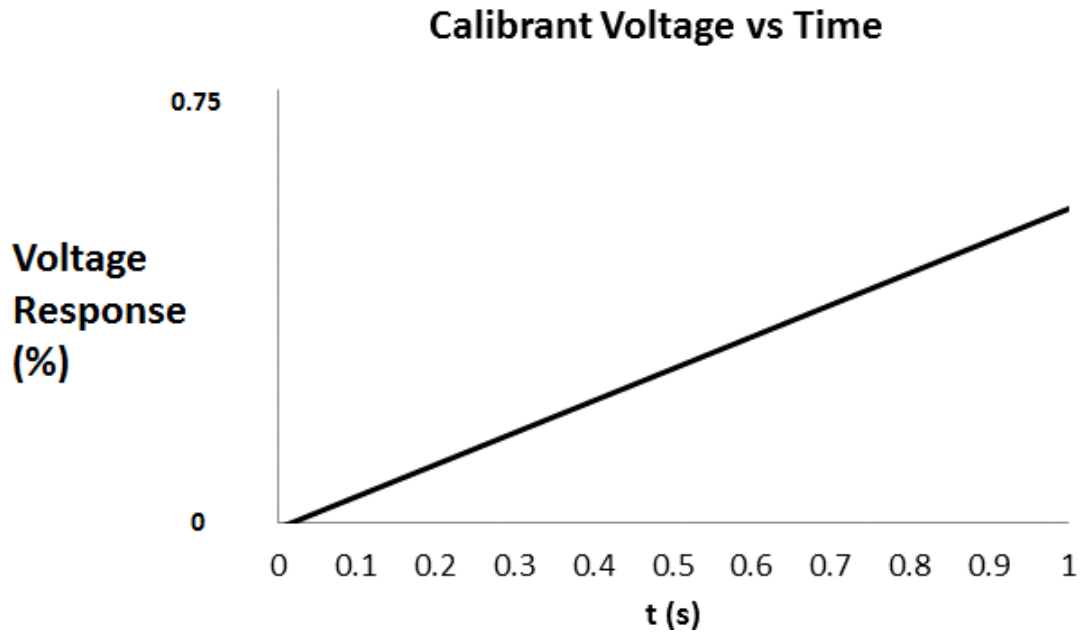


Figure 31: Voltage response for calibrant used for concentration profiles at centre of the Au electrode

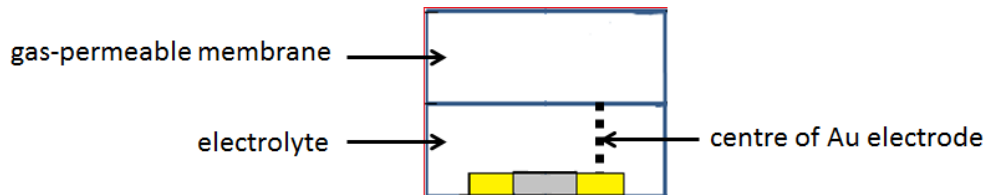


Figure 32: Centre of Au electrode where carbonic acid concentration profiles are taken

3.4 Sensitivity Analysis

Part of the value of a mathematical model of the POC sensor response is the ability to study the impact of design decisions on the performance of the sensor. In part as proof of concept, and as a preliminary step in using the model to elucidate the impact of design decisions on sensor behavior, a number of design parameters in the sensor were varied to observe their influence on the voltage response. Sensitivity analyses were performed to determine the most sensitive design parameters in the sensor, over the ranges of practical interest. The factors that were studied are: water concentration in the electrolyte, height

of the electrolyte within the sensor (because this will vary depending on the water that has evaporated), initial dissolved CO₂, initial buffer concentration and initial BQ in the electrolyte composition. Note that with a fixed cross-sectional area, varying the height of electrolyte is equivalent to varying the volume of electrolyte in the sensor. The corresponding sensitivity plots are shown in Figures 33 to 46. Note that only the results for CV1 and CV5 are shown. These fluids have the highest and lowest pCO₂ values, respectively, of the four control fluids, and were used to bracket the range of pCO₂ values that would typically be encountered.

Figure 33 depicts the voltage response for the calibrant when different amounts of water are present in the electrolyte, while the height and hence volume of the electrolyte is held at its nominal design value. The voltage increases by 40% at 0.88 when more water is present. Similarly, the voltage decreases by 35% at the same time when less water is present. Figure 34 presents the voltage response for the control fluids under the same scenario. The predicted voltage is significantly higher for both CV1 and CV5 when there is more water in the electrolyte. Similarly, the voltage is lower when there is less water in the electrolyte. These results make sense because the initial concentration of H₂Q at the electrode surface is lower while the initial concentration of H⁺ is higher when there is more water. Both BQ and H₂Q concentrations are reduced when there is more water. However, the H⁺ concentration is increased when there is less water due to Equations (32) and (33) and equilibriums (17) to (19). The concentrations of H₂Q and H⁺ dominate the voltage response in Equation 7. When there is a lower concentration of H₂Q and a higher concentration of H⁺, the magnitude of $\frac{RT}{nF} \ln \left(\frac{[H_2Q]}{[BQ][H^+]^2} \right)$ decreases, which increases the value of $E_{BQ \text{ to } H_2Q}$ due to the subtraction of a lower value of $\frac{RT}{nF} \ln \left(\frac{[H_2Q]}{[BQ][H^+]^2} \right)$ in

Equation (7). A higher value of $E_{BQ \text{ to } H_2Q}$ leads to a higher value of E at the Au electrode due to Equation (8) since E_{ref} is constant. Also, when there is more H^+ present at the Au electrode surface, the cations attract more electrons in the Au electrode surface, increasing the accumulated charge separation and yielding a more positive voltage response.

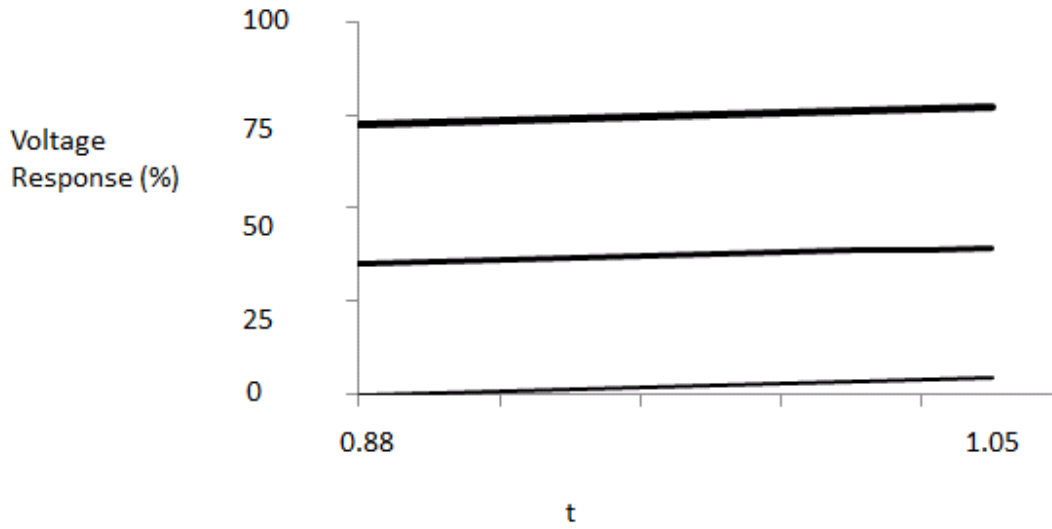


Figure 33: Influence of water concentration in electrolyte voltage response for the calibrant. The thickest lines are for the case with the most water (3/4 of the amount in as-manufactured electrolyte). The medium thickness lines are for the base case (1/2 of the amount in as-manufactured electrolyte) and the thinnest lines are for the case with the least water (1/4 of the amount in as-manufactured electrolyte).

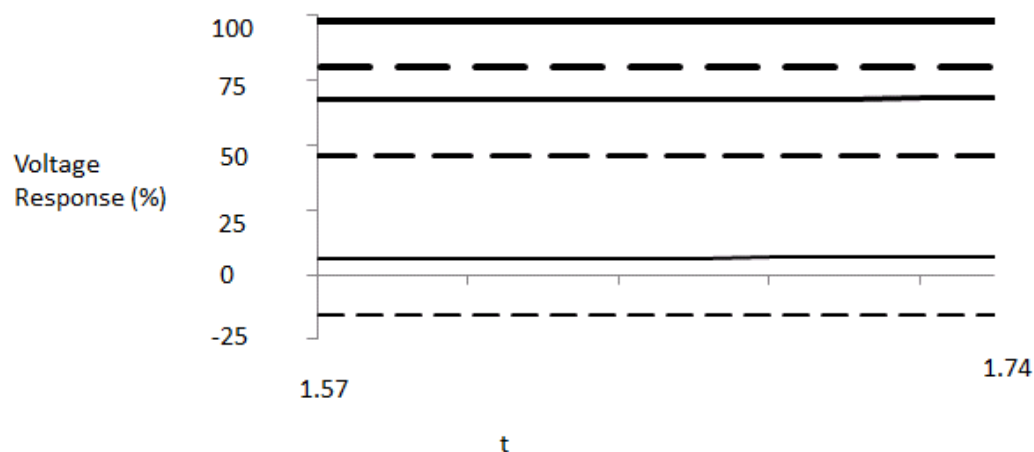


Figure 34: Influence of water concentration in electrolyte on voltage responses are shown for CV1 — , and CV5 - - - . The thickest lines are for the case with the most water (3/4 of the amount in as-manufactured electrolyte). The medium thickness lines are for the base case (1/2 of the amount in as-manufactured electrolyte) and the thinnest lines are for the case with the least water (1/4 of the amount in as-manufactured electrolyte).

Figures 35 and 36 depict the voltage responses when the height of the electrolyte changes. There is no noticeable change in the voltage response for both the calibrant and control fluids. A thicker or thinner electrolyte does not appear to affect the voltage response. The diffusion coefficients of all species are fast compared to the thickness of the membrane. Therefore, the membrane has to be extremely thick (i.e., in the millimeter range) or extremely thin (i.e., in the nanometer range) in order to make a difference. Having an extremely thick membrane drives up the cost. Therefore it is undesirable. Having an extremely thin membrane is likely to prove challenging for consistent and robust manufacturing efforts.

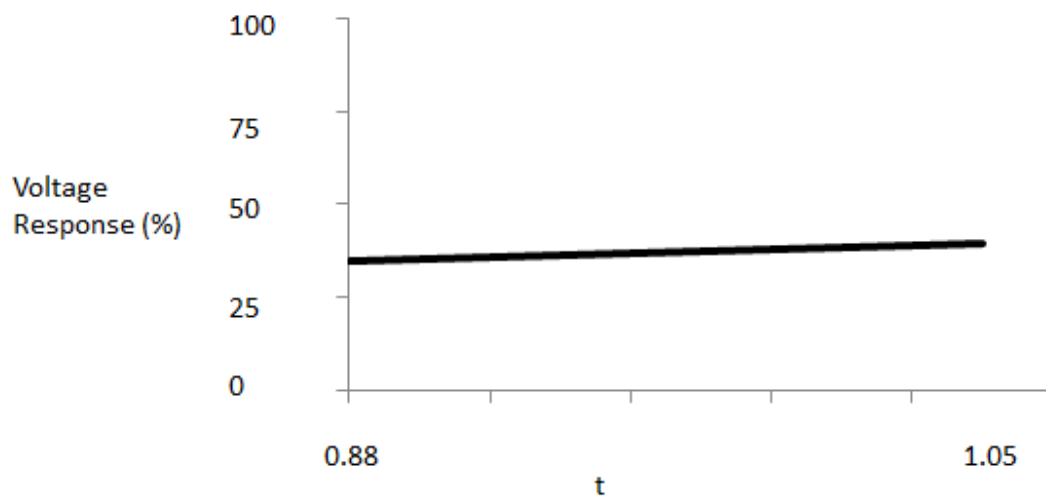


Figure 35: Influence of the electrolyte height on voltage response for the calibrant. The thickest lines are for the case with the most water (3/4 of the amount in as-manufactured electrolyte). The medium thickness lines are for the base case (1/2 of the amount in as-manufactured electrolyte) and the thinnest lines are for the case with the least water (1/4 of the amount in as-manufactured electrolyte).

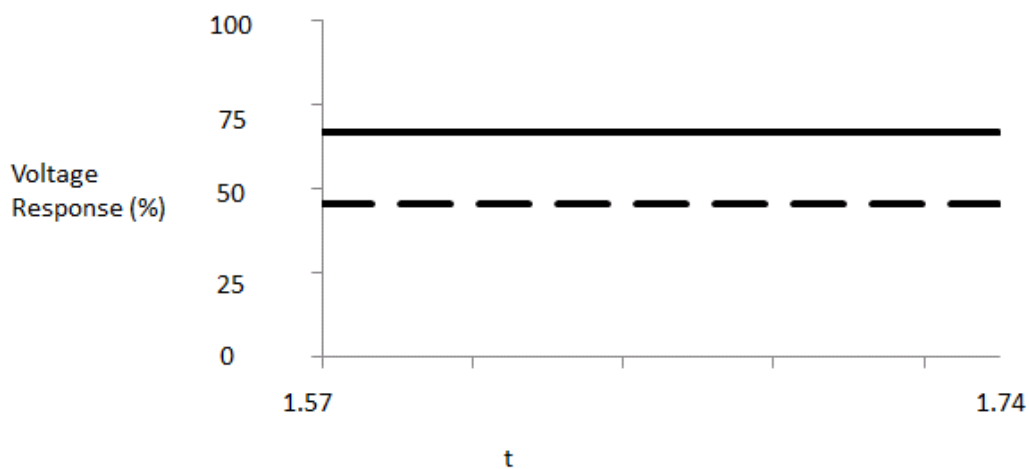


Figure 36: Influence of water concentration in electrolyte on voltage responses are shown for CV1 —, and CV5 - - -. The thickest lines are for the case with the most water (3/4 of the amount in as-manufactured electrolyte). The medium thickness lines are for the base case (1/2 of the amount in as-manufactured electrolyte) and the thinnest lines are for the case with the least water (1/4 of the amount in as-manufactured electrolyte).

Figure 37 illustrates the voltage response for the calibrant when the amount of water and height of the electrolyte are changed together. This produces the same results as those shown in Figure 33, since the height of the electrolyte has no effect on the voltage response as shown in Figures 35 and 36. Consequently, the voltage response for the control fluids shown in Figure 38 is the same as for the case of changes in the amount of water, shown in Figure 34. Therefore, only the amount of water present in the electrolyte affects the voltage response, regardless of the electrolyte geometry.

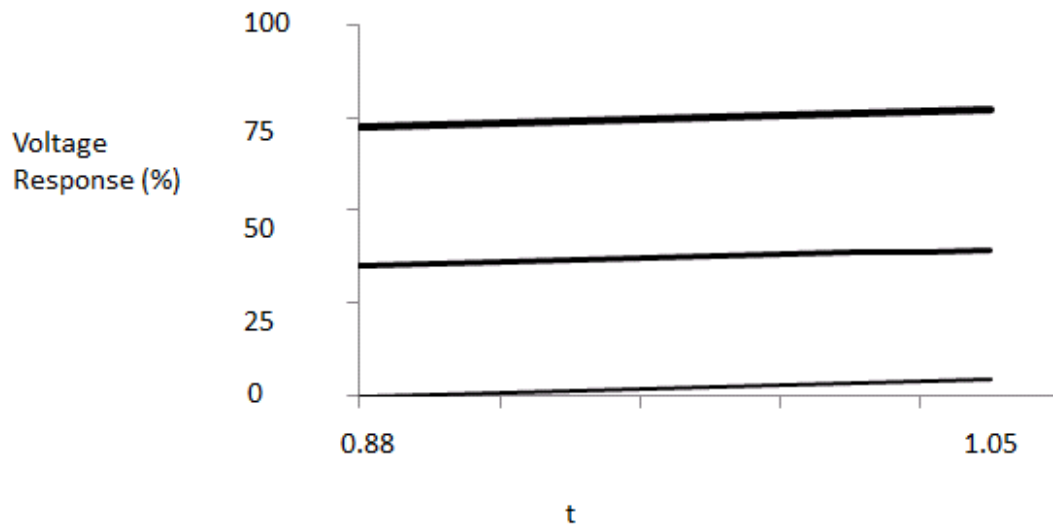


Figure 37: Influence of water concentration in electrolyte and electrolyte thickness on voltage response for the calibrant. The thickest lines are for the case with the most water and thickest electrolyte (3/4 of the water amount and 1.5X the thickness in as-manufactured electrolyte). The medium thickness lines are for the base case (1/2 of the amount and original thickness in as-manufactured electrolyte) and the thinnest lines are for the case with the least water (1/4 of the water amount and 1/2X the thickness in as-manufactured electrolyte).

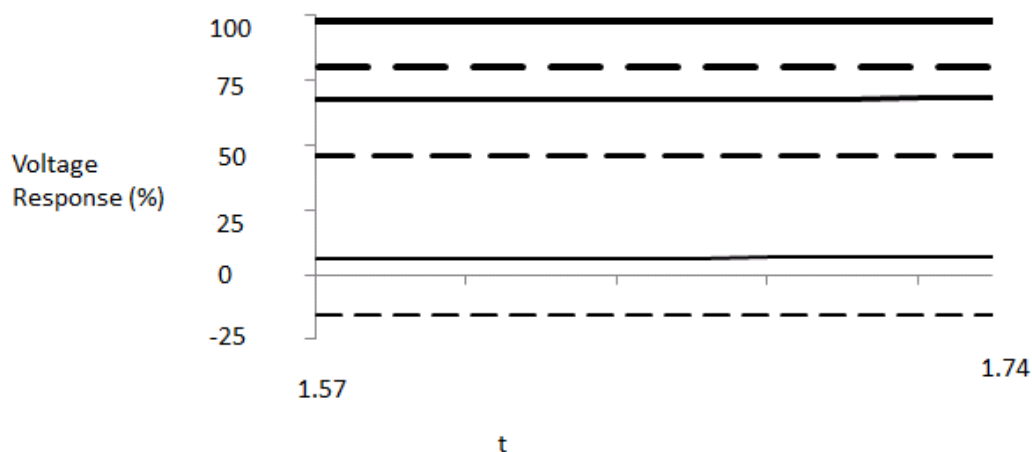


Figure 38: Influence of water concentration in electrolyte on voltage responses are shown for CV1 —, and CV5 - - -. The thickest lines are for the case with the most water and thickest electrolyte (3/4 of the water amount and 1.5X the thickness in as-manufactured electrolyte). The medium thickness lines are for the base case (1/2 of the water amount and original thickness in as-manufactured electrolyte) and the thinnest lines are for the case with the least water (1/4 of the water amount and half of the thickness in as-manufactured electrolyte).

The voltage response for the calibrant when different levels of carbonic acid are present in the electrolyte is shown in Figure 39. The sensor voltage response is increased by 5% relative to the nominal design when there is more carbonic acid present. Similarly, the sensor voltage response is lower relative to the nominal design when there is less carbonic acid. Figure 40 contains the voltage response for the control fluids when different levels of carbonic acid are present in the electrolyte. The sensor voltage response is increased by ~5% for both CV1 and CV5 when there is more carbonic acid present. Similarly, the sensor voltage decreases by about ~5% for both control fluids when there is less carbonic acid. This makes sense physically, since at higher levels of carbonic acid, there is more H^+ present at the Au electrode surface which attracts more

electrons in the Au electrode surface, increasing the accumulated charge separation and yielding a more positive voltage response.

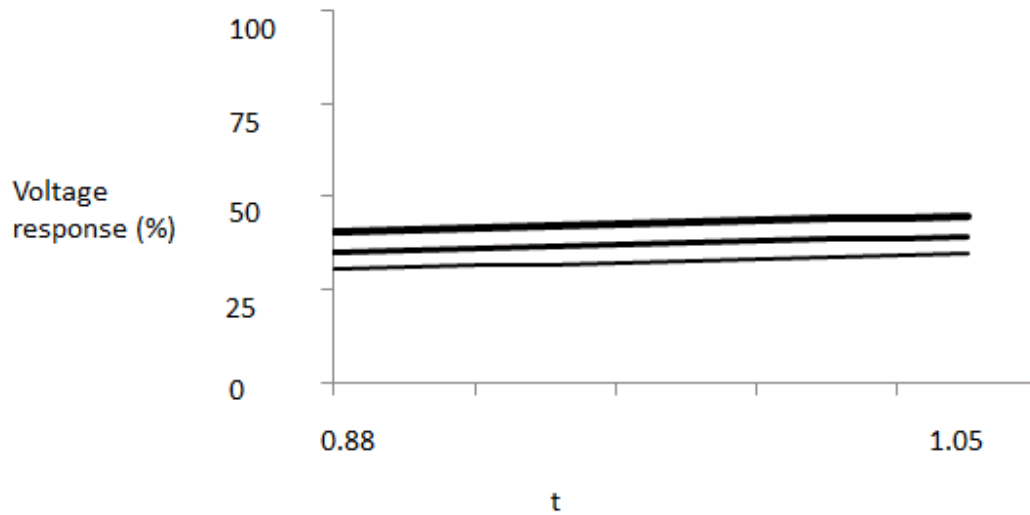


Figure 39: Influence of initial carbonic acid concentration in electrolyte on voltage response for the calibrant. The thickest lines are for the case with the most carbonic (twice of the amount in as-manufactured electrolyte). The medium thickness lines are for the base case (the amount in as-manufactured electrolyte) and the thinnest lines are for the case with the least carbonic acid (half of the amount in as-manufactured electrolyte).

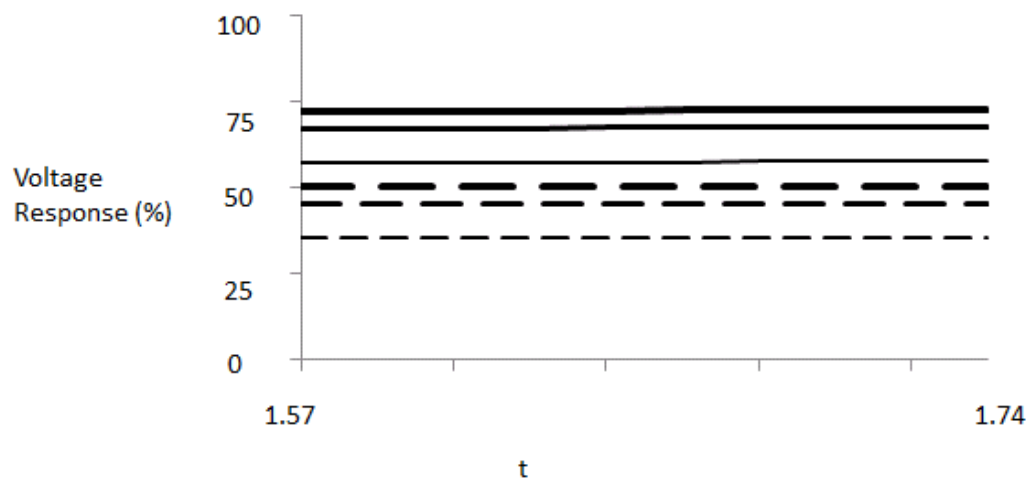


Figure 40: Influence of initial carbonic acid concentration in electrolyte on voltage responses are shown for CV1—, and CV5 - - -. The thickest lines are for the case with the most carbonic (twice of the amount in as-manufactured electrolyte). The medium thickness lines are for the base case (the amount in as-manufactured electrolyte) and the thinnest lines are for the case with the least carbonic acid (half of the amount in as-manufactured electrolyte).

The voltage response for the calibrant when different levels of the buffer are present in the electrolyte solution is shown in Figure 41. The voltage response is increased by ~25% relative to the nominal design when the amount of buffer is doubled, and it is reduced by about ~25% when the amount buffer is halved. The corresponding voltage profiles for the control fluids are shown in Figure 42, at different levels of the buffer present in the electrolyte solution. The voltage response increases by ~10% when the amount of buffer is doubled, and the voltage response decreases by ~10% when the amount is halved for CV1. Similarly, the voltage response increases by ~10% when the amount of buffer is doubled, and the voltage response decreases by ~10% when the amount is halved for CV5. This makes sense physically, since when more buffer is present, there is less H_2Q per volume initially present at the Au electrode surface which yields a higher voltage response. This agrees with Figures 33 and 34.

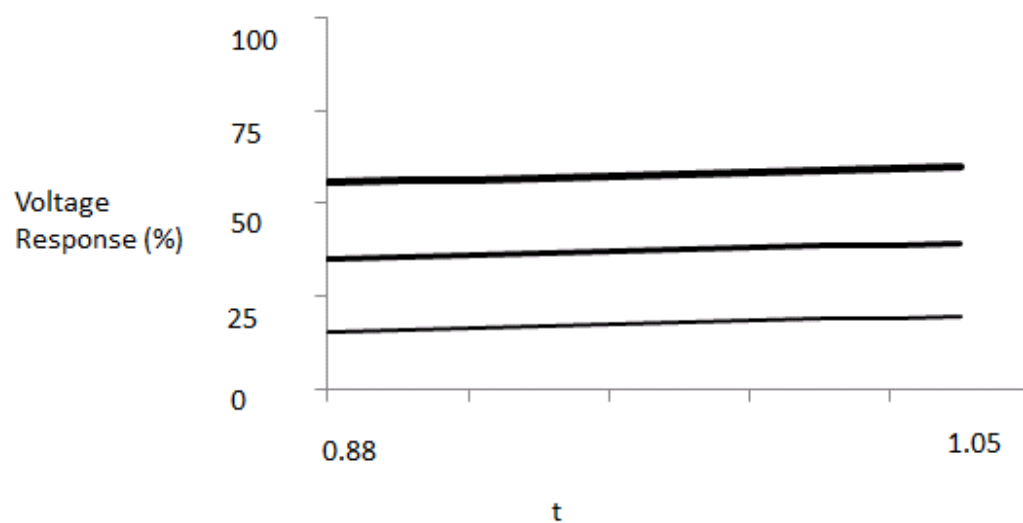


Figure 41: Influence of initial buffer concentration in electrolyte on voltage response for the calibrant. The thickest lines are for the case with the most buffer (four times of the amount in as-manufactured electrolyte). The medium thickness lines are for the base case (twice of the amount in as-manufactured electrolyte) and the thinnest lines are for the case with the least buffer (the amount in as-manufactured electrolyte).

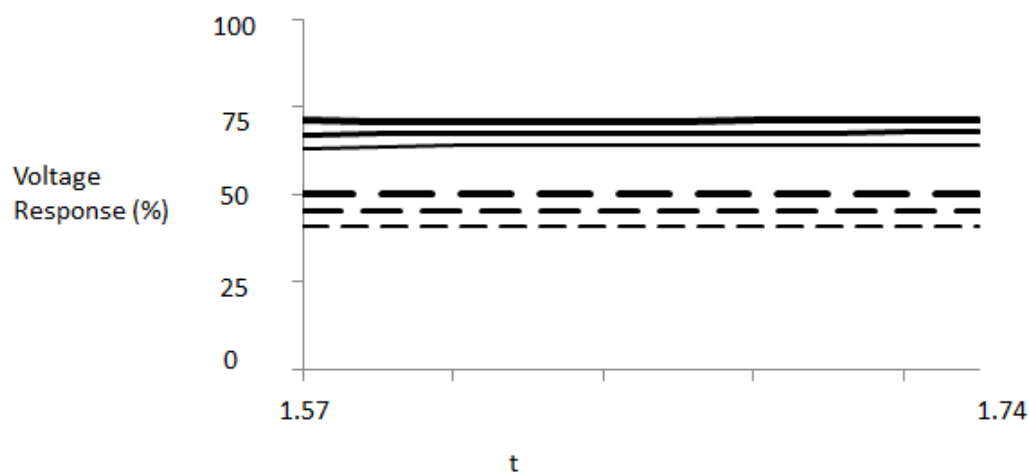


Figure 42: Influence of initial buffer concentration in electrolyte on voltage responses are shown for CV1 —, and CV5 - - -. The thickest lines are for the case with the most buffer (four times of the amount in as-manufactured electrolyte). The medium thickness lines are for the base case (twice of the amount in as-manufactured electrolyte) and the thinnest lines are for the case with the least buffer (the amount in as-manufactured electrolyte).

Changes in the amount of BQ present while maintaining the other species concentrations at their nominal design values produce no change in the voltage response for the calibrant, or for the control fluids. The initial concentration ratio of H2Q to BQ is still the same. Therefore there is no change in the voltage. The voltage responses for the calibrant are shown in Figure 43, while those for the control fluids are shown in Figure 44. Finally, changing the area of the Au electrode surface does not affect the voltage

response for either the calibrant or control fluids, as shown in Figures 45 and 46.

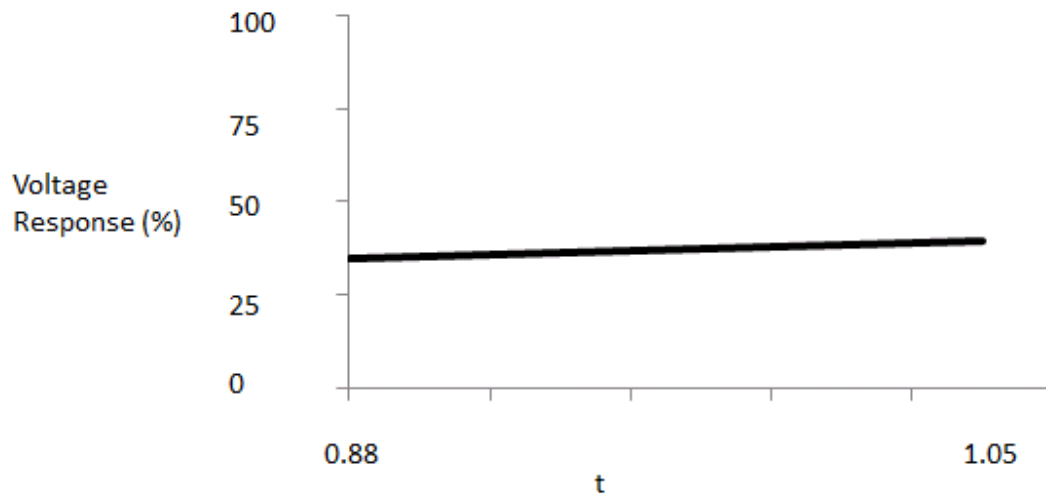


Figure 43: Influence of initial BQ concentration in electrolyte on voltage response for the calibrant. The thickest lines are for the case with the most BQ (four times of the amount in as-manufactured electrolyte). The medium thickness lines are for the base case (two times of the amount in as-manufactured electrolyte) and the thinnest lines are for the case with the least BQ (the amount in as-manufactured electrolyte).

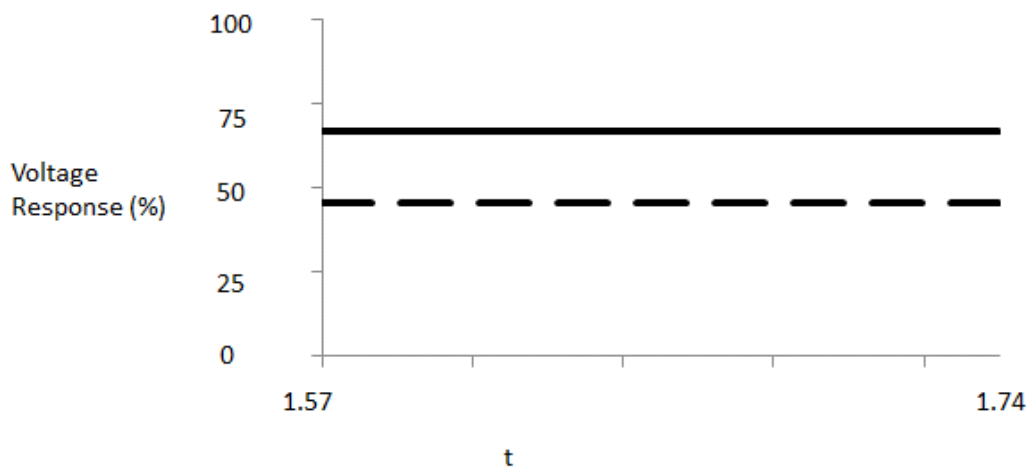


Figure 44: Influence of initial BQ concentration in electrolyte on voltage responses are shown for CV1 —, and CV5 - - -. The thicker lines are for the case with the most water (amount in as-manufactured electrolyte). The regular thickness lines are for the base case (twice of the amount in as-manufactured electrolyte).

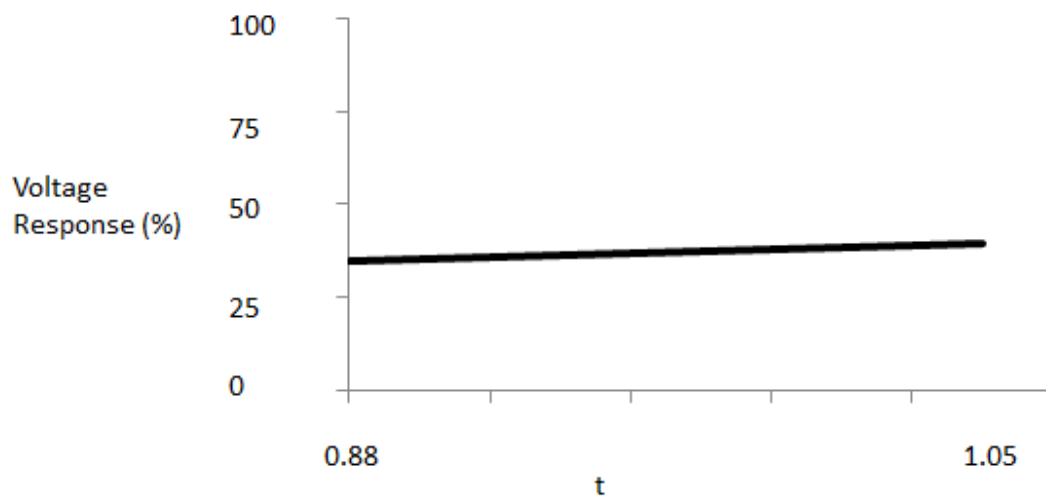


Figure 45: Influence of Au electrode surface area voltage response for the calibrant. The thickest lines are for the case with the biggest Au electrode area (twice of the surface area in as-manufactured Au electrode). The medium thickness lines are for the base case (the surface in as-manufactured Au electrode) and the thinnest lines are for the case with the least water (half of the surface area in as-manufactured Au electrode).

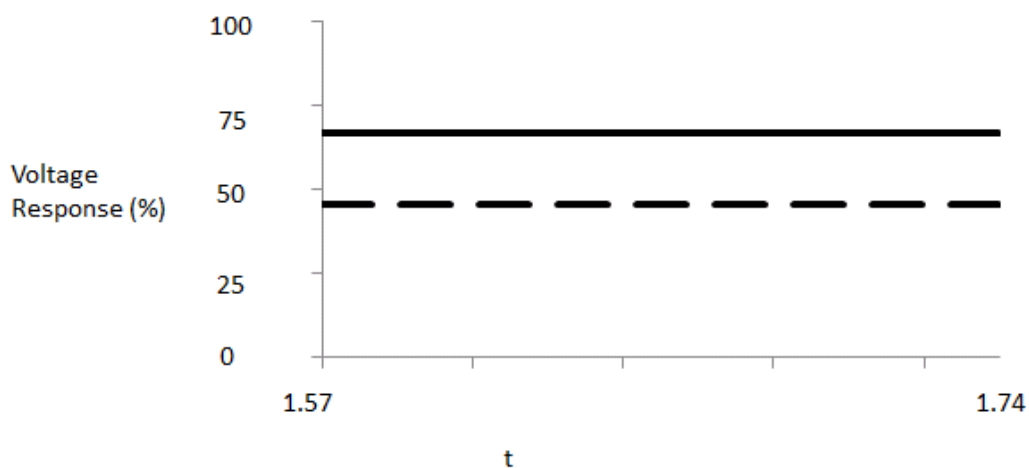


Figure 46: Influence of Au electrode surface on voltage responses are shown for CV1 — , and CV5 - - -. The thicker lines are for the case with the most water (twice of the Au electrode surface area in as-manufactured). The regular thickness lines are for the base case (the Au electrode surface area in as-manufactured).

Summarizing, the amount of water in the electrolyte is the most influential design factor for the voltage response. The sensor voltage response increases relative to that of the nominal design when there is more water, and decreases when there is less water. In

contrast, the voltage response is not influenced by changes in the height of electrolyte, BQ concentration, or surface area of the Au electrode.

The insights from these sensitivity analyses can be used in several ways. First, the sensitivity, or lack thereof, to changes in design parameters provides an indication of the robustness of the performance to variations in the design parameters. Changes in the amount of water in the electrolyte have a more pronounced effect, suggesting that water content in the electrolyte is a key factor to monitor, relative to other characteristics such as the height or volume of electrolyte.

The second use for insights from these analyses is the possibility of modifying the design of the sensor to produce a more dramatic or more rapid sensor response, enabling more rapid measurement of $p\text{CO}_2$, or modifications to the design to improve robustness or reduce manufacturing cost.

3.5 Summary

The mathematical model of the POC $p\text{CO}_2$ sensor has been successfully fitted using sensor performance data from the Abbott Point of Care database. The most influential model parameters influencing the predicted responses were identified using estimability analysis, and values for the two most estimable parameters were tuned to improve the quality of the model predictions. Finally, the use of the model for design investigation was illustrated using a series of sensitivity analyses on the main design parameters for the sensor. The model clearly indicated design factors having a pronounced influence on the

voltage response (e.g., water content), and those having a negligible influence (e.g., area of the Au electrode).

Chapter 4 Conclusions and Recommendations

4.1 Conclusions

In this thesis, a dynamic mathematical model was derived to predict the voltage response in a pCO₂ sensor when it is subjected to different CO₂ concentrations in the calibration fluid and control fluids. The model considers diffusion of species due to concentration gradients in the vertical and radial directions, and reaction phenomena in the electrolyte and at the Au electrode. Diffusion due to potential gradients and any potential change in the reference Ag/AgCl were not considered.

The model predicts the two most influential and uncertain parameters in the model were determined to be $k_{f_{Au}}$ and $K_{CO_{2m}}$, which are the forward rate constant for benzoquinone consumption at the gold surface, and the partition coefficient for CO₂ between the membrane and the electrolyte. These parameters were adjusted by hand to obtain a good fit (within 2 mV) between the dynamic voltage response data (during a predetermined number of seconds) and the model predictions. An even better fit would be expected if a formal least-squares parameter estimation study were performed or if additional parameters were estimated.

The model was fitted using test data from Abbott Point of Care, and was found to provide reliable predictions of the sensor voltage response over a time interval of interest.

Several design parameters were varied to study the influence of the electrolyte concentration and the sensor geometry on the voltage response. The model predicts the

most influential design parameter studied was the amount of water present in the electrolyte during the sensor operation. For example, increasing the water concentration by 50% resulted in an increase of 35% in the predicted voltage for the calibrant when the sensor is in contact with the calibrant fluid and an increase of 28% when the sensor is in contact with CV1 control fluid. These results suggest that the amount of water that evaporates or is absorbed by the sensor during manufacturing and storage may have an important influence on the sensor response. The model predicts that the changing the depth of the electrolyte fluid in the sensor was not as important as changing the water concentration.

The model predicts the initial buffer concentration in the electrolyte was the second most influential parameter. For example, increasing the buffer concentration from 0.005 mol L⁻¹ to 0.01 mol L⁻¹ increased the predicted voltage by ~20% when the sensor is in contact with the calibrant fluid and by ~10% when the sensor is in contact with CV1. The initial H₂CO₃ concentration, which might depend on the CO₂ concentration in the air during manufacturing was the third most sensitive parameter. For example, increasing the carbonic acid concentration from 0.00005 mol L⁻¹ to 0.0001 mol L⁻¹ increased the predicted voltage by ~5% when the sensor is in contact with the calibrant fluid and when the sensor is in contact with CV1. The model predicts that the initial benzoquinone concentration in the electrolyte had very little influence on the sensor response, and the surface area of the Au electrode was also not important to the predicted sensor response.

These results demonstrate the potential value of the mathematical model for providing insight into influential design parameters.

4.2 Contributions of this Thesis

This thesis has advanced the mathematical modeling of POC pCO₂ sensors beyond the current state of the art in the literature. The specific contributions of the thesis are:

1. Development of the model equations and approach for dealing with the BQ \rightleftharpoons HQ cascade and interaction at the electrode. This includes linking the Nernst equation to the reaction equilibrium constant for the BQ \rightleftharpoons HQ reactions, and developing a technique for initializing the concentrations in the sensor so that the PDE model can be solved.
2. Development of the material balance PDE model for the membrane and electrolyte, and subsequent parameter estimation using Abbott Point of Care test data.
3. Gathering and grouping model parameters, including identifying which characteristics (e.g., diffusivities) can be assumed to be similar.
4. An estimability analysis that identifies the most influential parameters in the PDE model, enabling tuning to produce more reliable predictions.
5. A preliminary investigation into the impact of different design parameters on the performance of the pCO₂ sensor.
6. Identifying appropriate model routines and techniques within COMSOLTM to represent, accommodate and solve the type of PDE model developed for the sensor (e.g., computing an average potential over the Au electrode).

4.3 Recommendations for Future Work

1. The model would benefit from additional data that could serve to further validate the predictions. Currently there are no plans to design and execute the experimental runs that would generate this data.
2. Consideration should be given to constructing a more complicated PDE model to account for changes in water concentration and temperature during the sensor operation. Additional data would be required to fit the parameters in this model and to test the model validity.
3. The diffusion of species within the electrolyte may be affected by the potential gradient and by activities rather than the concentrations of the species alone. A more complicated model that accounts for these effects should be developed, but would require additional knowledge of transport phenomena and thermodynamics in solutions with ions.
4. The potential of the reference electrode, Ag/AgCl, may change with time due to changes in ionic strength and changes in species activities. This effect should be incorporated in the model if additional data and knowledge are available.
5. The modeling approach should be applied to other POC sensors based on ion-selective electrodes. The mathematical model structure consists of diffusing species, possible dissociation in the electrolyte (depending on the analyte), and interaction with a electrochemical reaction cascade, leading to the potential measurement at the electrode.

References:

- Bialkowski, S. E. (2006). *Carbon Dioxide and Carbonic Acid*. Retrieved March 17, 2013, from Utah State University Environmental Chemistry Chemistry 3650 Course Website:
<http://ion.chem.usu.edu/~sbialkow/Classes/3650/Carbonate/Carbonic%20Acid.html>
- Burtis, C. A., Ashwood, E. R., & Bruns, D. E. (2006). *Tietz Textbook of Clinical Chemistry and Molecular Diagnostics*. Missouri: Elsevier Saunders.
- Cai, W.-J. and C.E. Reimers. (1993). The development of pH and pCO₂ microelectrodes for studying the carbonate chemistry of pore waters near the sediment-water interface. *Limnology and Oceanography*, 38, 1776-1787.
- Colt, J. (2012). *Dissolved Gas Concentration in Water: Computation as Functions of Temperature, Salinity and Pressure*. Waltham, U.S.A.: Elsevier.
- Cozzette et al. (1992). Patent No. 5112455. United States of America.
- Dabos, D. (1975). *A Handbook for Electrochemists in Industry and Universities*. Elsevier Scientific Publishing Company, New York, NY
- Davis, G., Lauks, I. R., Pierce, R. J., & Wildrig, C. A. (1996). *Patent No. 5514253*. United States of America.
- Global Industry Analysts, Inc. (2012). *Blood Gas and Electrolyte Analyzers - a Global Strategic Business Report*. Global Industry Analysts, Inc.
- Greeley, R. S., Smith, W. T., Stoughton, R. W., and Lietzke, M. H. (1960). Electromotive Force Studies in Aqueous Solutions at Elevated Temperatures. I. The Standard Potential of the Silver-silver Chloride Electrode. *Journal of Physical Chemistry*, 65(5), 652-657.
- Green, D. W. and Perry, R. H. (2008). *Perry's Chemical Engineers' Handbook*. McGraw-Hill, New York, NY.
- Guin, P. S., Das, S., and Mandal, P. C. (2011). Electrochemical reduction of quinones in different media: a review. *International Journal of Electrochemistry*.
- Haynes, W. M. (2012). *CRC Handbook of Chemistry and Physics*. CRC Press: Boca Raton, FL
- Holz, M., Heil, S.R. and Sacco, A. (2000) Temperature-dependent self-diffusion coefficients of water and six selected molecular liquids for calibration in accurate

- ¹H NMR PFG measurements. *Physical Chemistry Chemical Physics*, 2, 4740–4742.
- Hui, Y., Chng, E. L., Chng, C. Y., Poh, H. L. and Webster, R. D. (2009). Hydrogen-Bonding Interactions between Water and the One-and Two-Electron-Reduced Forms of Vitamin K1: Applying quinone Electrochemistry to Determine the Moisture Content of Non-Aqueous Solvents. *Journal American Chemical Society*, 131(4), 1523–1534
- Ives, D. J., and Janz, G. J. (1961). *Reference Electrodes: Theory and Practice*. New York: Academic Press.
- Jensen, M. A., and Rechnitz, G. A. (1979). Response Time characteristics of the $p\text{CO}_2$ Electrode. *Analytical Chemistry*, 51(12), 1972-1977.
- Lane, E. E., and Walker, J. (1987). *Clinical Arterial Blood Gas Analysis*. Mosby: St. Louis.
- Lauks, I. (1998). Microfabricated Biosensors and Microanalytical Systems for Blood Analysis. *Accounts of Chemical Research*, 31, 317-324.
- Lauks, I., and Maczuszenko, A. (2006). *Patent No. US20060137980 A1*. U.S.A.
- Lindsey, A. S. (1974). Polymeric Quinones. *The Chemistry of Quinonoid Compounds*, 1, 793-856. London: John Wiley & Sons.
- Lopez, M. E. (1984). Selectivity of the Potentiometric Carbon Dioxide Gas-Sensing Electrode. *Analytical Chemistry*, 2360-2366.
- Maas, A. H., Van Heijst, N. P., and Visser, B. F. (1971). The determination of the true equilibrium constant (pK_{1g}) and the practical equilibrium coefficient (pK_{1g}) for the first ionization of carbonic acid in solutions of sodium bicarbonate, cerebrospinal fluid, plasma, and serum at 25 and 38°. *Clinica Chimica Acta*, 33, 325-343.
- Manahan, S. E. (2005). *Environmental Chemistry*. Boca Raton: CRC Press.
- McLean K. A. P. and K. B. McAuley. (2012). Mathematical Modelling of Chemical Processes – Obtaining the Best Model Predictions and Parameter Estimates using Identifiability and Estimability Procedures. *Canadian Journal of Chemical Engineering*, 90, 351-366.
- Meyerhoff, M. E., Fraticelli, W. N., Opdycke, W. N., Bachas, L. G., and Gordus, A. D. (1983). Theoretical Predictions on the Response Properties of Potentiometric Gas Sensors Based on Internal Polymer Membrane Electrodes. *Analytica Chimica Acta*, 154, 17-31.

- Newman, J., and Thomas-Alyea, K. E. (2004). *Electrochemical Systems*. Hoboken: John Wiley & Sons, Inc.
- Ramsay, G. (1988). *Commercial Biosensors: Applications to Clinical, Bioprocess, and Environmental Samples*. New York: John Wiley & Sons, Inc.
- Rikely, J., & Skirrow, G. (1975). *Chemical Oceanography*, v.1. New York: Academic Press.
- Ross, J. W., Riseman, J. H., & Krueger, J. A. (1973). Potentiometric Gas Sensing Electrodes. *Pure and Applied Chemistry*, 473-487.
- Samukawa, T., Ohta, K., Onitsuka, M., & Motohashi, R. (1995). Numerical Approach to the Explanation of the Response Time of the Severinghouse Type Electrode. *Analytica Chmica Acta*, 316(1), 83-92. P
- Severinghaus, J. W., & Bradley, A. F. (1958). Electrodes for Blood pO_2 and pCO_2 Determination. *Journal of Applied Physiology*, 13(3), 515-520.
- Snokeyink, V. and Jenkins, D. (1980). *Water Chemistry*. New York: Wiley.
- Thompson, D.E., McAuley, K.B. and McLellan, P.J. (2009).Parameter estimation in a simplified MWD model for HDPE produced by Z-N catalyst, *Macromolecule Reaction Engineering*, 3, 160-177.
- Tongol, B.J.& Binag, C.A. and Sevilla, F.B.(2003).Surface and electrochemical studies of a carbon dioxide probe based on conducting polypyrrole. *Sensors and Actuators B*, 93, 187-196.
- Wu. S., McLean, K. A. P. , Harris, T.J., and McAuley, K.B. (2011). Selection of Optimal Parameter Set Using Estimability Analysis and MSE-based Model Selection Criterion. *International Journal of Advanced Mechatronic Systems*, 3, 188-197.
- Yang, L.-J., and Kao, A.-F. (2010). Gas Permeation in PDMS Monitored by On-site Pressure Sensors, *Proceedings of IEEE NEMS '10 (Xiamen, China, 20–23 January 2010)*, 348–351.
- Zeebe, R. E. (2011). On the molecular diffusion coefficeints of dissolved CO_2 , HCO_3^- , and CO_3^{2-} and their dependence on isotopic mass. *Geochimica et Cosmochimica Acta*, 75, 2483-2498.
- Zhao, P., and Cai, W. (1997). An Improved Potentiometric pCO_2 Microelectrode. *Analytical Chemistry*, (69), 5052-5058.

Zosel, J., Oelbner, W., Decker, M., Gerlach, G., and Guth, U. (2011). The Measurement of Dissolved and Gaseous Carbon Dioxide Concentration. *Measurement Science and Technology*, 22 (7), 072001-072046.

Appendix:

The “user-controlled mesh” was used in COMSOL™ 4.3.0. to generate the mesh and the elements in the mesh are triangular (See Figure A.1). The number of iterations is 8 and the integration order for the average voltage at the Au electrode is 4th order (See Figure A.2).

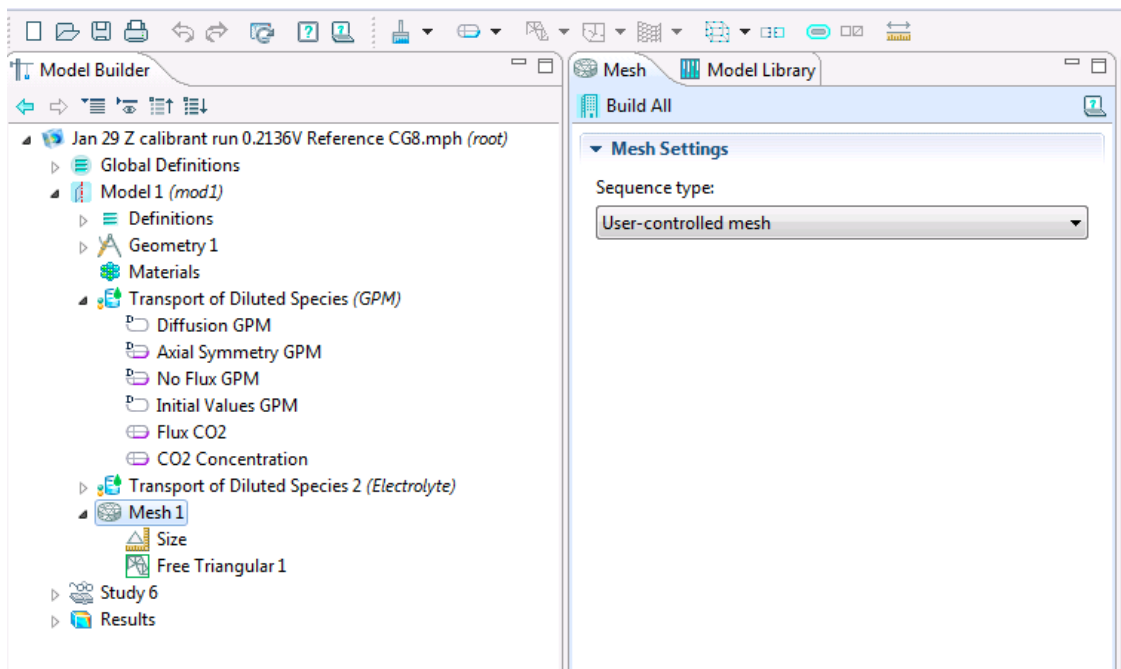


Figure A. 1: “User-controlled mesh” in COMSOL™ 4.3.0

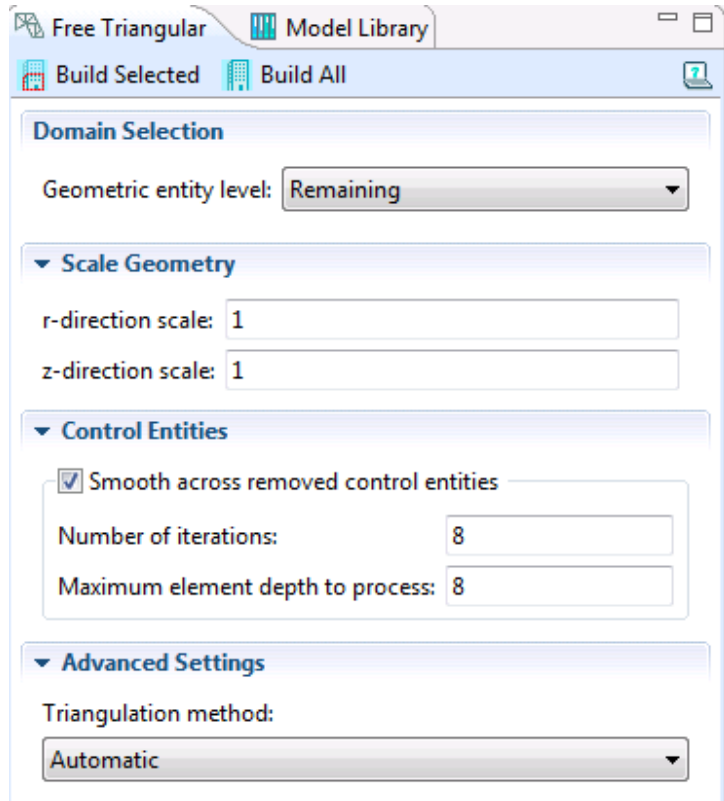


Figure A. 2: Settings for number of iterations and integration order

The maximum element size was varied (See Figure A.3) while keeping the other element size parameters constant (i.e., minimum element size, maximum element growth rate, resolution of curvature, and resolution of narrow regions). Maximum element sizes of 0.4, 0.6 and 0.8 μm were selected. They each generated 16911, 8460 and 4724 elements over the model domain respectively. The computation times for these three meshes were about 40 min, 20 min and 10 min respectively.

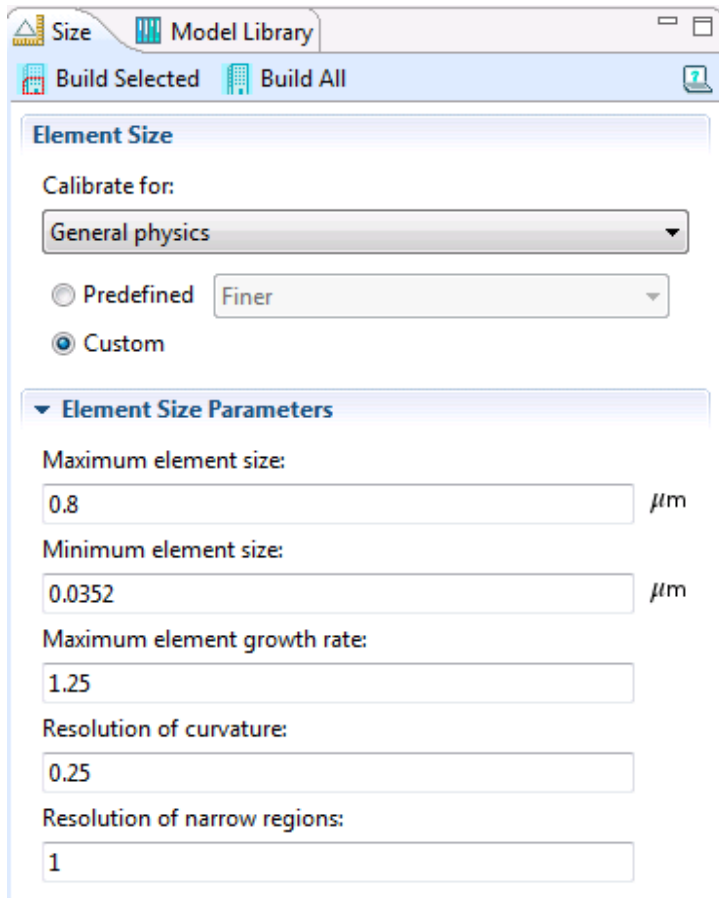


Figure A. 3: “Maximum element size” under “Element Size” tab

Figure A.4 is a fine mesh for the entire sensor with a maximum element size of 0.6 μm .

Figures A.5 to A.7 are the meshes for one end of the sensor with maximum element sizes of 0.4 μm , 0.6 μm and 0.8 μm respectively.



Figure A. 4: Mesh for the central portion of the sensor (between $r = 0 \text{ m}$ and $r = 2.000 \times 10^{-4} \text{ m}$) with a maximum element size of 0.6 μm .

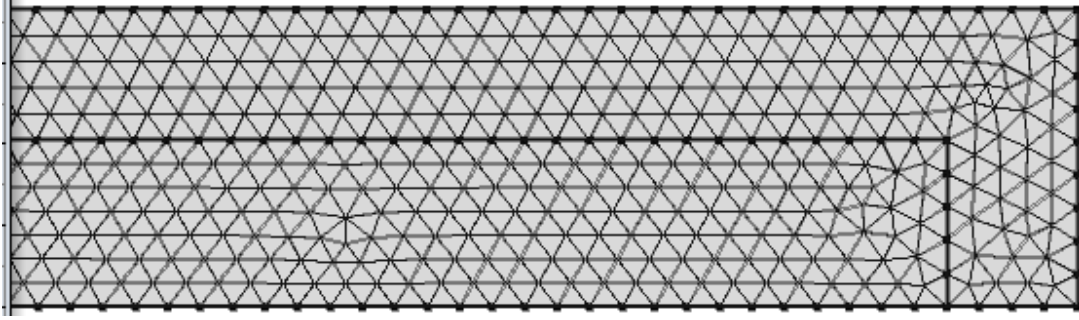


Figure A. 5: Mesh for the outer portion of the sensor (between $r = 2.670 \times 10^{-4}$ m and $r = 2.816 \times 10^{-4}$ m) with a maximum element size of 0.4 μ m.

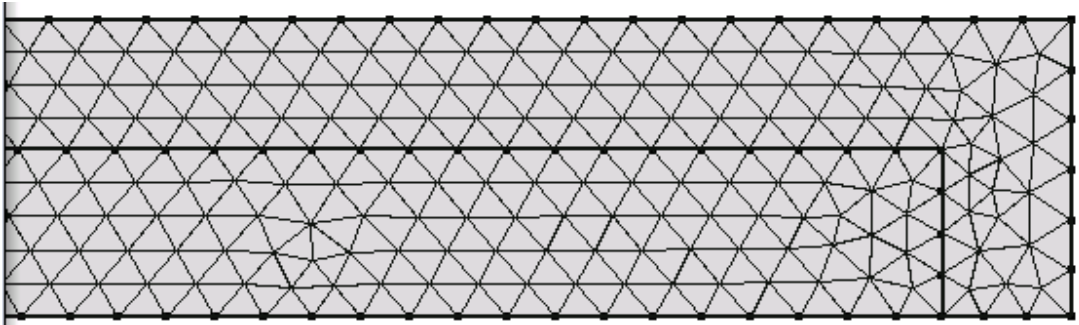


Figure A. 6: Mesh for the outer portion of the sensor (between $r = 2.670 \times 10^{-4}$ m and $r = 2.816 \times 10^{-4}$ m) with a maximum element size of 0.6 μ m.

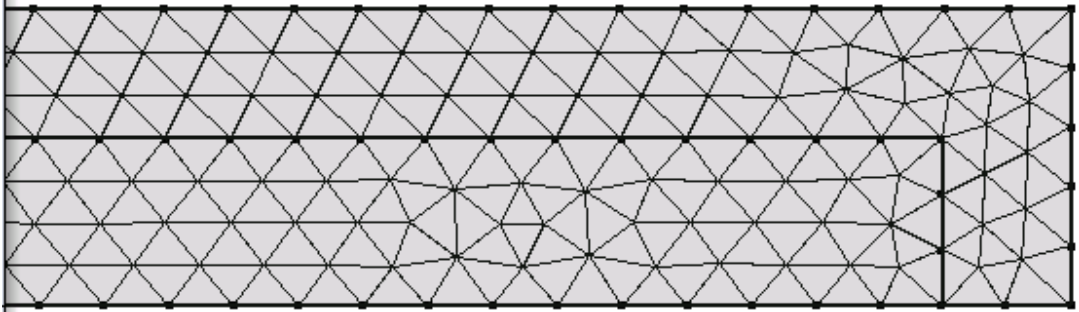


Figure A. 7: Mesh for the outer portion of the sensor (between $r = 2.670 \times 10^{-4}$ m and $r = 2.816 \times 10^{-4}$ m) with a maximum element size of 0.8 μ m.

Parameter values in Table 8 plus updated values of $k_{f_{Au}} = 66.6 \frac{m^7}{s \cdot mol^2}$ and $\kappa_{CO_{2m}} = 1.2$

were used to generate the following plots in Figures A. 8 and A.9 for the calibrant.

Since all the voltage vs time plots overlap and the concentration profiles overlap with different maximum element sizes, grid independence was achieved. Therefore, a maximum element size of 0.8 μm was used.

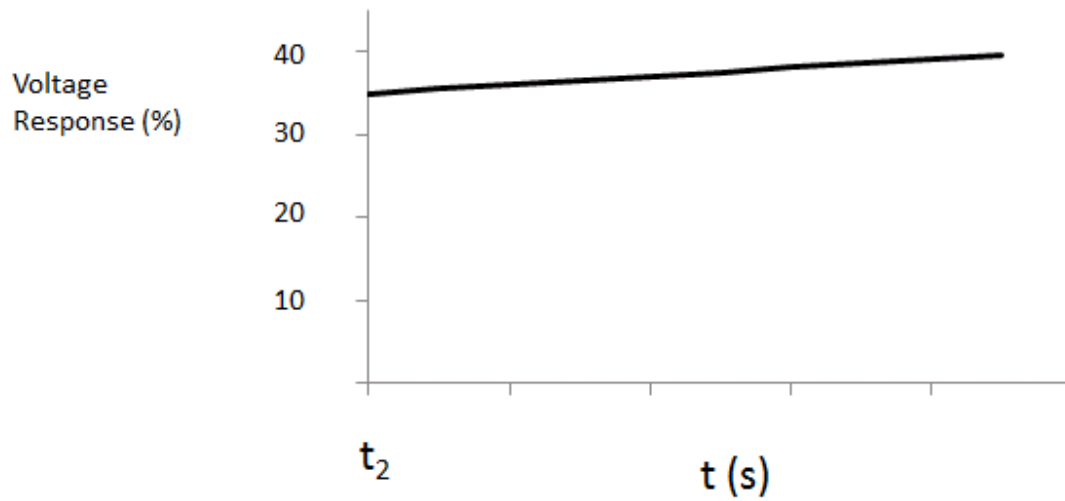


Figure A. 8: Voltage responses versus time for maximum element size of 0.4 μm , 0.6 μm and 0.8 μm . The three plots overlap.

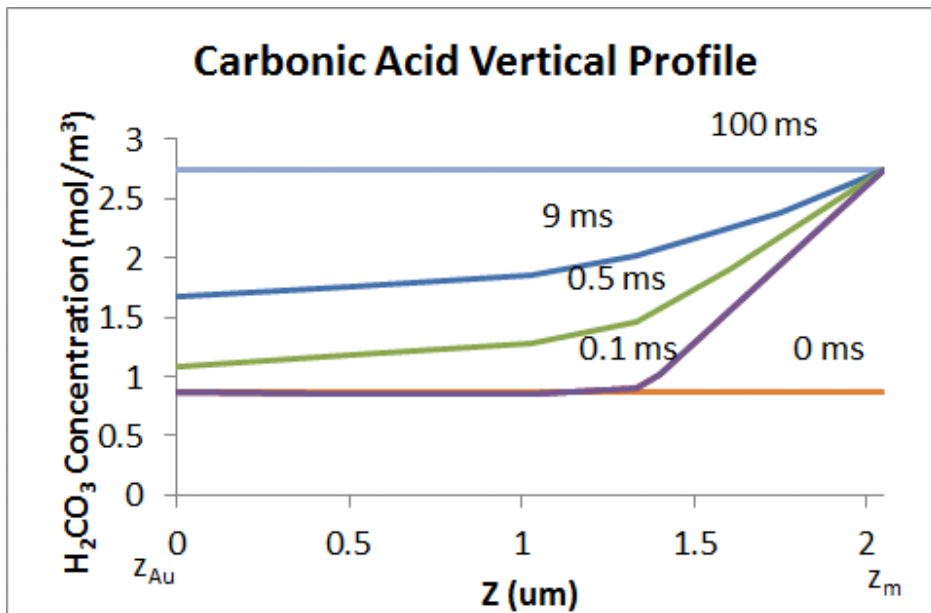


Figure A. 9: Concentration profiles of carbonic acid for maximum element size of 0.4 μm , 0.6 μm and 0.8 μm . The plots overlap.

Time tolerance was also investigated. Under the “Time Dependent” tab (See Figure A. 10), the relative tolerance was varied. Three tolerances were used: 5×10^{-8} s, 2×10^{-7} s and 1×10^{-7} s. The same plots (See Figures A.11 and A.12) were generated and the voltage plots overlap and the concentration profiles overlap as well. A relative tolerance of 1×10^{-7} s for the time setting was used for the simulations.

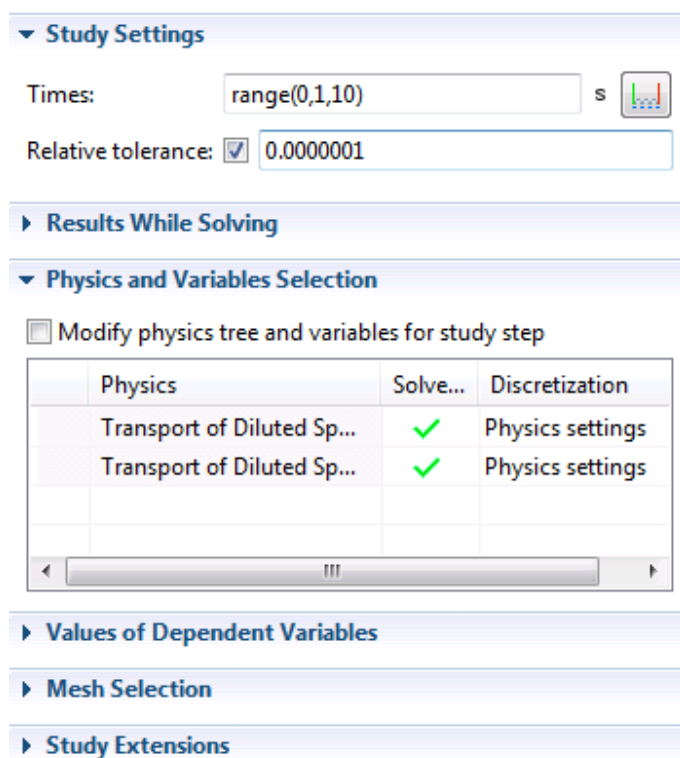


Figure A. 10: Setting up the relative tolerance for time in COMSOL™.

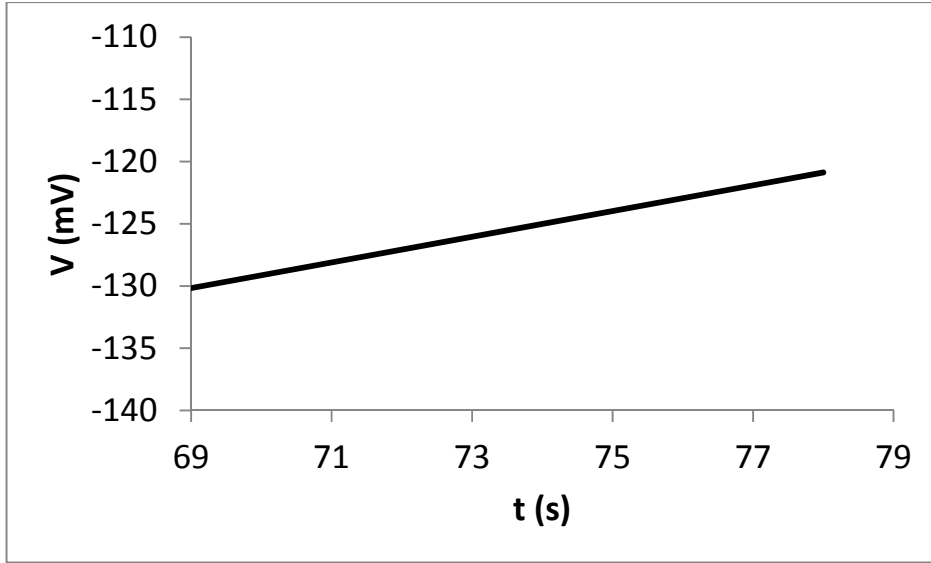


Figure A. 11: Voltage responses versus time for time relative tolerances of 5×10^{-8} s, 2×10^{-7} s and 1×10^{-7} s. The three plots overlap.

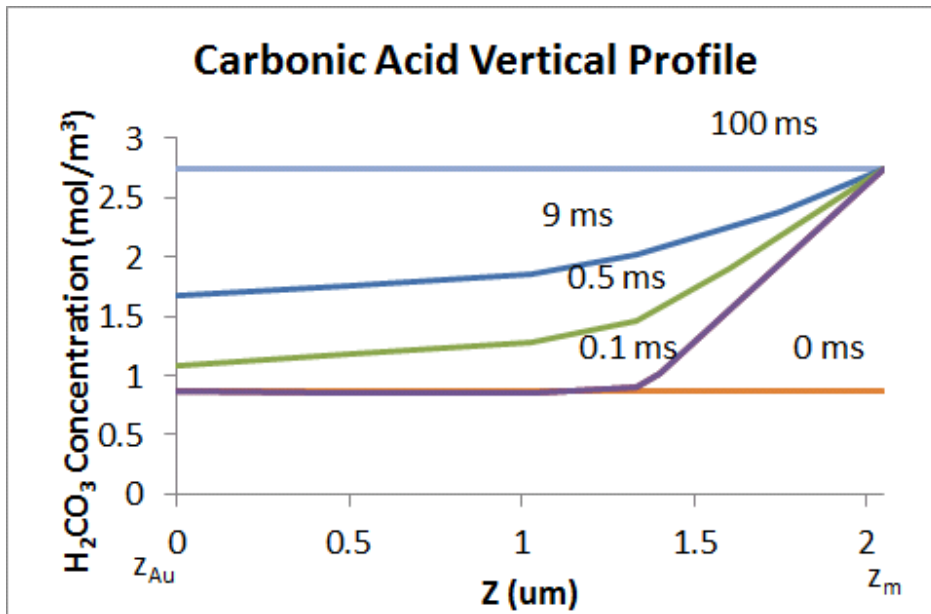


Figure A. 12: Concentration profiles of carbonic acid for time relative tolerances of 5×10^{-8} s, 2×10^{-7} s and 1×10^{-7} s. The plots overlap.